Soft Robotic Hands
For Compliant Grasping

vorgelegt von

Raphael Deimel, MSc

geb. in Wien

von der Fakultät IV — Elektrotechnik und Informatik
der Technischen Universität Berlin
zur Erlangung des akademischen Grades

Doktor der Ingenieurwissenschaften
— Dr.-Ing. —

genehmigte Dissertation

Promotionsausschuss:

Vorsitzender:	Prof. Dr. Marc Alexa
1. Gutachter:	Prof. Dr. Oliver Brock
2. Gutachter:	Prof. Dr. Kaspar Althoefer
3. Gutachter:	Prof. Dr. Sami Haddadin

Tag der wissenschaftlichen Aussprache: 23.6.2017

Berlin 2017

Abstract

The thesis considers the problem of grasping for autonomous robots, with a focus on the design and construction of robotic hands and grippers. The approach we take is to fundamentally reconsider the basic motivation and goals for grasping that steer hand design. We consider grasping as the result of reliable and robust patterns of interaction between hand, object and environment which are mechanically opaque to the robot. This motivates the investigation of a new type of robotic hands, *pneumatic soft hands*. These hands enable the robot to collide with objects safely, maintain contact under disturbance, and provide many places of contact for a robust grasp. At the same time they intend to lower requirements on control and perception compared to fully actuated hands. Due to the fundamental change in perspective compared to the classical, mechanics-centric view in grasping, I believe we will ultimately have to reconsider all aspects of a robot system to use soft hands effectively. We call this alternative view the *Soft Manipulation* paradigm. In this thesis we propose a list of defining principles for Soft Manipulation and focus on the ramifications for hand hardware, but we also consider the adjacent domains of hand control and grasping strategies.

Research on soft hands is complicated by the fact that the technology and body of knowledge for building soft hands only is emerging right now. The thesis contributes the groundwork for soft hand research by developing a coherent and comprehensive set of tools to rapidly prototype pneumatic soft hands. This toolkit is built around a versatile and easy to prototype actuator design named PneuFlex. The thesis will cover all aspects of prototyping such as designing mechanical properties, manufacturing actuators, assembling them into hands, and controlling them without interfering in their compliance. We also propose and validate a fast and stable dynamic simulation model for the simulation of pneumatic soft hands which for the first time makes interactive and automated design of soft hands feasible.

The thesis also explores the properties and capabilities of pneumatic soft hands in a series of grasping experiments with the help of two artifacts, the *RBO Hand 1* and *RBO Hand 2*. We investigate their shape adaptability, their grasp dexterity, and their suitability for implementing grasping strategies that exploit environment constraints to motion for robust execution. We will see that soft hands built with technology developed in the first part of the thesis provide a solid foundation for further research on Soft Manipulation.

Zusammenfassung

Diese Dissertation betrachtet das Problem des Greifens für autonome Roboter mit Fokus auf die Gestaltung und Konstruktion von Roboterhänden. Wir überdenken in unserem Ansatz dabei die fundamentalen Vorstellungen und Ziele für funktionelle Roboterhände. Wir verstehen dabei Greifen als das Ergebnis zuverlässiger und robuster Interaktionen zwischen Hand, zu greifendem Objekt und dessen Umgebung. Die zugrundeliegende Mechanik dieser Interaktion ist dem Roboter dabei nicht zugänglich. Aus der geänderten Aufgabenstellung folgt eine neue Art, Roboterhände zu bauen: *pneumatische weiche Hände*. Diese Hände sollen dem Roboter ermöglichen, sicher mit Objekten zu kollidieren, Kontakt während einer Bewegung zu halten, und viele Kontaktpunkte zu erzeugen. Gleichzeitig zielen diese weichen Hände auf eine Reduktion der Anforderungen an Regelung und Wahrnehmung ab, im Gegensatz zu klassischen, vollständig kontrollierten Händen. Aufgrund des grundlegenden Perspektivenwechsels gegenüber der vorherrschenden, mechanisch-zentrischen Sichtweise müssen letztlich alle Aspekte eines Robotersystems überdacht werden, will man weiche Hände effektiv nutzen. Zwar konzentriert sich der Inhalt dieser Arbeit auf weiche Hände an sich, streift aber auch die Themen Regelung und Greifstrategien.

Die Forschung an weichen Händen gestaltet sich jedoch noch schwierig, da das Wissen um Konstruktion und Verwendung weicher Hände gerade erst erarbeitet wird. Deshalb trägt diese Dissertation ein umfassendes und kohärentes System für die schnellen Bau weicher Hände rund um die so genannten PneuFlex Aktoren zusammen. Die Arbeit beleuchtet alle Aspekte des Handdesigns, vom Entwurf mechanischer Eigenschaften, der Herstellung von Aktoren, dem Zusammenfügen zu kompletten Händen bis zu einer Steuermethode die die Nachgiebigkeit weicher pneumatischer Aktoren optimal ausnützen kann. Wir präsentieren und validieren außerdem eine schnelle und stabile dynamische Simulation pneumatischer weicher Hände. Dieser Durchbruch ermöglicht erstmals das interaktive oder automatisierte Design weicher Hände zu deren Anpassung an spezifische Anwendungen.

Im zweiten Teil untersucht die Arbeit die Eigenschaften und Fähigkeiten von pneumatischen weichen Händen in einer Reihe von Experimenten mit Hilfe zweier Artefakte, der *RBO Hand 1* und *RBO Hand 2*. Wir untersuchen dabei deren Formanpassungsfähigkeit, die erreichbare Griffvielfalt, und ihre Eignung für Greifstrategien, die auf dem Ausnutzen

von Einschränkungen der Roboterbewegung durch umgebende Objekte aufbauen. Wir werden dabei auch sehen, dass pneumatische weiche Hände für weiterführende Forschung an nachgiebiger Manipulation bestens geeignet sind.

Acknowledgements

Writing this thesis would not have been possible without the support of many great minds. I had the pleasure to work with the most critical yet constructive group of people I have ever met, at the Robotics and Biology Lab. Only in such an environment it is possible to question and reformulate fundamental assumptions. This especially is true for my long-time colleagues Clemens Eppner, Sebastian Höfer, Roberto Martin-Martin, Arne Sieverling, Rico Jonschkowsi, Michael Schneider, Ines Putz and Mahmoud Mabrouk and Kolja Stahl. Each of them – sometimes unwittingly – contributed to my work in various ways. And of course, Vincent Wall, who was never satisfied with superficial explanations and pushed me to reformulate my thoughts time and again to make them communicable. You all are amazing, everyone in their own way. So are Jessica Abele, Can Erdogan, Manuel Baum and Elöd Páll, it has been very satisfying to see you using the soft hands, and to know that there are people that will carry on the research with soft hands. Janika Urig deserves recognition too, for her help on many small administrative issues throughout the years. I also want to thank all the collaborators I had the pleasure to work with, especially the members of the SOMA project and Keyan Ghazi-Zahedi. Most of our collaborations did not make it into this thesis, but I assure you this is owed to limits in page length and not interestingness of our joint ventures. I also need to apologize to my family, who at difficult times I could not support as much as I had wanted to because of this thesis.

The list is getting long but the most important people haven't been mentioned yet. Great thanks to Oliver Brock, who has been incredibly supportive of investigating unorthodox ideas that most other researchers would not even consider. I therefore owe you more than anybody else for being able to write a fair amount of bold claims and transformative ideas into this thesis. I also want to thank you on improving my writing skills in the course of endless series of paper versions we iterated over together.

And finally, I have to thank Monika who gave me unconditional trust and advice every single time I was hitting the figurative wall throughout the years. I deeply appreciate your presence, both emotionally and intellectually.

Eidesstattliche Erklärung

In accordance with §5, Sec. 1 of the Doctoral Regulations by TU Berlin,

- re. (1): I hereby declare that I am acquainted with the current doctoral regulations of the TU Berlin as of 23 October 2006, last amended on 5 February 2014.
- re. (5): I hereby declare that all pre-publications of the dissertation or parts thereof and details of own contributions according to §2, subparagraph 4 doctoral regulations are listed in the attachment.
- re. (6): I hereby declare in lieu of an oath that I have independently completed the dissertation. All aids and sources have been listed and all details regarding own contributions according to (5) are correct.
- re. (7): I hereby declare that I have listed all applications (if any) for admission as a doctoral candidate or admission to doctoral procedure according in Sec. 4. of this form.

Berlin,

_____

Raphael Deimel

Prepublication and Statement of Contribution

Prior Publications

Parts of this thesis have been published in the following publications:

[A] Raphael Deimel and Oliver Brock. “A Compliant Hand Based on a Novel Pneumatic Actuator”. In: *IEEE International Conference on Robotics and Automation (ICRA)*. IEEE International Conference on Robotics and Automation (ICRA). 2013, pp. 2047–2053

[B] Raphael Deimel and Oliver Brock. “A novel type of compliant, underactuated robotic hand for dexterous grasping”. In: *Proceedings of Robotics: Science and Systems (RSS)*. Robotics: Science and Systems. 2014, pp. 1687–1692

[C] Raphael Deimel and Oliver Brock. “A novel type of compliant and underactuated robotic hand for dexterous grasping”. In: *The International Journal of Robotics Research* 35.1 (2016), pp. 161–185

[D] R. Deimel, C. Eppner, J. Alvarez-Ruiz, M. Maertens, and O. Brock. “Exploitation of Environmental Constraints in Human and Robotic Grasping”. In: *Proceedings of the International Symposium on Robotics Research (ISRR)*. International Symposium on Robotics Research (ISRR). 2013

[E] Clemens Eppner, Raphael Deimel, José Álvarez-Ruiz, Marianne Maertens, and Oliver Brock. “Exploitation of environmental constraints in human and robotic grasping”. In: *The International Journal of Robotics Research* 34.7 (2015), pp. 1021–1038

[F] Raphael Deimel and Oliver Brock. “Soft Hands for Reliable Grasping Strategies”. In: *Soft Robotics, Soft Hands, Grasping*. Berlin Heidelberg: Springer-Verlag, 2015, pp. 211–221

[G] Raphael Deimel, Marcel Radke, and Oliver Brock. “Mass control of pneumatic soft continuum actuators with commodity components”. In: *Proceedings of the Intelligent Robots and Systems (IROS), 2016 IEEE/RSJ International Conference on*. IEEE, 2016, pp. 774–779

Contributions to Each Prior Publication

Here I clarify my contributions to each prior publication.

[A] I am the sole first author of this paper. The last author conceived the project idea, gave scientific advice and contributed to paper writing.

[B] I am the sole first author of these papers. The last author conceived the project idea, gave scientific advice and contributed to paper writing.

[C] I am the sole first author of these papers. The last author conceived the project idea, gave scientific advice and contributed to paper writing.

[D] The first three authors contributed to the publications in equal parts. The last author gave scientific advice and contributed to paper writing. The Environmental Constraint Exploitation concept was jointly developed by all authors. I am the sole contributor of the content in Section 4.2. Only the contribution mentioned is used in this thesis.

[E] The first three authors contributed to the publications in equal parts. The last author gave scientific advice and contributed to paper writing. The Environmental Constraint Exploitation concept was jointly developed by all authors. I am the sole contributor of the content in Section 5. Only the contribution mentioned is used in this thesis.

[F] I am the sole first author of this paper. The last author gave scientific advice and contributed to paper writing.

[G] I am the first author of this paper. The second author contributed substantially to the example implementation of mass control and conducted the data acquisition of the validation experiments. The last author gave scientific advice and contributed to paper writing.

Contributions to Each Chapter

Chapter 1: The content is original to this thesis.

Chapter 2: The content is original to this thesis.

Chapter 3: The content is based on the publications [A,B,C] The actuation principle and manufacturing method are described in [A,B,C], the analytic model and design rules are derived in [C] and the validation experiments are described in [C]. The following content is original to this thesis: The inclusion of the side wall in the analytic model, the analysis of material choices on reliability and robustness, and a compilation of best practices for soft hand building.

Chapter 4: The content is based in part on publication [G]. It describes the formalization and implementation of mass control for discrete commodity valves. The categorization of mass control as a form of equilibrium-point control is original to this thesis.
Chapter 5: The content of this chapter is original to this thesis.
Chapter 6: The content is based in part on publications [A,D,E,F]. The shape adaptability hypothesis is proposed in [A], the Environmental Constraint Exploitation concept is proposed in [D,E]. The refinement into categories of motion patterns based on intent is published in [F]. The proposal of principles for Soft Manipulation is original to this thesis.
Chapter 7: The content is based in part on publications [A,B,C]. The morphology of the RBO Hand 1 is described in [A], the morphology of RBO Hand 2 in [B,C].
Chapter 8: The content is based on publications [A,B,C]. The experiments relating to shape adaptability are published in [A], the experiments on grasp diversity in [B,C]. The experiments on control complexity are published in [C].
Chapter 9: The content is based on publications [D,E,F]. The construction of grasping strategies based on exploiting environmental constraints is described in [D,E,F]. The surface-constrained grasp and the push-grasp examples are published in [A,D], the edge grasp in [D, E] and the wall grasp in [E,F].

Table of Contents

Foreword

I think it is fair to say that the development of pneumatic soft hands has been a success story. Since the initial idea of building a hyper-compliant gripper to investigate the limits of the shape adaptability hypothesis five years ago, steady progress lead to a point where pneumatic soft hands are optimized in simulation, incorporate sensors, and provide an agile reference platform for developing new grasping strategies. Their use as one of the main hand hardware platforms in the Horizon 2020 project *Soft Manipulation* also illustrates their success.

From the beginning it was also clear: soft hands need to be cheap and fast to build, in order to encourage high-potential yet low-risk experiments that accelerate research progress. For long-term impact soft hands additionally need to be easy to build for dissemination to roboticists of all disciplines, not just mechanical engineers. In order to succeed here, we had to provide examples for the big picture of a soft hand based system: rapid prototyping tools and reference hardware designs, but also control methods and application examples. Reflecting this broad scope, this thesis boasts contributions to a wide range of topics, which are connected by the soft hands as the central artifacts of research.

Orthogonally to these efforts, we also aimed at the long-term goal of establishing pneumatic soft hands as an effective and reliable component in robotics by actively proliferating soft hand technology beyond the Lab to gather feedback and use it to improve robustness and usability. At the time of writing of the thesis, RBO Hand 2s have been deployed and used at nine partner institutions.

Looking beyond pneumatic soft hands, there are also other promising hand platforms under active development that incorporate the principle of softness to varying degrees. Especially underactuated hands and grippers such as the Pisa/IIT SoftHand, or the SDM and iHY hands share many design principles with pneumatic soft hands. Together they can be seen as members of a new class of robot end effectors – soft hands – that hopefully will catalyze a quantum leap in our understanding on how to make robots competently manipulate their environment.

Chapter 1

Introduction and Overview

This chapter introduces challenges in robot grasping, explains the approach we took, lists the main contributions of this thesis and lays out its structure.

1.1 Problem Statement

In this thesis, we consider the problem that in open and uncontrolled environments, robots cannot perform grasping robustly and reliably today. It is symptomatic that practically all mass applications of autonomous robots foreseeable in the immediate future are devoid of grasping, e.g. autonomous driving, air- and seaborne robots, robotic tour guides and floor cleaning robots. The lack of ubiquitous grasping skills holds back the proliferation of robotic solutions in many otherwise feasible application scenarios. Even in highly controlled environments such as factories and customer fulfillment centers: pick-and-place tasks are predominantly done by human workers and not robots.

Why is that? Grasping and manipulation has already been a topic of research for decades. The canonical view on grasping is condensed in standard books such as the Springer Handbook of Robotics [89]. Here, the act of grasping is presented as the act of obtaining a special mechanical relationship (transmission of arbitrary forces) between two rigid, possibly articulated bodies. And it is formalized within a mechanical description of the world. Exemplary topics of classical grasping research are:

- Distinguish grasp from non-grasp situations (grasp quality, force closure property, form closure property)
- Determine which forces can be effected on an object (grasp matrix, manipulability ellipsoids, grasp wrenches)
- Compute joint configurations that result in a grasp posture (random search, postural synergies, grasp primitives)
- Ensure the dynamic stability of controlled contact forces (force balancing)

The main appeal of a purely mechanical description is, that it is mathematically clean, consistent, and that it is universal, i.e. it can in principle represent all possible hand morphologies and grasp configurations. But the devil is in the detail. Manipulation and grasping necessarily involves contact, and in general contacts are neither linear nor smooth nor deterministic in terms of their mechanical description. Even worse, these undesirable properties are paired with high dimensionality as we usually need to consider a sizable number of contacts concurrently, and each contact contributes six dimensions.

As a result, the seemingly clean and complete canonical formulation reveals itself as a high-dimensional and non-linear cost landscape with frequent discontinuities. This insight partially explains the struggle of information-theoretic approaches to grasping, and may explain why general grasp planning (such as the GraspIt! toolkit [77]) did not improve much beyond random search.

The abundance of nonlinearity and discontinuities also has another grave consequence: Even small errors (e.g. introduced by unavoidable uncertainties in perception) can lead to

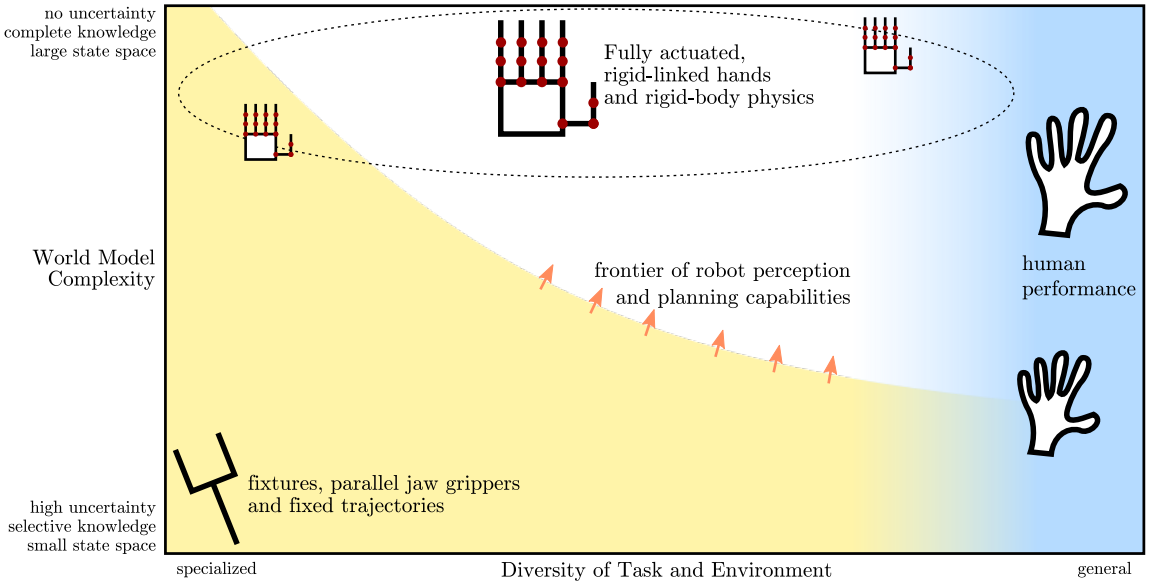

Fig. 1.1 Map of robot systems with respect to their intended task generality and the complexity of perception and actuation required by the hardware and internal world model. The blue area to the right indicates the level of competence we desire. The yellow area indicates systems for which we know how to build perception and control. In this map, engineered fixtures and simple grippers reside in the lower left corner, while systems with fully actuated robot hands [3, 45, 98] usually presume a detailed, accurate world model, and thus reside in the upper half of the map.

arbitrarily large changes in grasping and manipulation outcomes. In classical approaches, solving this problem is nonchalantly delegated to perception by assuming an accurate mechanical description of the world. Unfortunately, robot perception does not appear to be capable of achieving a sufficiently accurate and reliable world representation anytime soon, if at all. Nevertheless, the prevalent view of grasping has motivated robot hand research to aim for precise, accurate and arbitrary positioning and force application, without considering the ramifications to perception and control that need to provide the control signals. As a result, today we have – from a control perspective – very sophisticated robot hands [45, 117, 98] but fail to use them effectively in uncontrolled environments and on general grasping tasks.

To better understand the issue, we can organize hand hardware in a conceptual space that juxtaposes the task generality desired of a robot system using a given hand morphology with the resulting requirements placed on control and perception. This map is drawn in Figure 1.1. On the right side, it features the human capable of grasping in diverse tasks. This is where we want to progress our robot systems towards. From bottom to top, we indicate the amount of complexity demanded by the robot manipulator from the rest of the system, perception and control. Classical robot hands are engineered for precision, accuracy, and arbitrary motion,

which places them in the upper half of the map. The yellow region represents the actual capabilities of today's perception and control. For very specific tasks we are able to satisfy the requirements of even very complicated and precise hardware. The further we progress towards more general settings though, it becomes progressively difficult for perception and control to provide the level of accuracy and certainty that is required to make use of fully controlled, precise and accurate robot hands. Unfortunately, the intersection between systems with classical robot hands and systems with sufficient perception capabilities is on the left-task-specific side, and not on the task-general side to the right.

Are there Alternatives? The fundamental issues raised in the previous paragraphs beg the question of whether understanding grasping (and manipulation in general) from a purely mechanical point of view maybe is an ill-posed problem, as it drives our system into the upper half of the map in Figure 1.1. Are there alternatives that place us in the lower half instead, where perception and control are feasible today?

A starting point can be found by looking at the end effectors that are actually delivered with robot arms and used by most applications: fixtures and grippers. Here, end effectors are purposefully engineered to perform robustly and reliably, but only on a very narrow selection of objects and environments. Control is relatively simple as only one or two degrees of actuation are provided. Often, only one single, predefined grasp motion (or motion primitive) is executed instead of doing a full-blown motion planning and kinematic analysis. In Figures 1.1 and 1.2 these solutions reside in the lower left corner.

Over the years, researchers designed grippers that improve their generality, e.g. to increase the diversity of graspable object shapes or to allow for less certain object location. A good and recent example for a gripper following this idea is the SDM hand [29] (shown in Figure 7.1a). By simply replacing rotational joints with bend- *and* twistable pieces of rubber, the gripper gains additional, passive degrees of freedom that enable it to better comply to the orientation of an object surface [29]. This improvement in generality was accomplished without making control, and especially perception more difficult. Because of this, we can place the system in the lower half of the map, as done in Figure 1.2. Another example is the Pisa/IIT SoftHand [8] (shown in Figure 7.1d), which incorporates dislocatable joints to improve robustness, and a carefully designed joint coupling to keep control simple despite having nineteen degrees of freedom. Here, researchers simplified control of a hand design while maintaining its capabilities afforded by a highly articulated hand shape. They therefore moved from the top half downwards, improving system capability by making perception and control easier.

Both hand designs can be considered precursors or first representatives of a new class of robot end effectors: *soft hands*. In contrast to classical "rigid" hands (i.e. hands with

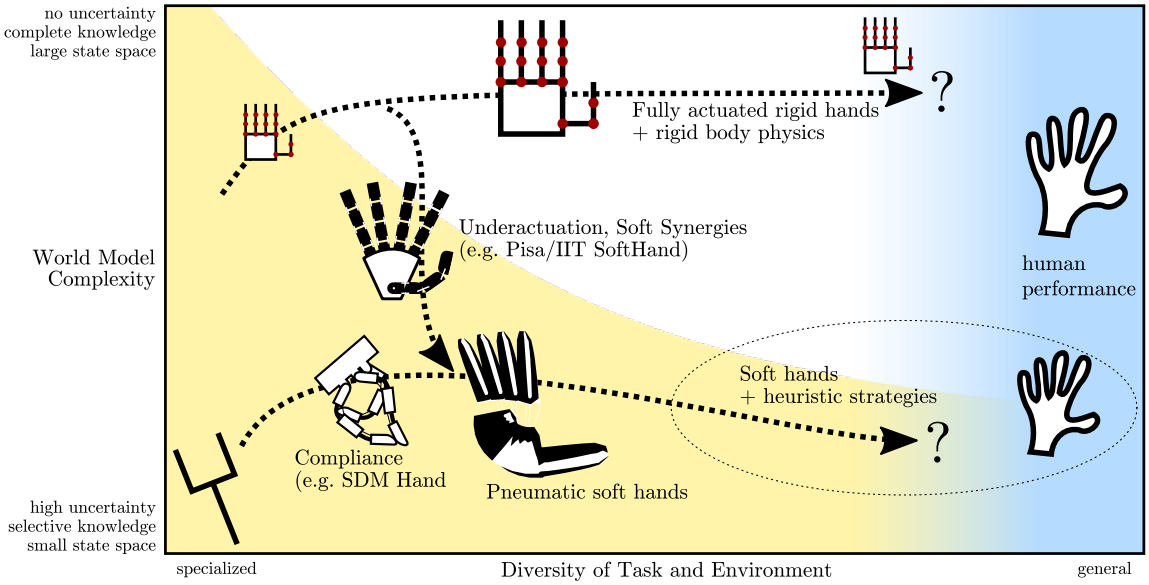

Fig. 1.2 Illustration of the differences in the approach of classical grasping research and Soft Manipulation for developing competent systems. Soft hands consider the limits of control and perception and attempt to simplify actuation commands, compensate for perceptual inaccuracies and tolerate planning mistakes, in order to maintain feasibility of the overall robot system when improving its versatility.

distinct, rigid segments), the key task of a soft hand is not to provide precise and accurate posture and motion, but to provide stable contacts, many contacts, compensation of control inaccuracies, tolerance to perceptual uncertainties and benign outcomes to planning mistakes. These features places soft hands in the lower half of Figure 1.2. In contrast, classical grasping research intends to progress along the arrow in the top half, and expects perception and control to cope with the resulting escalation of model complexity.

1.1.1 The Soft Manipulation Paradigm

In order to understand the unique challenges to soft hand design and the importance of the contributions of this thesis, we need to take a step back and make our vision on grasping with soft hands explicit. The previous section already outlined the classical view in detail, which we will refer to as the *mechanistic paradigm*. This name reflects the fact that both representation and analysis are firmly rooted in mechanics, especially contact mechanics and rigid body physics. In contrast, we propose the so called *Soft Manipulation* paradigm (elaborated in Chapter 6). In the view of Soft Manipulation:

- The main problem of grasping is to reliably obtain *a* grasp via a mechanically complex, dynamic grasp*ing* process preceding the grasp.

- Perception is inherently uncertain; the robot body either needs to cope with it or provide actions to actively reduce uncertainty affecting grasp success
- Mechanic interactions during grasping are too complex and sensitive, it does not make sense to explicitly represent them.
- Grasping behavior is composed from a bag of strategies whose implementations are necessarily bound to a specific end effector embodiment.
- Grasping strategies leverage the environment around the object to grasp to increase outcome reliability. They opportunistically exploit *environmental constraints* to motion.
- The key task of hand hardware is to provide reliable contacts and many of them. Accurate control over force or position is unnecessary.
- Grasping strategies are the main mode of generating grasping behavior for humans and robots, detailed motion planning and mechanic analysis are suboptimal fall back solutions

The Soft Manipulation view provides a coherent explanation for many developments in grasping research in recent years. A sizable number of mechanically opaque but reliable grasping strategies have been proposed [26, 68, 21, 32]. These strategies also do not require complex perception to execute. In addition, these strategies are executed not by relying on accurate positioning or force control, but by relying on their morphology (shape, articulation, coupling, compliance) to adjust and balance contact forces. Here, mechanical compliance plays a crucial role as it provides performance superior to active control. This is a key motivation to develop intrinsically soft hands. There is also increasing evidence on the importance of the immediate environment for human and robot grasping too [62, 20]. This evidence spawned the idea of intentionally *exploiting environmental constraints* in order to simplify control and planning instead of avoiding them [20]. This idea of outsourcing of control and perception to the environment fits well to the Soft Manipulation paradigm. For further information on Soft Manipulation and its proposed principles, see Chapter 6.

From the view of Soft Manipulation, soft hands are a compelling, even obvious idea. They simplify control of the interaction patterns and this way easily outperform rigid hands. Soft Manipulation offers a road to completely rethink our approach to grasping and we believe it will bring a great leap forward to the grasping competence of robots.

1.1.2 Research Questions

Whereas the idea of shifting our focus in hand design to softness and compliance promises to reinvigorate grasping research, we have to first show that pneumatic soft hands – with their unconventional actuator technology – indeed are useful to create systems capable of grasping. In this light, this thesis investigates several research questions that will help to establish the

usefulness of soft hands and by extension indicate the usefulness of the Soft Manipulation paradigm:

- How can we rapidly prototype soft hands in order to catch up with conventional hands in terms of versatility and integration, and quickly advance research in Soft Manipulation?
- Does softness as *the* guiding design principle lead to practical robot manipulators at all, or does softness make grasping more difficult as one would assume in the mechanistic view (because posture becomes less uncontrollable)?
- What are the limits to the intrinsic shape adaptability of soft hands? How much additional control is necessary to complement it?
- If hand posture and contact forces are not under the robot's direct control, how else can grasping be orchestrated?

1.2 Main Contributions and Thesis Structure

The main topic of this thesis is to present efforts towards creating capable soft hands. It contributes to the field of robotics in two major ways: First, it contributes a comprehensive set of engineering tools for building and simulating pneumatic soft hands in order to enable future scientific contributions. Second, it contributes empirical evidence for the usefulness of the Soft Manipulation paradigm in grasping, and the suitability of pneumatic soft hands for investigating and implementing grasping strategies.

Engineering contributions The main engineering contributions of this thesis are:

- We introduce a new class of robot hands, pneumatic soft hands built almost entirely from highly deformable materials and structures. They promise to fulfill the requirements of manipulators in the Soft Manipulation paradigm [20, 23, 32] much better than classical rigid-linked and tendon-driven hands.
- We advance state-of-the-art in manufacture and modeling of pneumatic soft continuum actuators, so that artifacts can be built quickly and reliably in order to empirically explore the soft hand design space and Soft Manipulation paradigm. We create a robust rapid prototyping method and accompanying tools that enable the empirical exploration of pneumatic soft hand design space. [20, 22]
- We propose a method to continuously control pneumatic soft continuum actuators named equilibrium-point control which respects their key advantage of intrinsic mechanical compliance. [25]

- We derive a simple set of design rules to predict the bending behavior of PneuFlex actuators. The rules are derived via well-informed approximation and are validated experimentally. [22]
- Leveraging recent advances in finite element simulation [114] we develop a simulator that is capable of simulating complete, contact-rich grasping behaviors of soft hands in a stable and realistic manner. In addition, the simulation is fast enough to make simulation-based automated design feasible. This performance goes considerably beyond the capabilities of existing state-of-the-art grasping simulators such as GraspIt [77] or SynGrasp [69].

Scientific contributions The main scientific contributions of this thesis are:

- We analyze observations on robot grasping and formulate principles for a new paradigm named Soft Manipulation which motivates the research into soft hands.
- We demonstrate that soft hands can grasp a surprisingly large number of object shapes without the need for sophisticated control or perception [21]. We provide an explanation using the concept of shape adaptability.
- We show that static grasp postures assumed by soft hands are as diverse as those observed with humans [23].
- We corroborate the soft synergies hypothesis from literature: hand control can be much simpler than hand posture by leveraging the compliance of soft hands [99, 5].
- Our experiments suggest that grasp posture probably is not an input to control but the outcome of control-hand-object interaction. [32]. We show that postural diversity is not explained by control diversity, so it must stem from the interaction with the grasped objects [22].
- We propose a continuous control scheme for soft pneumatic actuators that is based on an 'equilibrium point - compliance' decomposition of actuator state space. The control scheme provides superior performance to previously documented continuous control strategies of soft actuators in terms of delay and stability.
- We derive and validate an approximated mechanical model of PneuFlex actuators that enables reliable simulation of complete grasping scenes of pneumatic soft hands and with many contacts. Simulation based on this model is fast enough to make automated design feasible. The model may also be used as a forward model for control purposes.

1.2.1 Thesis Structure

The main difficulty for building and applying pneumatic soft hands is, that all aspects of such a system are novel, fledging topics of research. Because of this, no generally accepted

best practices have emerged yet. This is in stark contrast to traditional technologies such as rigid-linked, electrically torque-controlled and fully actuated robots. Therefore, the first part of this thesis aggregates a comprehensive and coherent set of best practices and tools for manufacture, morphology design, control, modeling and simulation of soft hands and their components. This part is intended for readers interested mainly in building pneumatic soft hands, or even other soft robots. The second part focuses on demonstrating the capabilities of specific soft hands and explains in detail the Soft Manipulation paradigm. This part is intended for readers interested in mainly in grasping and manipulation.

Part I

Chapter 2 reviews existing actuators that exploit compliant materials and structures for improving grasp robustness, and that can potentially be used for soft hands

Chapter 3 documents a comprehensive and coherent toolkit of methods and best practices to design, create, and assemble soft hands

Chapter 4 presents a control scheme that respects key properties of soft pneumatic actuators

Chapter 5 presents a simulation model for PneuFlex actuators and complete hands that enables fast and stable simulation of soft hands

Part II

Chapter 6 lays out the Soft Manipulation paradigm and proposes a set of related principles

Chapter 7 presents the RBO Hand 1 and RBO Hand 2

Chapter 8 provides evidence for the Shape Adaptability hypothesis with the RBO Hand 1 and demonstrates the postural dexterity of RBO Hand 2

Chapter 9 provides examples for how to implement grasping strategies successfully with soft hands

Chapter 10 concludes the thesis and gives an outlook on open issues and challenges

Part I

Tools for Soft Hand Research

Chapter 2

Fluidic Soft Continuum Actuator Designs

This chapter gives an overview over the range of existing actuators suitable for building pneumatic soft hands and manipulators.

The term continuum actuator seems to be used since the late 1990s, the earliest known mention in a paper is in one about a submarine gripper [94], where it describes an actuator which does not have links and joints in the conventional sense. Continuum actuators based on a soft, deformable structure and fluidically actuated – *fluidic soft continuum actuators* (FSCA) – were made popular recently by the so-called PneuNet [54] actuators. In contrast to more common, bellow-based pneumatic continuum actuators such as the bionic handling assistant [47] or the KITECH and FRH4 hand [103, 40], FSCAs feature no rigid support structure and a continuous deformation. They also distinguish themselves from pneumatically actuated muscles (i.e. McKibben actuators, PAMs) in that they don't rely on an external skeleton. We also specifically focus here on *fluidic* actuation as opposed to tendon-based actuation (such as the seminal soft gripper by Hirose and Umetani [50]), because it provides low mechanical impedance and has no stiction effect. Continuum actuators are also popular in research on tools for minimally invasive surgery, but the main interest in this field is on the reduction of cross section area. The comparison also does not include complementary research on modifications to make actuator stiffness controllable, such as granular jamming [2, 38, 115], layer jamming [115], or tendon-facilitated stiffening [107].

The basic idea of an FSCA is to provide a hollow beam where two opposing sides have very different stiffnesses. When the hollow is inflated, the stiffer side elongates less than the softer one, making the structure bend towards the stiffer side. Due to the anisotropy, unstable beam mechanics ("buckling") are avoided and resulting actuator motions are well defined. Individual actuator designs differ greatly in their method of creating the anisotropy in stiffness: Some use rubbers of different elasticity, others modify the cross section geometry to create thicker or thinner walls. Some designs use bellows-like segments, while yet another option is to create meta-materials by adding fibers or introducing carefully designed defects via 3D-printing. This section covers the most prominent variations of FSCAs, and analyzes their advantages and weaknesses relative to the PneuFlex design which is covered in detail in Chapter 3.

2.1 Existing Actuator Designs

The following designs, which are related to PneuFlex, are listed in chronological order, to enable the reader to trace the rapid progression of state of the art in recent years.

2.1.1 PneuNet Actuators

The PneuNet actuator [54, 70, 81] is a popular design made from two silicone rubber casts, the top part contains a series of flat, parallel cavities, while the bottom part is made of solid rubber, resulting a bellows-like structure. Sometimes a stiffer rubber is used for the bottom part to improve bending. Historically, PneuNets have been the first widely known soft continuum actuator designs based on silicone rubber.

PneuNet actuators are completely soft and can be produced in very few, simple production steps. The design process is amenable to rapid prototyping, as it relies on printed molds. In comparison to PneuFlex, these actuators can be miniaturized more easily, but require more rubber by volume for the same size. They also have a much lower maximum curvature compared to PneuFlex actuators using the same material and shape, as the rubber hull needs to stretch in two dimensions instead of one.

2.1.2 Bi-Bellows Actuators

3D-Printers capable of modifying rubber stiffness, such as the Objet series by the company Stratasys, can be used to directly print soft continuum actuators. One published design is called Bi-bellows actuator [105], which uses rings of stiff rubber around a tube of soft rubber and is shown in Figure 2.1. On one side, the rings are connected by a sheet of stiff rubber, forming the passive layer the actuator bends around.

The main advantage of this method is the freedom in structure and the ability to easily integrate many actuators in printed structures. The main drawback is, though, that due to the choice of material (a thermoplastic acrylic-based elastomer) the ratio of stiffness between soft and stiff rubber is rather limited, and that the material exhibits pronounced viscoelasticity. This severely limits the attainable performance compared to casted actuators.

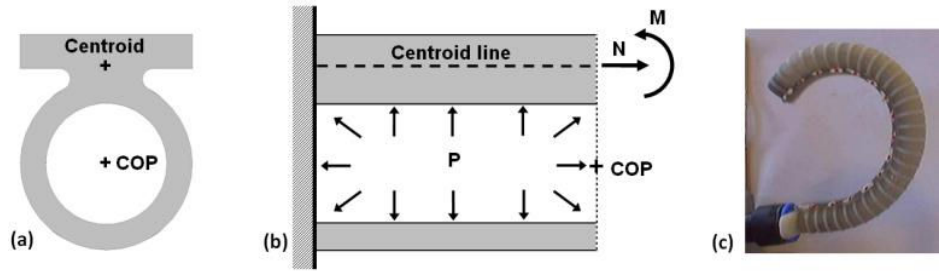

Fig. 2.1 Bi-bellows actuator. Image taken from Shapiro, Wolf, and Kósa [104], ©2012 IEEE.

2.1.3 Fiber-Reinforced Elastomeric Enclosure Actuators

Fiber-Reinforced Elastomeric Enclosures (FREE), shown in Figure 2.2, are made from rubber tubes with one to three fibers wound around them [7]. The key feature of FREEs is, that their actuated deformation can be "programmed" by choosing the winding angles of the fibers. With two fibers, actuators can be made to contract the tube (i.e. a McKibben type actuator), expand, stiffen without moving, bend, or twist along the tube. When placing two or three single FREEs in parallel, multidirectional bending can be realized too. A major restriction due to the use of tubes is, that the cross section shape has to be the same along the whole actuator. The actuator design has been replicated under different names too [16], which gives credibility to its appeal as a simple and effective design.

Research results on FREEs is especially interesting from the perspective of PneuFlex, as their results can be directly incorporated. The winding angle of the helical thread represents of PneuFlex actuators directly corresponds to the angles of two FREE fibers, while the passive layer can be translated as a third thread with angle $\alpha = 0$.

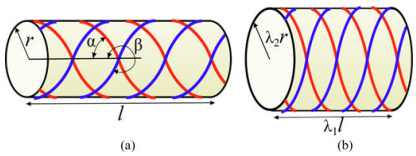

Fig. 2.2 Fiber-Reinforced Elastomeric Enclosures (FREE). Illustration taken from Bishop-Moser and Kota [6], ©2015 IEEE.

2.1.4 Elastomeric Origami Actuators

Elastomeric origami is a peculiar but interesting variation of soft continuum actuators, where origami folding techniques are used to create tubes from paper sheets that are only extensible along the tube [71]. The tubes are made airtight by coating them with silicone rubber. These actuators are capable of achieving very large curvatures. A potential problem of this approach is its reliability, though: mechanical stress is amplified at the creases, promoting material fatigue of the fibers. Another possible issue is that regular silicone does not adhere well to sheet-like materials and peels off easily.

2.1.5 Fiber-Reinforced Actuators

The Fiber-Reinforced Actuator design [41] (FRA, shown in Figure 2.3) shares a great similarity with PneuFlex actuators, as both incorporate a helical thread and a fabric layer on a casted silicone body. This makes them almost equivalent in mechanical behavior.

A notable difference is the direction from which the cavity that forms the air chamber is kept open during casting. With FRAs, the smallest side is kept open and needs to be closed subsequently. This simplifies manufacturing. On the other hand, all FRAs to date [41, 41, 87, 52, 16, 15] have been straight and with a constant cross section geometry, and curved actuators or actuators with varying cross section size may pose challenges when extracting casts from the mold. Another difference between FRAs and PneuFlex actuators is their basic shape of the cross section. FRAs use semicircles, while PneuFlex uses trapezoids. At high enough pressure – due to uniform fiber tension of the radial thread – all actuators deform their cross section into a circular shape. Similar to PneuFlex, equations for an approximative actuation model are available for FRAs [70].

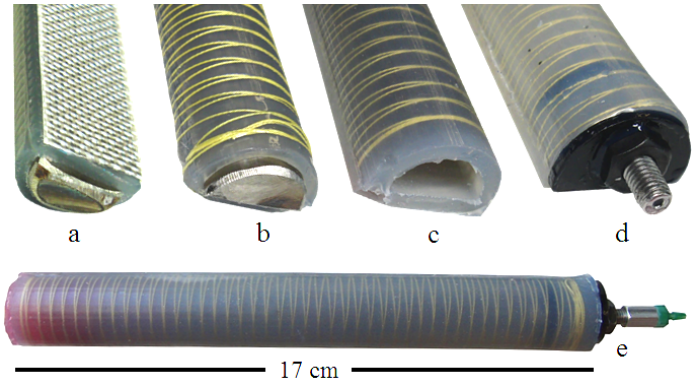

Fig. 2.3 Fiber-Reinforced Actuators. Image taken from Galloway et al. [41], ©2013 IEEE.

2.1.6 Fast-PneuNet Actuators

Fast-PneuNet actuators [79] (fPN) are an improvement of PneuNet actuators. With fPNs, the thin membrane is now vertical instead of horizontal, and also pushes against the membrane of the neighboring segment. The shape of fPN actuators resembles a bellows structure more clearly than PneuNet actuators. This avoids the "ballooning" effect of regular PneuNet actuators and results in a greatly reduced stress maxima (and therefore fatigue). As with PneuNets, fPNs consist only of rubber and a flat fabric. This simplifies manufacturing considerably by avoiding the time-consuming step of adding radial threads (such as with PneuFlex or FRAs), which makes this process suitable to building very small actuators.

2.1.7 Rotary and Bending SPA

Rotary Soft Pneumatic Actuators (Rotary SPA) and Bending SPAs [109] work similarly to PneuNet actuators, but incorporate an inextensible fabric that replaces rubber at places

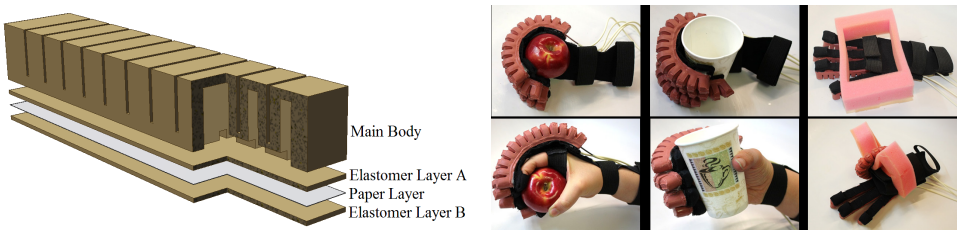

Fig. 2.4 Example of fast-PneuNet (fPN) actuators. Images taken from Polygerinos et al. [88], ©2013 IEEE.

where it is only used to stiffen the structure. This allows Rotary SPAs to bend with extreme curvatures in comparison to other actuator designs. From the point of manufacture, Bending SPA is located between PneuFlex and PneuNet design. The Rotary SPAs require the stacking of individually manufactured bellows, which adds an additional step in production. Same as with PneuNet actuators, the individual bellows are prone to ballooning, which promotes material fatigue.

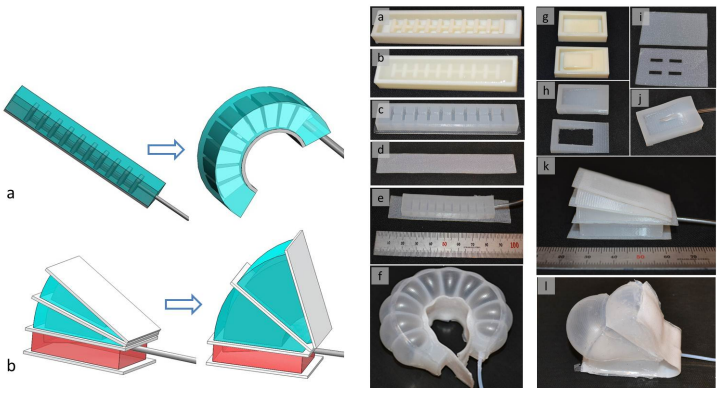

Fig. 2.5 Rotary and Bending SPAs. Image taken from Sun, Song, and Paik [109], ©2013 IEEE.

2.1.8 Miniaturized McKibben Actuators

Yet another method to create soft continuum actuators was developed by Doi et al. [28]. The authors miniaturized the well-known McKibben actuator design, down to 1.8*mm* outer diameter using a customized braiding machine. This opens up the opportunity to combine individual actuators into more complex structures, for example mimicking the morphology of an octopus tentacle [28]. The actual manufacturing process is not published. The actuators are not commercially available either. Such actuators are interesting for complementing other soft continuum actuators though, as they provide contraction instead of extension and bending.

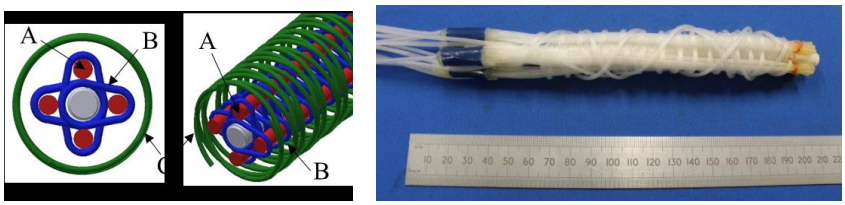

Fig. 2.6 Compound of multiple Miniature McKibben actuators. Images taken from Sun, Song, and Paik [109], ©2016 IEEE.

2.1.9 STIFF-FLOP actuators

The STIFF-FLOP project developed FSCAs for minimally invasive surgery robots. The cylindrical actuators provide two bending directions, which are controlled by three individually inflatable, fiber-reinforced actuators that are arranged symmetrically around a central tube which may contain a mechanism for changing actuator stiffness [38]. Notably, the actuator's exterior is reinforced with a custom built bellowed sheath made from a woven tube [11]. This design choice provides both excellent anisotropy of elasticity, while at the same time preventing ruptures caused by over-inflating the actuator. The manufacturing is comparatively complex though, as it requires three rubber casting and two fiber application steps. The manufacturing process for the sheath additionally precludes the construction of actuators with cross section geometries changing along the actuator.

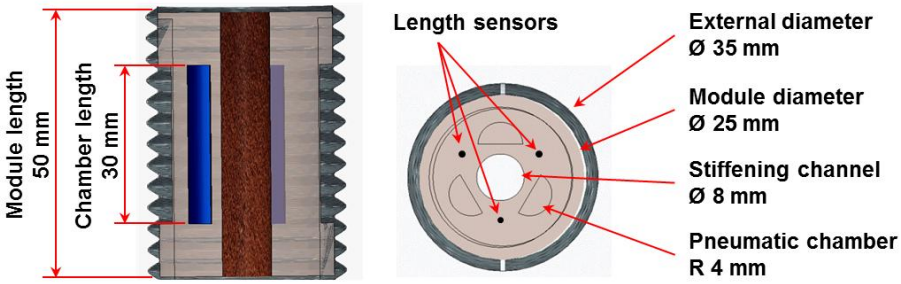

Fig. 2.7 The STIFF-FLOP actuator uses a braided bellowed sheath for reinforcing the actuator which contains three parallel chambers that are braided themselves too. Image taken from Fraś et al. [38], ©2015 IEEE.

2.1.10 Other Actuators

Some more variants of fluidic soft continuum actuator have been published, but not in the level of detail necessary for the comparative analysis. The company Pneubotics (a spin-off from the incubator Otherlab) developed pneumatic actuators based on sewn fabric enclosures [4]. The company FESTO developed a so-called bionic handling assistant, which is an elephant-trunk like robot arm where each segments is made of three parallel, inflatable bellows around a central tube [47].

2.2 Comparison

2.2.1 Distinguishing Features of PneuFlex Actuators

The PneuFlex actuator design was developed by me from early 2012 onwards, with the goal to provide a versatile and reliable method for building soft hands. The main advantage of Pneuflex actuators is, that they balance various requirements such as strength, robustness, material fatique, repeatability of production, production costs, material availability, shape design and the predictability of mechanical properties. Their manufacturing process and mechanic behavior is described in detail in Chapter 3.

PneuFlex actuators are most similar to FRAs, which were developed independently at the same time. With PneuFlex actuators though, the air chamber is kept open at the bottom side during casting. Because of this, it is very easy to vary the cross section along the actuator and to create curved actuators. As Chapter 3 will show, this enables easy variation of actuation ratio and stiffness along the actuator. Additionally, due to the opening of the bottom of the cavity during casting, it is easy to create curved actuators, to split up air chambers, and to integrate tubing or sensors inside of the actuator. Closing the air chamber requires an additional production step though, which represents the biggest drawback of the design. Work with PneuFlex actuators can also draw on the insights from FREE actuators [7], as actuation behavior can be shaped by changing the angles of the radial fibers. Finally, PneuFlex actuators have also been built by other researchers, using molds made from made from layering several laser-cut plates of acrylic [35].

2.2.2 Feature Comparison

As this chapter demonstrates, there is currently a large number of competing actuator designs available to choose from, when building soft hands. To give an overview on the main features, we compiled the properties of each technology into Table 2.1. As manufacturing

steps we only counted time-consuming ones such as casting and thread-winding, or bonding. It becomes obvious, that the PneuFlex actuator has a relatively elaborate manufacturing process, especially compared to PneuNet and fPN actuators. Related to this, we listed any specialty equipment required to manufacture the actuator. Most technologies rely on printed molds and a vacuum chamber for degassing rubber. While it is also possible to cast silicone rubbers without degassing, mechanical properties, especially ultimate strength, suffer greatly. Printing services have become wide spread too, so possession of a printer is not seen as a strict requirement and therefore put in parentheses. The next two columns (curvature and torque) indicate the mechanical limits that are realistically attainable with the given design. The main limiting factor here is the attainable anisotropy in stiffness. Fibers easily enable anisotropy factors of up to 10000, while it is difficult to obtain anisotropy greater than 10 based on varying shape (i.e. using more material volume).

The next two columns (scale up and scale down) indicate the scalability of the designs in terms of size. Here, actuators with a single material and no fibers fare well when scaling down, as it becomes increasingly harder to align parts and place fibers correctly (especially radial threads). Fiber-based actuators gain an advantage when scaling up though, as they require less rubber volume for the same strength (better strength-to-weight ratio) and therefore are less affected by the cubic increase of their own weight.

The availability of models to predict mechanical behavior is indicated by two more columns. The column of mechanical models indicates whether a model to describe actuator behavior has been published, while the column on simulation indicates whether actuators can also be simulated. While mechanics models have been published for PneuFlex [22], FRA [70] and FREE [6, 15], faithful simulation has only been demonstrated for PneuFlex (in Chapter 5) and FREEs [15] so far.

Finally, the last column assesses the difficulty of arbitrarily changing the cross section geometry, and thus the mechanical properties. For the last column, the PneuFlex actuator is the only one that not only is amenable to modulating cross section geometry, but where it is done so regularly [22, 63]. Overall, the PneuFlex actuator fares well with respect to its peers, with its main drawback being the number of manufacturing steps.

Actuator technology	Prod. steps	required equipment	materials used	high curv.	high torque	scale up	scale down	mech. models	sim. models	variable cross section
PneuFlex [21]	4	vac-chamber, (printer)	silicone, fiber, fabric	+	++	+	-	yes [22]	yes (Chap. 5)	++
FRA [41]	4	vac-chamber, (printer)	silicone, fiber, fabric	+	++	+	-	yes [70]	no	-
FREE [7]	2	none	tubes, fiber	+	+	+	-	yes [6, 15]	yes [6, 15]	-
McKibben [28]	3	braiding machine	tubes, fiber	-	+	+	+	no	no	-
fast-PneuNet [79]	2	vac-chamber, (printer)	silicone	+	+	-	+	no	no	+
PneuNet [54]	2	vac-chamber, (printer)	silicone	-	-	-	+	no	no	+
Rotary SPA [109]	2	vac-chamber, (printer)	silicone, fabric	++	-	+	-	no	no	+
Bi-Bellows [104]	1	multi-material printer	PU-rubber	-	-	-	+	no	no	+
STIFF-FLOP [11, 38]	5	vac-chamber (machining tools)	silicone, fiber braided tube	++	+	+	-	no	no	-

Table 2.1 Properties of different fluidic soft continuum actuator technologies

Chapter 3

The PneuFlex Actuator Toolkit: Design, Construction and Modeling

This chapter presents a set of methods to design, manufacture and model fluidic soft continuum actuators, and covers mechanical aspects required to assemble pneumatic soft hands.

PneuFlex actuators provide an elegant and versatile component for building soft hands, and are a core contribution of this thesis. They distinguish themselves from other existing pneumatic soft continuum actuators by their manufacturing process and the resulting available design options, such as ability to freely vary cross section geometry and to incorporate several chambers. The process allows for choosing the actuation ratio (curvature per pressure) and stiffness (change of curvature per torque) at each infinitesimal segment along the actuator. Additionally, the method allows to easily compartmentalize actuators along the main axis.

Augmenting the manufacturing process, we will also develop a set of simple design rules to estimate actuator behavior which in turn enables us to quickly tailor actuators to specific tasks.

This chapter covers three main topics: the actual manufacturing of PneuFlex based actuators, the derivation and validation of an simplified mechanical model, and design rules for ensuring actuator reliability. The chapter also includes a collection of best practices for assembling actuators into functional hands. We consider this as an important contribution too, as a common pool of knowledge on how to build reliable soft robots has yet to emerge from ongoing research. A notable initiative here is the Soft Robotics Toolkit[1] [51], which aims to provide a central collection of low cost and easy to replicate methods for building soft robots.

3.1 Actuation Principle

The basic actuation principle of soft continuum actuators is illustrated in Fig. 3.1. PneuFlex actuators follow the classical design pattern of McKibben muscles: an elastic bladder is selectively stiffened by attaching fibers (threads) to the outer hull. The fibers are aligned and, together with the rubber, form a shell of composite material with anisotropic stiffness. PneuFlex actuators are neither radially elastic, nor along the bottom layer. The combination of these two constraints creates an efficient bending motion when the actuator is pressurized. While PneuFlex actuators primarily implement a bending motion, they can be modified to perform many different deformation modes, which were enumerated by Bishop-Moser et al.on the conceptually related FREE actuators [7]. A thorough analysis of the deformation and resulting actuator behavior can be found in Section 3.4

[1] http://softroboticstoolkit.com/

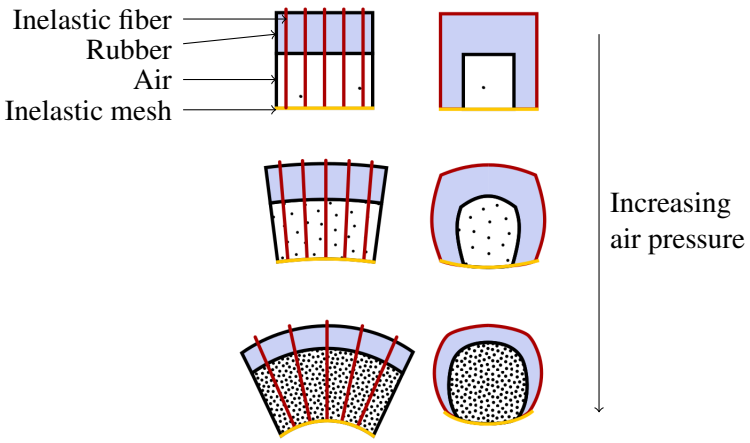

Fig. 3.1 Longitudinal cut (left) and cross section (right) of the deformation of a segment of a PneuFlex actuator when inflating it. Due to pressure, the rubber hull gets stretched, but only on the top and along the main axis, causing the actuator to bend. The required anisotropic stiffness is obtained by adding fibers.

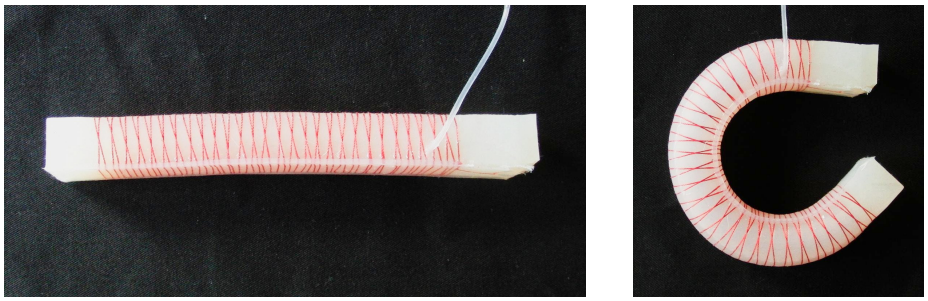

(a) Resting (b) Inflated

Fig. 3.2 Example PneuFlex actuator. The red, helical thread keeps the actuator from expanding radially when inflated. Image taken from Deimel and Brock [24].

3.2 Production Steps

The manufacturing method defines the properties and capabilities of soft continuum actuators. We carefully chose both the sequence and kind of production steps to balance them with respect to several competing, desirable actuator properties. Compared to published manufacturing methods for PneuNet [54], fast-PneuNet [79], and Fiber-Reinforced Actuators [70], the PneuFlex manufacturing process makes it especially easy to change the cross section geometry along the actuator, and to make non-straight, pre-curved actuators such as used in the palm of the RBO Hand 2.

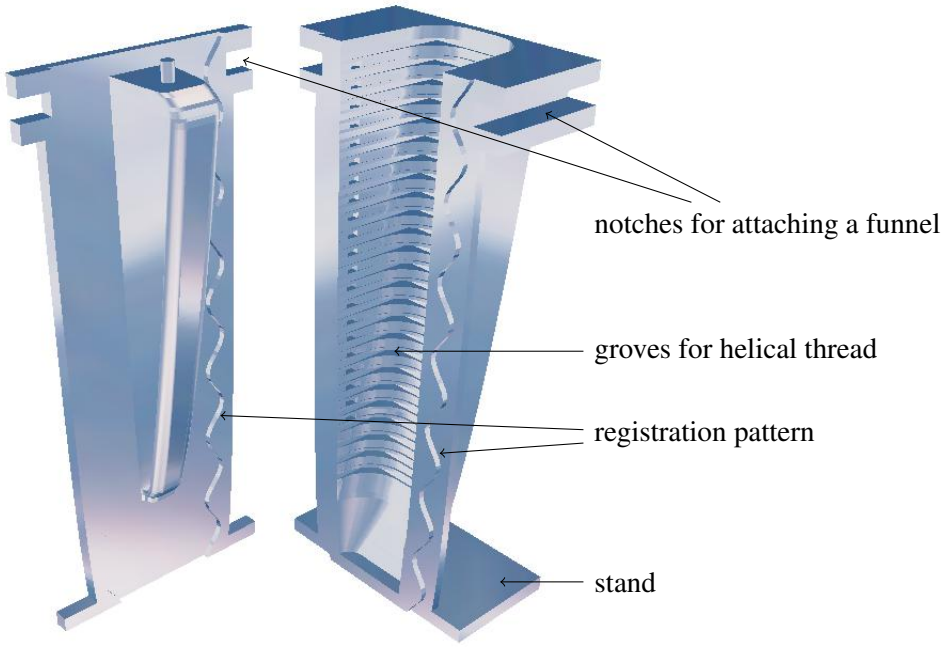

Fig. 3.3 Illustration of a two-part mold for a PneuFlex actuator, constructed automatically from a description of desired mechanical properties.

Production of an actuator can be split into two phases: the design phase and the construction phase. The former covers all steps to create a physical mold, while the latter covers all steps to create an actuator from the mold.

3.2.1 Design Phase

Before making a PneuFlex actuator, the desired actuator shape and has to be determined. The primary parameters are the thickness of the rubber hull, and the circumference of the actuator, as they define the actuation ratio and stiffness. We will derive the relationships in Section 3.4. For PneuFlex actuators, we can change both parameters easily along the actuator. Therefore, thickness and circumference are actually smooth functions parameterized on the position along the main actuator axis. Secondary parameters are the aspect ratio (height to width), and the ratio between thickness of the rubber at the side walls and the top side. We can use these parameters to shape the actuator and to affect the nonlinearity of actuation ratio and stiffness with respect to air pressure or curvature.

In addition to the cross section geometry, we can also gradually change the orientation of the cross section plane itself along the actuator.This allows us to define non-straight, curved actuators. Two examples of such curved actuators are shown in Figure 3.6. If possible though,

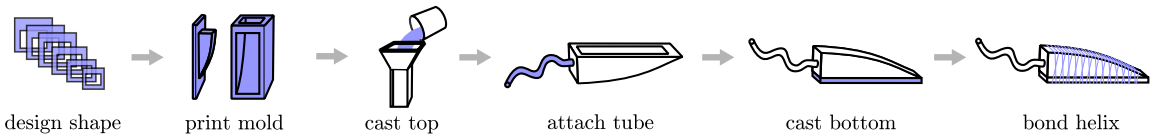

Fig. 3.4 Individual Production steps for creating a PneuFlex actuator. Figure published in Deimel and Brock [22].

the bottom sides of all cross sections should lie on a common plane, to avoid the need of additional molds for casting a non-flat passive layer.

Once the parameters are defined, we can automatically construct a mold made of two parts. An example for a mold is shown in Figure 3.3. The mold provides many shape details to make subsequent production faster and more reliable, but it also incorporates fillets in the air chamber to reduce wear during use.

In order to speed up the winding of the helical thread, the mold imparts small groves and nibbles on the outer side of the cast. On the inside, all edges are rounded to avoid stress peaks. The side walls are slightly slanted by about 3° to aid unmolding. At the interface of both mold parts, an undulating step provides a registration pattern for accurate mold alignment. It also reduces the leakage of liquid rubber during casting. The flat rim can be used to clamp both mold parts tightly together with binder clips. Molds can deform slightly because of printing or due to use. The continuous flat rim provides an easy way to remove any gaps by adding additional binder clips. A foot stand at the tip of the actuator simplifies handling during casting.

The mold is constructed as a surface mesh, and then printed out for the second phase of the creation process.

3.2.2 Production Phase

Once a mold is printed, a large number of actuators can be produced from it. The individual production steps are illustrated in Figure 3.4.

Casting the top part The printed mold parts are first assembled with binder clips, and put upright. Then silicone rubber is prepared for casting by mixing and degassing in a vacuum chamber. Section 3.3.3 provides a guideline for selecting suitable rubber materials. The prepared silicone is poured into the mold and the mold is placed into a vacuum chamber for another 5 min to 10 min to remove any trapped air. The mold is retrieved from the vacuum chamber and a piece of loop tape is placed on the opening of the mold to provide an interface

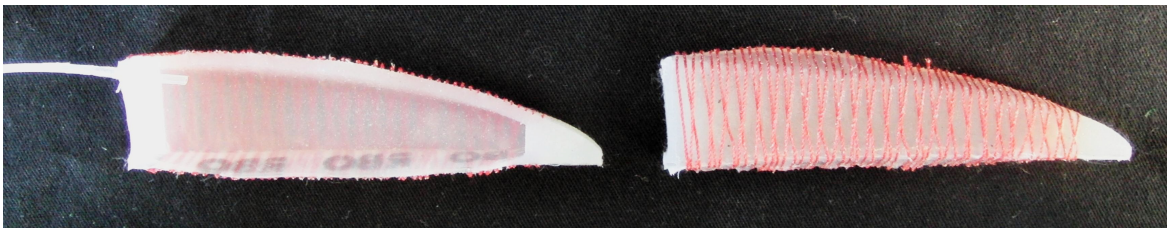

Fig. 3.5 Cross cut of a PneuFlex actuator, version `P10`. Image taken from Deimel and Brock [24].

to attach the final actuator to stiff materials, as explained in Section 3.6.2. The silicone is then left to cure completely overnight. Afterwards the finished top part is unmolded.

Attaching the tube We then install the tube to inflate and deflate the actuator. We first punch a small hole in the actuator hull at a convenient position, then insert a premanufactured silicone rubber tube. The gap between tube and top part is sealed with silicone adhesive from the inside of the air chamber to rule out air leakage.

In this step, we can also install more than one tube to accommodate for more chambers or for connecting several individual actuators directly together.

Attaching the bottom layer In the next step we close the air chamber and also add the passive layer containing an inelastic mesh fabric. For this, the mesh fabric is covered with ca. 1 mm to 2 mm of prepared silicone, and the top part is placed on top of it. The silicone is again left to cure overnight. Afterwards, the bottom layer is trimmed with scissors to match the size of the top part.

The mesh fabric used is monofilament polyester screen, which is used in the printing industry and therefore readily available. Due to being made of single, straight filaments, the fabric has almost no stretch.

Bond helix In the last step of production, the helical thread is wound around the actuator. The material used is regular, high quality PET sewing thread. The manual winding process is supported by groves in the top part, but it still represents the most time consuming manufacturing step (about 10% to 30%). Once the double helix is in place, the thread is fixated on the top and bottom side with a thin coating of prepared silicone.

After curing, the actuator is ready to use. Figure 3.5 shows an actuator made from the mold illustrated in Figure 3.3.

Fig. 3.6 The PneuFlex toolkit can be used to create actuators with many different but well defined mechanical behaviors.

3.2.3 Examples

The production method lends itself to create actuators whose mechanical properties vary along the actuator, but also to make non-straight actuators. Figure 3.6 shows several examples of different actuator shapes, all built with the method outlined in this section. The shown actuators not only vary their shape along the actuator, but also vary the thickness of the rubber hull. The two rightmost actuators show examples of non-straight PneuFlex actuators.

3.3 Considerations for Reliability and Versatility

An important goal of the PneuFlex design is to create robust and reliable actuators. We achieved this by addressing several, common point of failures of soft continuum actuators. This section elaborates on the most influential design choices.

3.3.1 Choice of Fiber Material and Thread Size

The main purpose of fibers within the actuator is to increase stiffness. To this end, materials often are selected based on their stiffness and ultimate strength, such as Kevlar fibers [87] or high-density poly-ethylene fibers (HDPE, e.g. Dyneema or Spectra brand fibers). For actuators made of silicone rubber, such extreme material properties are not necessary. We can estimate the change in radial length of the actuator in the operating range by considering the ratio of Young's modulus along and across fiber direction. The fibers are assumed to align with the radial direction, and for sake of simplicity, we only consider a simple, uniaxial load. We can then estimate the influence of anisotropy on the radial stretch:

Fiber Material (2 % added to soft silicone)	E_{axial} MPa	E_{radial} (2 % fibers) MPa	radial stretch (Eq. 3.2) ratio
(no fibers)	0.15	0.15	3.0
Stiff Silicone (1.5 MPa)	0.15	0.177	2.70
PET (2.5 GPa)	0.15	50	1.006
HD-PE (115 GPa)	0.15	2300	1.000

Table 3.1 Juxtaposition of the effect of fiber material choice on actuator deformation: PET performs similarly to HD-PE, preventing any considerable radial expansion

$$\lambda_{axial} = 1 + \frac{p}{E_{axial}}, \quad \lambda_{radial} = 1 + \frac{p}{E_{radial}}$$
$$\lambda_{radial} = 1 + \frac{p}{\frac{E_{radial}}{E_{axial}} \cdot E_{axial}} = 1 + \frac{\lambda_{axial} - 1}{\frac{E_{radial}}{E_{axial}}} \tag{3.1}$$

In order to illustrate the relationship between fiber stiffness and effect on deformation, we will fix axial stretch to a reasonably large value of $\lambda_{axial} = 3.0$ which covers the operating range of a typical actuator:

$$\lambda_{radial} = 1 + \frac{2 \cdot E_{axial}}{E_{radial}} \qquad | \, \lambda_{axial} = 3.0 \tag{3.2}$$

Furthermore,we can fix the ratio of rubber to fiber volume for the relative comparison, e.g. to 2 % which corresponds to the ratio for a typical PneuFlex actuator. We can then estimate the stiffnesses of various fiber materials:

$$E_{axial} \approx E_{rubber}$$
$$E_{radial} \approx (1 - 0.02) \cdot E_{rubber} + 0.02 \cdot E_{fiber} \tag{3.3}$$

Table 3.1 shows the resulting radial stretch that results from various material choices. While stiff silicone as fiber material (making an all-rubber actuator) does not strongly constrain radial expansion, PET (poly-ethyleneterephtalate) already does it close to the performance of HD-PE (high-density polyethylene, e.g. Dyneema and Spectra brands), which is among the stiffest fiber materials available.

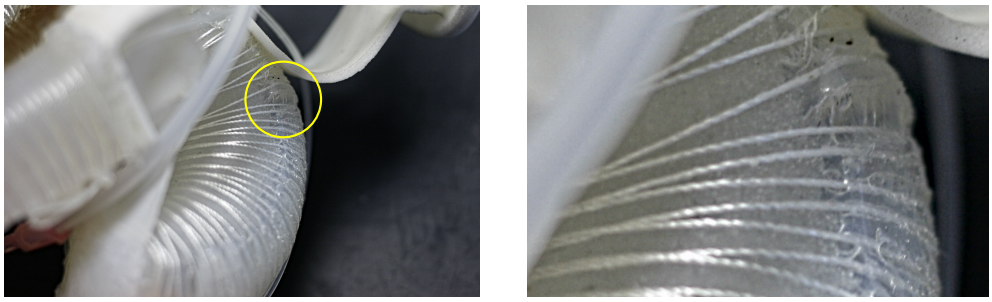

(a) Fatigued actuator (b) Detail

Fig. 3.7 Example of rubber fatigue on the palm actuator of an RBO Hand 2, induced by more than one hundred extreme inflations. It is likely that this actuator will soon rupture.

While just replacing PET with stiffer materials will not affect actuator performance, one could potentially use thinner fibers instead (ca. 40 times thinner in the case of HD-PE). Such extremely thin fibers unnecessarily exacerbate the problem of stress concentration at the contact between fiber and rubber though, and quickly exceed the tear strength of the rubber. At the extreme, these fibers simply cut through the rubber like a cheese cutter. In less extreme cases, they still lower actuator lifetime due to material fatigue, creating ruptures. The latter phenomenon can happen with PET fibers too. Figure 3.7 shows an example of developing ruptures on one of the palm actuators of the RBO Hand 2 after prolonged use. Such failures can easily be counteracted by either increasing thread diameter or by using flat braided threads to provide a large contact area. Another option would be to decrease the distance between individual threads, which lowers the force each thread has to transmit to the rubber. When the thread is wound manually, then increasing the number of turns becomes very costly as the time needed to apply the thread is the biggest cost factor in manufacture.

Compared to other potential materials (e.g. HD-PE fibers, carbon fibers), PET fibers have the advantage of being used for sewing in the textile industry, making them very cheap, easy to source, and available in many different sizes. Because of all these considerations, the default material for fibers and threads in PneuFlex actuators is PET. For restricting the circular expansion (helical reinforcement thread), PneuFlex uses 50/2 sewing thread. It has a relatively large diameter of about 0.5 mm to limit stress induced rubber fatigue.

3.3.2 Choice of Fabric for Passive Layer Reinforcement

Reinforcing the passive layer on the bottom of the actuator poses two challenges. First, the extension of the passive layer should be restricted in both axial and radial direction. At the same time the layer bends radially and axially, and assumes a saddle-like shape. Solid, flat materials such as paper, or plastic sheets have been used by some soft continuum actuator

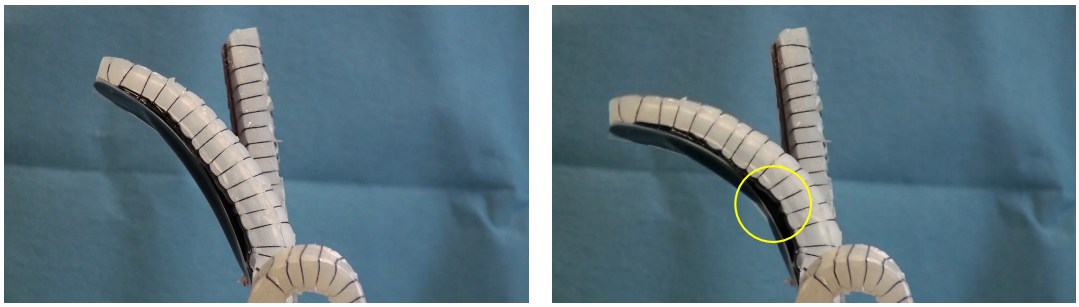

Fig. 3.8 Early actuator prototype with a sheet of polycarbonate as passive layer. The left image shows the actuator shortly after inflation, while the the right one shows the moment the actuator transitions to a new shape by buckling the sheet.

designs, but they are not able to conform to saddle shapes due to their stiffness against shear motion. Figure 3.8 shows a soft continuum actuator built with a solid sheet material as passive layer. When it is inflated, the actuator first bends radially, with the passive layer forming a cylinder segment. At some point the axial bending moments overcome the radial tension and the actuator snaps into another cylinder-segment shape, this time bent axially. Besides being an unstable, difficult to control conformation change, the transition creates huge stresses within the sheet material, puncturing or breaking it quickly. This problem is removed by using fabric instead of solid sheets. As fabrics can shear, they can conform to the saddle shape and avoid both bistable behavior and material fatigue.

The second challenge is that by nature of its stiffness the passive layer fibers will transmit practically all tensile forces along the actuator. This in turn means that these forces have to enter and exit the fiber mesh at some point (e.g. tip and base of an actuator), making the bonding between fibers and rubber of paramount importance. Unfortunately, the best performing rubber material, addition-cure Silicone rubber, exhibits negligible adhesion to almost any other material. As bonding is not an option, the only alternative is to embed fibers within the rubber body. In order to determine which fiber size is best, we can use a model from the field of fracture mechanics. This is possible as polymer fibers embedded within a solid rubber body can also be understood as a tubular defect. The Griffith micro-crack model from structure mechanics gives us a quantitative estimate. It derives a stress limit σ_{max} from material properties (Young's modulus E and surface energy G_c) and the width a of a crack within a solid material:

$$\sigma_{max} = \sqrt{\frac{4EG_c}{\pi}} \cdot \sqrt{\frac{1}{a}} \tag{3.4}$$

The first term is material dependent but constant. The second term tells us how that the stress limit increases with shrinking defect size, i.e. fiber diameter a. To maximize the

strength of rubber-fiber composites, fibers should therefore be chosen as thin as possible. Therefore, finer fabrics generally improve actuator robustness and make failure less likely. For the passive layer of PneuFlex actuators, we recommend the use of Monofilament Polyester Screen (MPS) fabric with a mesh size of 140 threads per inch (tpi). This material is widely available due to its primary use in silkscreen printing. A common fiber diameter for this type of fabric is 70 µm, which proved to be sufficiently small to not separate fibers and rubber under high stress.

3.3.3 Choice of Rubber

Choosing the optimal rubber material for a PneuFlex actuator is not trivial. This is due to the fact that in the actuator design we can trade off rubber stiffness (expressed by its shear modulus) against strain. Usually, we want both stiffness and maximum allowable strain to be as high as possible, to be able to make actuators with both large rotation and high forces. Alternatively, staying farther away from the maximum strain during normal operation will greatly increase the lifetime of the actuator. So for a given material candidate, we want to have a measure that informs us how much the material constrains the mechanical properties. Equation 3.12 gives us the relation between curvature κ, actuator height h and axial stretch λ:

$$h = \frac{\lambda_{max} - 1}{\kappa_{max}} \tag{3.5}$$

As we will see in Section 3.4.5, we should also keep the ratio between actuator hull thickness (d) and actuator height h below this limit:

$$d < 0.5 \cdot h \tag{3.6}$$

Substituting Equation 3.5 into Equation 3.6 yields the constraint:

$$d < 0.5 \cdot \frac{\lambda_{max} - 1}{\kappa_{max}} \tag{3.7}$$

We can now substitute Equation 3.5 into an estimate of the actuator's bending stiffness, Equation 3.26 which we will derive in Section 3.4.3:

$$\frac{\delta M}{\delta \kappa} = \frac{(\lambda_{max} - 1)^3}{\kappa_{max}^3} \cdot 2 \cdot G \cdot d \tag{3.8}$$

Finally, we can combine Equation 3.7 and 3.8:

$$\frac{\delta M}{\delta \kappa} < 0.5 \cdot \frac{(\lambda_{max}-1)^4}{\kappa_{max}^4} \cdot 2 \cdot G$$

$$\kappa_{max} \cdot \sqrt[4]{\frac{\delta M}{\delta \kappa}} < (\lambda_{max}-1) \cdot \sqrt[4]{G} \tag{3.9}$$

The product on the left hand side represents the trade off that can be done between stiffness and maximum curvature, while the right hand side only contains material properties, maximum stretch λ_{max} and shear modulus G It is therefore determined by the choice of material. The larger the right side term is, the more freedom we have when trading off stiffness for maximum curvature. In order to compare materials, we can use the right hand side as a material suitability index:

$$S = (\lambda_{max}-1) \cdot \sqrt[4]{G} \tag{3.10}$$

Table 3.2 gives an overview of the resulting rubber suitability for a range of popular materials. The default material used for PneuFlex actuators is DragonSkin 10. The suitability index of 26.6 is the highest of all investigated materials and indicates that this rubber is a very good choice for soft continuum actuators. Printable thermoplastic rubber, for comparison, has a suitability index that is almost three times lower. This means that printed actuators will either provide three times less maximum curvature or alternatively $3^4 = 81$ times less stiffness. The table also lists an alternative tin-cure silicone (Elastosil M4125) with a promising index of 23.5. Besides using a more cost-conscious chemistry, the material is especially interesting for making very strong (i.e. bigger) actuators. Its high shear modulus enables us to build an actuator with the same stiffness and maximum curvature as one built using DragonSkin 10, but have the actuator's diameter be reduced by about 45 %. The strength-to-weight ratio of the actuator increases by a factor of about 3.5 accordingly, which is advantageous both in terms of costs (3.5 times less rubber) and robot dynamics (3.5 times less inertia). For smaller or softer actuators (e.g. fingers of soft hands) this material may be of limited use though, as placing more radial fibers to account for the thinner hull outweighs the cost advantage of using less rubber. As Inertia already is minute for finger-size actuators, lowering it further usually does not provide any gain either.

Suitability based on tear strength The suitability index $S(G, \lambda_{max})$ should be considered as a rule of thumb and not a precise measurement. Rubbers often exhibit a nonlinear stiffening at large strains. Therefore the stress attainable at large strains can be much higher than indicated by the shear modulus which is usually measured at small strains. This effect could in principle be captured by modifying the suitability index to be based on the maximum

Material	Chemistry	Maximum stretch	Shear Modulus kPa	Suitability Index $\sqrt[4]{kPa}$
Smooth-On Dragon Skin 10	Pt-cure silicone	11	50	26.6
Smooth-On Dragon Skin 20	Pt-cure silicone	7.2	113	20.2
Smooth-On Dragon Skin 30	Pt-cure silicone	4.6	197	13.5
Smooth-On Ecoflex 00-30	Pt-cure silicone	10	23	19.7
Smooth-On Ecoflex 00-50	Pt-cure silicone	10.8	28	22.5
Wacker Chemie Elastosil M4125	Sn-cure silicone	6	333	23.5
Stratasys TangoBlack+ FLX980	Acrylic	2.7-3.2	500-230	8.0 - 8.6

Table 3.2 Table of popular rubbers and their suitability for PneuFlex actuators

tensile load σ_{max} instead:

$$S_{\text{tear strength}} = (\lambda_{max} - 1) \cdot \sqrt[4]{\frac{\sigma_{max}}{(\lambda_{max} - 1)}} \tag{3.11}$$

On the other hand, the rubber should not be operated near tear strength anyway, as this exacerbates rubber fatigue [76]. A good rule of thumb in normal operation is to limit stretch of silicone rubber to 0.3 to $0.5 \cdot \lambda_{max}$ [76]. Because of this rule, computation based on shear modulus appears to be the more reasonable choice.

3.3.4 Choice of Cross Section Shape

Every manufacturing method for a soft continuum actuator needs to solve the problem of creating a closed, convex chamber within the actuator body. The most common method of constructing a soft continuum actuator is by starting with an elastic tube [6] or by casting a tube-like part [87, 79, 70]. For the latter, molds usually are split into two or three parts, to enable easy unmolding. This tube-based approach leaves open one or two of the small faces of the actuator, which are then plugged in a subsequent step with e.g. silicone adhesives. This method lets us freely choose the basic shape of the cross section [72]. The downside of the method is, that unmolding a cast can become difficult, or even impossible when actuators are bent or have strong variations in cross section width and height.

The manufacturing method for PneuFlex follows a different strategy: the air chamber is kept open on the passive layer side of the actuator during production, as depicted in Figure 3.4. In contrast to the tube-based approach, the actuator's cross section height, width and thickness can be varied freely along the actuator, i.e. we can set a stiffness and actuation "profile" along the actuator. It is also trivial to segment the air chamber during molding to

create consecutive chambers along the actuator, or chambers in parallel to each other along the actuator, without requiring an additional assembly step. The large bottom opening of the cast also makes it easy to modify the interior, e.g. to route supply tubes, wiring, or sensors. For the manufacturing process it is advantageous to keep the passive layer flat. A twisted or bent passive layer is possible in principle, but complicates production by requiring pre-casting of the passive layer and an custom fixture for bonding together top and bottom part.

The cross section shape of PneuFlex was chosen to be trapezoidal with rounded corners. When soft continuum actuators are inflated, their cross section always assumes a circular shape, as only in this configuration the forces on the radial reinforcement fibers balance. So most soft continuum actuator designs implement circular cross sections. While the end shape is circular, it is still worthwhile to consider different shapes for the uninflated actuator. For PneuFlex actuators, the basic cross section shape is rectangular for two reasons. First, it simplifies unmolding compared to a circular shape with undercuts. The side walls of the mold are slanted slightly to create a subtle trapezoid, which greatly simplifies unmolding and avoids the need for a three-part mold. Second, the rectangular shape reduces the actuation ratio of the actuator at very low pressures and effectively linearizes the actuation ratio above a certain pressure [22]. The edges also provide a convenient point of reference for spacing the turns of the radial thread. A half-circle cross section, such as used by Polygerinos et al. [87], does not provide any clear advantage over the trapezoidal cross section.

3.4 Analysis of Actuator Behavior and Resulting Design Rules

While understanding the deformation of a PneuFlex actuator at inflation may seem a daunting task, it turns out that surprisingly simple design rules can be derived with a set of well-informed approximations. The rules do not capture the complete behavior though, but only model actuation and stiffness in the main actuated axis of each actuator segment. This derivation was initially published as an appendix of Deimel and Brock [22] and was extended to consider nonlinearity and the influence of side walls. Similar analyses have been conducted on FRAs [87] and FREEs [15] to determine actuation ratios, with similar results.

3.4.1 Formalization of the PneuFlex Actuator Geometry

Fig. 3.9 shows the parameterization of a small segment of the actuator. To simplify the model, we ignore the side walls and assume a rectangular cross section. Let x, z, h be the

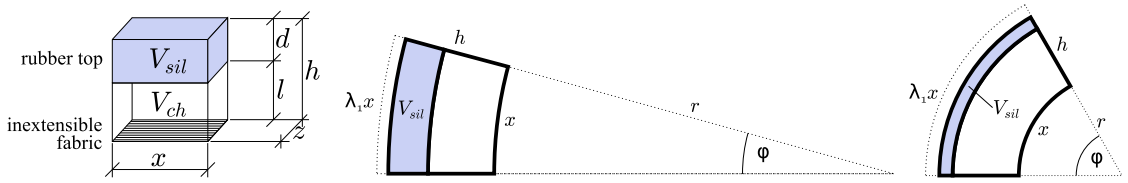

(a) Actuator segment (b) Actuator shape at different curvatures

Fig. 3.9 Parameterization of a single actuator segment: x (length), V_{sil} (rubber volume) and h (height) stay constant while λ (stretch), r (bending radius) and φ (bending angle) change. Additional parameters defining rest shape geometry are z (width), d (rubber thickness), l (air chamber height) and V_{ch} (air chamber volume). Images taken from Deimel and Brock [22].

length, width, and height of a segment of the actuator respectively. The thickness of the rubber hull is denoted with d.

Free Variables Width and height of the actuator are assumed to be constant due to the helical thread around the actuator. This assumption is facilitated by selecting an approximately circular cross section (e.g. a square) for the shape of actuator cross section, as the radial fibers will always deform the shape into circle to balance the radial pressure. Due to its embedded fabric, the bottom layer also has a fixed length x. The only possible deformation left is to stretch the silicone hull while bending the bottom layer, which is illustrated in Fig. 3.9 The interfaces of the segment are rotated to each other by the angle φ and the bottom layer curves with the radius $r = \frac{x}{\varphi}$. As we also have configurations with $\varphi = 0$ (when the actuator is deflated), we will rather express equations in terms of the curvature κ of the bottom layer:

$$\kappa = \frac{1}{r} = \frac{\varphi}{x} \quad \Rightarrow \quad \varphi = \kappa \cdot x$$

We can also express the curvature on the top side of the actuator in terms of κ:

$$\kappa_{top} = \frac{1}{\frac{1}{\kappa} + h}$$

Both κ and κ_{top} are defined on the same angle φ. Therefore we can compute a relationship between angle φ and stretch λ_1:

$$\begin{aligned}
\varphi &= \varphi_{top} \\
\kappa \cdot x &= \frac{1}{\frac{1}{\kappa} + h} \cdot \lambda_1 x \\
\kappa &= \frac{\lambda_1 - 1}{h} && (3.12) \\
\lambda_1 &= 1 + \kappa \cdot h && (3.13) \\
\varphi &= \frac{x}{h} \cdot (\lambda_1 - 1) && (3.14)
\end{aligned}$$

Volumes To aid readability of the analysis, we define several volume constants that do not change under deformation. These volumes can be computed from the basic actuator geometry. The volume of the effectively incompressible silicone in the active layer of the actuator is:

$$V_{sil} = z \cdot x \cdot d$$

The total volume of the *deflated* air chamber is:

$$V_{ch} = z \cdot x \cdot (h - d)$$

The total volume of the *deflated* actuator is:

$$\begin{aligned}
V_{act} &= z \cdot x \cdot h = \frac{h}{d} \cdot V_{sil} && (3.15) \\
&= V_{ch} + V_{sil} && (3.16)
\end{aligned}$$

The total volume of air contained in the *deflated* actuator plus any volumes connected to it, such as supply tubes is:

$$V_{air} = V_{supply} + V_{ch} = V_{supply} + V_{act} - V_{sil}$$

The symbol V will be reserved to denote the *actual* volume of the air chamber, which is dependent on the deformation. Therefore it is a function of actuator curvature. The total actual volume of the actuator is $V + V_{sil}$.

Volume Change To compute the energy stored by the compressed gas (air) within the actuator, we need to compute the actual volume with respect to actuator curvatures. We can

do this by first calculating the total volume of a flexed actuator segment:

$$\begin{aligned} V + V_{sil} =& z \cdot \frac{\varphi}{2\pi} \cdot \left(\pi \cdot \left(\frac{x}{\varphi} + h \right)^2 - \pi \cdot \left(\frac{x}{\varphi} \right)^2 \right) \\ =& V_{act} \cdot \left(1 + \frac{h}{2} \frac{\varphi}{x} \right) \end{aligned}$$

As $\frac{\varphi}{x} = \kappa$, we can express actuator curvature in terms of air chamber volume and initial geometry as:

$$\begin{aligned} V + V_{sil} =& V_{act} \cdot \left(1 + \frac{h}{2} \cdot \kappa \right) \\ \kappa =& \frac{2}{h} \left(\frac{V + V_{sil}}{V_{act}} - 1 \right) \\ =& \frac{2}{h} \cdot \left(\frac{V - V_{ch}}{V_{act}} \right) \end{aligned}$$

With Equation 3.12 we can also compute the relationship between λ_1 and the actuator volume:

$$\lambda_1 = 1 + 2 \cdot \left(\frac{V - V_{ch}}{V_{act}} \right) \tag{3.17}$$

This leads to the first insight: actuator curvature and stretch of the silicone rubber are linearly proportional to the gas volume:

$$\begin{aligned} \partial \kappa =& \frac{2}{V_{act} \cdot h} \cdot \partial V \\ \partial \lambda_1 =& \frac{2}{V_{act}} \cdot \partial V \end{aligned}$$

Strain Tensor Invariants The energy stored in the rubber during deformation is modeled using strain tensor invariants [43]. The strain tensor invariants are related to the orthogonal stretches λ_1, λ_2, λ_3 by:

$$\begin{aligned} J_1 =& \lambda_1^2 + \lambda_2^2 + \lambda_3^2 - 3 \\ J_2 =& \lambda_1^2 \lambda_2^2 + \lambda_1^2 \lambda_3^2 + \lambda_2^2 \lambda_3^2 - 3 \\ J_3 =& \lambda_1 \cdot \lambda_2 \cdot \lambda_3 - 1 \end{aligned}$$

Silicones are almost incompressible ($\nu \approx 0.48$), therefore we can assume a constant volume:

$$\lambda_1 \cdot \lambda_2 \cdot \lambda_3 = 1$$

Therefore, J_3 is constant and can be ignored when computing energy gradients. To compute J_1 and J_2, we first define actuator-specific relations between stretches λ_1, λ_2, λ_3 in three principal directions, which are aligned to x, h and z respectively. The actuator's radial size does not change either because of the reinforcement helices. We therefore set the circumferential stretch $\lambda_3 = 1$, and get the relationship:

$$\lambda_2 = \lambda_1^{-1}$$

This deformation is also called pure shear. Using these relations, both J_1 and J_2 reduce to:

$$J_2 = J_1 = \lambda_1^2 + \lambda_1^{-2} - 2 \tag{3.18}$$

Simplifications and Limitations To keep the model simple, many potentially important effects are not included. We assume a uniform strain energy density within the rubber hull, which is acceptable for moderately thin rubber hulls (i.e. $d < 0.5h$, as discussed in Section 3.4.5). Furthermore, we use a Neo-Hookean material model. This ignores higher order deformation effects. The error is less than 3.4% though, as discussed in Section 3.4.6. We also ignore material stiffening, because the maximum error is less than 7.7% as discussed in Section 3.4.7. The model can also be invalidated by externally applying large compressive forces: they can remove fiber tension in the passive layer which then causes those fibers to buckle. The resulting change in stiffness is not modeled. Despite the many approximations we needed to derive compact equations, we will see in Section 3.5 that the design rules predict actuator behavior to a large extent.

3.4.2 Statically Stable Actuator Configurations

To derive the static deformation of a PneuFlex actuator, we can use the minimum potential energy principle. For this, we first need to define all relevant forms of work in the system: Gas compression, elastic rubber deformation, and work added by an external load. The total potential energy of the actuator therefore is:

$$W = W_{air} + W_{sil} + W_{load} \tag{3.19}$$

Equilibrium is reached, when the gradient of work is zero. In our case, we will express all work in terms of a single free variable, λ_1, and then compute:

$$\frac{\Delta W}{\Delta \lambda_1} = 0$$

The remainder of this section derives each work component from the definitions of the previous section and state the resulting equation for statically stable configurations.

Gas Compression Work For computing the gas compression work of the air within the actuator, we need to differentiate between two different control regimes. In the mathematically simpler case, pressure is held constant under deformation: $p(V) = p$. This is either done actively by using a control system or passively by using a big reservoir connected to the actuator volume, which attenuates the effect of volume change within the actuator on pressure. In the second, more common case the total enclosed gas mass in the system is held constant e.g. when using pneumatic valves. According to the ideal gas law, pressure changes as $p(V) = nRT \cdot \frac{1}{V}$. A closed gas volume slightly increases the stiffness of the actuator. For the sake of brevity though, the latter case will not be derived here. In both cases, the work done by changing the volume of a gas from V_1 to V_2 is:

$$W_{air} = W_{V_1} - \int_{V_1}^{V_2} p(V) \cdot dV$$

In the case of constant gas pressure, we get a simple equation:

$$\begin{aligned} W_{air} &= W_0 - p \cdot (V) \\ \frac{\delta W_{air}}{\delta \lambda_1} &= - p \cdot \frac{\delta V}{\delta \lambda_1} \end{aligned}$$

$$\frac{\delta W_{air}}{\delta \lambda_1} = -p \cdot \frac{1}{2} V_{act} \tag{3.20}$$

Rubber Deformation Work The deformation work of the silicone rubber W_{sil} is modeled as a *Neo-Hookean solid* model with coefficient $C_{10} = \frac{G}{2}$:

$$W_{sil} = \int_{V_{sil}} \frac{G}{2} \cdot J_1 \cdot \delta V$$

G is the material's shear modulus, and V_{sil} the volume of the silicone. We assume a uniform deformation, and thus uniform strain energy density (i.e. uniform J_1) throughout the hull, as justified in Section 3.4.5. We can then calculate the total strain energy as:

$$W_{sil} = \frac{G}{2} \cdot J_1 \cdot V_{sil}$$

Using Equation 3.18, we can express the work gradient w.r.t. stretch λ_1:

$$\begin{aligned} W_{sil} =& \frac{G}{2} \cdot (\lambda_1^2 + \lambda_1^{-2} - 2) \cdot V_{sil} \\ \frac{\delta W_{sil}}{\delta \lambda_1} =& G \cdot \left(\lambda_1 - \lambda_1^{-3}\right) \cdot V_{sil} \end{aligned} \tag{3.21}$$

Load Work For a given actuator segment, external load is applied on the interfaces to the two adjacent segments. By attaching our frame of reference to one side of the actuator segment, load work can can be computed by only considering the motion and force of the opposite side. Load work can further be split up into the work done by translatory forces and rotary moments. Translatory forces are transmitted by the inelastic fibers of reinforcement helix and passive layer. If we assume completely inelastic fibers, those forces do not contribute any work. Rotation, on the other hand, does contribute work, and we can integrate the contribution along the bottom layer:

$$W_{load} = \int M(\varphi) \cdot d\varphi$$

For the model, it is more convenient to integrate over x instead of φ along the actuator segment. We can rewrite the integral to:

$$W_{load} = \int M(\varphi(x)) \cdot \frac{\partial \varphi(x)}{\partial x} dx$$

For short enough actuator segments (small x) we can assume constant, averaged moment along the whole segment, i.e. $M(x) = M$. Additionally we can substitute $\frac{\partial \varphi(x)}{\partial x}$ with the

derivative of Equation 3.14:

$$\begin{aligned} W_{load} &= \int M \cdot \frac{\lambda_1 - 1}{h} \cdot dx \\ &= M \cdot \frac{\lambda_1 - 1}{h} \cdot x + W_0 \end{aligned}$$

From this equation, we can compute the work gradient w.r.t. stretch λ_1:

$$\frac{\delta W_{load}}{\delta \lambda_1} = M \cdot \frac{x}{h} \tag{3.22}$$

Minimum Total Potential Energy We can now apply the minimum potential energy principle and compute the equilibrium configuration, which defines the shape the actuator attains given enough time. We compute the local minimum of Equation 3.19 w.r.t. the single free variable λ_1 with the help of the previously derived gradients 3.20, 3.21 and 3.22, we obtain an equation which describes all stable actuator states:

$$\begin{aligned} 0 = &\quad \frac{\delta W_{air}}{\delta \lambda_1} \quad + \quad \frac{\delta W_{sil}}{\delta \lambda_1} \quad + \quad \frac{\delta W_{load}}{\delta \lambda_1} \\ 0 = &- p \cdot \frac{V_{act}}{2} + G \cdot \left(\lambda_1 - \lambda_1^{-3}\right) V_{sil} + M_{load} \cdot \frac{x}{h} \end{aligned} \tag{3.23}$$

3.4.3 Stiffness

The stiffness of an actuator segment is expressed by the change in moment M_{load} w.r.t. curvature κ. From Equation 3.23 we can compute M_{load} explicitly:

$$M_{load} = \quad \frac{h^2 \cdot z}{2} \cdot p - \left(\lambda_1 - \lambda_1^{-3}\right) \cdot G \cdot h \cdot d \cdot z$$

As we assume a constant pressure regime, the first term vanishes when differentiating:

$$\frac{\delta M_{load}}{\delta \lambda_1} = -G \cdot h \cdot d \cdot z \cdot (1 + 3 \cdot \lambda_1^{-4})$$

We then substitute with Equation 3.13 and its derivative $\partial \lambda_1 = h \cdot \partial \kappa$ to yield an equation dependent on curvature. Additionally, we can isolate the influence of the the aspect ratio $\frac{z}{h}$, as usually it is approximately 1. We then arrive at the equation describing the stiffness of the

actuator given its shape and deformation:

$$\frac{\delta M_{load}}{\delta \kappa} = 2 \cdot h^3 \cdot G \cdot d \quad \cdot \quad \frac{z}{h} \quad \cdot \quad \frac{1+3(1+h\kappa)^{-4}}{2} \tag{3.24}$$

The last, nonlinear factor predicts that a strong stiffening when a PneuFlex actuator is straight or even negatively curved. This sudden stiffening is indeed observed with real actuators, but they also tend to buckle under such loads.

Scaling Law In order to arrive at a scaling law, we can approximate the latter two terms to be constant. We then get the simple design rule:

$$\frac{\delta M_{load}}{\delta \kappa} \approx 2 \cdot h^3 \cdot G \cdot d \tag{3.25}$$

This approximation underestimates tangent stiffness at high curvature by a factor of 2 and overestimates it at zero curvature by a factor of 0.5.

When scaling an actuator, the ratios $\frac{d}{h}$ and $\frac{z}{h}$ stay constant. The equation then becomes:

$$\frac{\delta M_{load}}{\delta \kappa} = h^4 \cdot \left(2 \cdot G \cdot \frac{d}{h} \cdot \frac{z}{h} \cdot \frac{1+3(1+h\kappa)^{-4}}{2} \right)$$

Stiffness therefore scales to the *fourth* power of actuator size. This gives us a powerful lever to adjust the strength of an actuator with only minute changes in actuator size.

Non Squared Cross Sections PneuFlex actuators can also have non-square cross sections. The influence of the aspect ratio can be understood by realizing that all actuators eventually deform into a circular cross section when being inflated. This happens, because the stable configuration of the helical thread from the applied uniform radial pressure is a circle. Vice versa, the resting shape aspect ratio only influences actuator behavior at no or low air pressure. Therefore, we probably get better estimates for higher pressures when we use the circumference c instead of height h and width z to compute actuator stiffness, irregardless of the aspect ratio:

$$\frac{\delta M_{load}}{\delta \kappa} = \left(\frac{c}{4}\right)^3 \cdot 2 \cdot G \cdot d \cdot \frac{1+3(1+h\kappa)^{-4}}{2} \approx \left(\frac{c}{4}\right)^3 \cdot 2 \cdot G \cdot d \tag{3.26}$$

Compensation of Side Walls Until now, the influence of the side walls on the stiffness of the theoretic model has been ignored. In order to do a rough estimation, we can assume that the contribution of a small area of rubber of the cross section to contribute to total stiffness

with the third power of height (Eq. 3.26):

$$\frac{\Delta\frac{\delta M_{load}}{\delta\kappa}}{\Delta h} = h^3 \cdot (2 \cdot G) \cdot d \cdot \frac{1+3(1+h\kappa)^{-4}}{2} \cdot \Delta h \tag{3.27}$$

This gives us an estimate for the contribution to stiffness by the side walls which we ignored so far:

$$\frac{\delta M_{load}}{\delta\kappa}_{\text{sidewalls}} = \frac{1}{4}(h-d)^4 \cdot \left(d_{\text{left}} + d_{\text{right}}\right) \cdot \left(2 \cdot G \cdot \frac{1+3(1+h\kappa)^{-4}}{2}\right) \tag{3.28}$$

This stiffness can be added to Eq. 3.26, as it operates in parallel. For convenience, we can express the contribution as a correction factor normalized on the stiffness rule of Eq. 3.26:

$$\text{contribution}_{\text{side walls}} = \frac{\frac{\delta M_{load}}{\delta\kappa}_{\text{sidewalls}}}{\frac{\delta M_{load}}{\delta\kappa}} = \frac{1}{4}\left(\frac{h-d}{h}\right)^4 \cdot \frac{\left(d_{\text{left}} + d_{\text{right}}\right)}{d} \tag{3.29}$$

This factor is also invariant to actuator size, i.e. it only depends on the shape of the cross section. Therefore it does not interfere with the findings of the analysis so far. Additionally, it is also invariant to curvature κ, making it simple to precompute. For a typical actuator shape with $d_{\text{left}} = d_{\text{right}} = d$, $z = h$ and a relatively thin hull $d \approx 0.1 \cdot h$, the side walls increase actuator stiffness by 32%. For thick hulls ($d \approx 0.3$) the contribution drops to 12%.

3.4.4 Actuation Ratio

The actuation ratio $\frac{\delta\kappa}{\delta p}$ is the change of curvature given an increase in pressure while assuming zero load. It can be computed from Equations 3.23 and 3.15:

$$\begin{aligned} \frac{p}{2} &= \left(\lambda_1 - \lambda_1^{-3}\right) \cdot G \cdot \frac{V_{sil}}{V_{act}} \\ p &= 2 \cdot \left(\lambda_1 - \lambda_1^{-3}\right) \cdot G \cdot \frac{d}{h} \\ \frac{\delta\lambda_1}{\delta p} &= \frac{1}{\left(1+3\lambda_1^{-4}\right) \cdot 2 \cdot G \cdot \frac{d}{h}} \end{aligned} \tag{3.30}$$

Using Equation 3.13 we can substitute λ_1 and $\delta\lambda_1$. We get the actuation ratio:

$$\frac{\delta\kappa}{\delta p} = \frac{2}{\left(1+3\left(1+h\kappa\right)^{-4}\right)} \cdot \frac{1}{4 \cdot G \cdot d} \tag{3.31}$$

So according to the simple model, the actuation ratio is inversely proportional to the silicone's shear modulus and its thickness. The actuation ratio also has a nonlinear component with respect to the actual curvature. At small curvatures the actuation ratio is considerably lower than at higher curvatures. The nonlinear term yields values in the range of $\frac{1}{2}$ to 2.

In order to arrive at an approximation useful for actuator design, we can fix the nonlinear term to 1. Additionally, the side walls contribute roughly the same amount of elastic energy gradient as the top hull (as will be shown in the subsequent paragraph), which further reduces the actuation ratio by about a factor of 2. Putting these factors together, we get the following design rule:

$$\frac{\delta\kappa}{\delta p} \approx \frac{1}{8 \cdot G \cdot d} \tag{3.32}$$

Note that this equation is independent of both h and z (and therefore also circumference c). The actuation ratio is not dependent on the size of the actuator cross section! We can therefore set an actuation ratio profile using thickness and shear modulus of the rubber hull, and then set the stiffness profile with:

$$\frac{\delta M_{load}}{\delta\kappa} \approx \left(\frac{c}{4}\right)^3 \cdot \frac{1}{4 \cdot \frac{\delta\kappa}{\delta p}} \tag{3.33}$$

Compensation of Side Walls In order to estimate the influence of the side walls on the actuation ratio, we can assume that the elastic energy gradient of a small volume of rubber rises proportional to the distance y from the passive layer, i.e. $\lambda_1(y) = \frac{\lambda_1}{h} \cdot y$. This approximation basically ignores the λ_1^{-3} term in Equation 3.21, but greatly simplifies the estimate.

$$\begin{aligned}
\frac{\delta W_{\text{left}}}{\delta\lambda_1} &\approx G \cdot d_{\text{left}} \cdot x \cdot \int_{y=0}^{h-d} \frac{\lambda_1}{h} \cdot y\, dy \\
&= G \cdot d_{\text{left}} \cdot x \cdot \lambda_1 \cdot \frac{(h-d)^2}{2 \cdot h} \\
&= G \cdot d \cdot x \cdot z \cdot \lambda_1 \cdot \frac{(h-d)^2}{2 \cdot h \cdot z} \cdot \frac{d_{\text{left}}}{d} \\
&= \left[\frac{(h-d)^2}{2 \cdot h \cdot z} \cdot \frac{d_{\text{left}}}{d}\right] \cdot \frac{\delta W_{sil}}{\delta\lambda_1}
\end{aligned} \tag{3.34}$$

Note that this approximation slightly overestimates the elastic energy gradient close to the passive layer. But this error is also partly offset by ignoring the contribution of the passive layer to overall stiffness. We can now replace the elastic energy gradient with the better

approximation:

$$\frac{\delta W'_{sil}}{\delta \lambda_1} = \frac{\delta W_{sil}}{\delta \lambda_1} + \left[\frac{(h-d)^2}{2 \cdot h \cdot z} \cdot \frac{d_{\text{left}}}{d}\right] \cdot \frac{\delta W_{sil}}{\delta \lambda_1} + \left[\frac{(h-d)^2}{2 \cdot h \cdot z} \cdot \frac{d_{\text{right}}}{d}\right] \cdot \frac{\delta W_{sil}}{\delta \lambda_1}$$

$$\frac{\frac{\delta W_{sil}}{\delta \lambda_1}}{\frac{\delta W'_{sil}}{\delta \lambda_1}} = \frac{1}{1 + \frac{(h-d)^2}{h \cdot z} \cdot \frac{d_{\text{left}} + d_{\text{right}}}{2 \cdot d}} = \frac{1}{2} \cdot \text{ratio}_{\text{sidewalls}} \tag{3.35}$$

When we assume that actuators deform into circular shape, we can also write:

$$\frac{1}{2} \cdot \text{ratio}_{\text{sidewalls}} = \frac{1}{1 + \left(\frac{h-d}{h}\right)^2 \cdot \frac{d_{\text{left}} + d_{\text{right}}}{2 \cdot d}} \tag{3.36}$$

In order to compensate the actuation ratio for the side walls, we can augment the elastic energy gradient in Equation 3.23 with the estimated factor $\frac{1}{2} \cdot \text{ratio}_{\text{sidewalls}}$ and get:

$$\frac{\delta \kappa}{\delta p} = \text{ratio}_{\text{sidewalls}} \cdot \frac{2}{\left(1 + 3\,(1 + h\kappa)^{-4}\right)} \cdot \frac{1}{8 \cdot G \cdot d} \tag{3.37}$$

Note that $\text{ratio}_{\text{sidewalls}}$ was chosen in such a way that it becomes 1.0 in the common case where $z = d$ (quadratic cross section) and $d_{\text{left}} = d_{\text{right}} = d$, and $\frac{d}{h} \approx 0$. It is easy to see that in this case the design rule Equation 3.32 approximates the actual actuation ratio well.

3.4.5 Approximation: Uniform Strain Energy Density Within Rubber Hull

In the model we assume a uniform strain energy density throughout the hull. This claim needs to be supported though, as the principal stretches are not uniform at all.

Formalization For an infinitesimal volume of elastomer within the hull, we define d to be the radial distance of the volume from the outer boundary of the hull in an undeformed actuator, while d' denotes the actual radial distance in the deformed actuator.

When the actuator bends, the volume moves radially outwards as the wall thins. This motion influences the stretches encountered. As the radial displacement is limited by the helical reinforcement fibers, we can assume the outer boundary of the rubber hull to not move radially at all.

Due to the reduced distance from the passive layer the longitudinal stretch λ_1 becomes smaller with increasing d':

$$\lambda_1 = 1 + \left(\kappa \cdot h - \kappa \cdot d'\right) \tag{3.38}$$

The circumferential stretch λ_3 can be calculated by the radial displacement given a position d' with respect to the undeformed position d:

$$\begin{aligned} \delta\lambda_3 =& \frac{\pi\,(h-d')}{\pi\,(h-d)} - \frac{\pi\,(h-d'-\delta d')}{\pi\,(h-d)} \\ =& -\frac{\delta d'}{h-d} \\ \Rightarrow \lambda_3 =& \frac{-d'}{h-d} + C \end{aligned}$$

Setting the boundary condition $\lambda_3 = 1$ at the outer boundary of the hull yields:

$$\lambda_3 = \frac{h-d'}{h-d} \tag{3.39}$$

Finally, we can derive λ_2 by using the incompressibility assumption $\lambda_1\lambda_2\lambda_3 = 1$ and get:

$$\lambda_2 = \frac{h-d}{\kappa \cdot h^2 + \kappa \cdot d'^2 - (2 \cdot \kappa \cdot h + 1)\, d' + h} \tag{3.40}$$

To normalize our calculations, we can express the principal stretches in terms of the dimensionless ratios $\frac{d'}{h}$,$\frac{d}{h}$, and $\kappa{\cdot}h$:

$$\lambda_1 = 1 + \kappa{\cdot}h \cdot \left(1 - \frac{d'}{h}\right) \tag{3.41}$$

$$\lambda_2 = \frac{1 - \frac{d}{h}}{\kappa{\cdot}h + \kappa{\cdot}h \cdot \left(\frac{d'}{h}\right)^2 - (2 \cdot \kappa{\cdot}h + 1)\,\frac{d'}{h} + 1} \tag{3.42}$$

$$\lambda_3 = \frac{1 - \frac{d'}{h}}{1 - \frac{d}{h}} \tag{3.43}$$

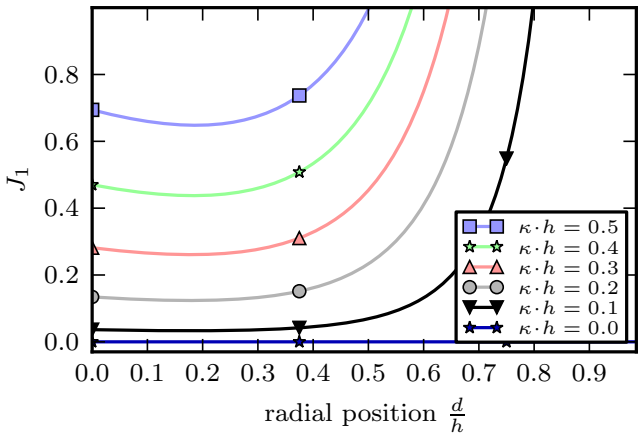

Fig. 3.10 Strain tensor strength within the rubber hull for different normalized curvatures. Figure published in Deimel and Brock [22] ©2016 Sage Publications.

With λ_2 we can express the relation between d' and d as a linear differential equation using λ_2 as the gradient of displacement:

$$\begin{aligned} \frac{\delta d'}{\delta d} &= \lambda_2 \\ \frac{\delta d'}{\delta d} &= \frac{1 - \frac{d}{h}}{\left(\frac{d'}{h}\right)^2 \kappa \cdot h - \frac{d'}{h}\left(2 \cdot \kappa \cdot h + 1\right) + 1 + \kappa \cdot h} \end{aligned} \tag{3.44}$$

This differential equation determines the position d' of a packet of rubber, and therefore its deformation.

Strain Energy Distribution To analyze the strain energy throughout the hull, we compute its main contributor, the strain tensor J_1. This is done by first solving Equation 3.44 numerically to yield the actual position d' for each (d, κ) tuple. The boundary conditions are set at the outer boundary of the hull to $d' = 0$ to $\lambda_1 = \frac{1+\kappa h}{}$, $\lambda_2 = 1$ and $\lambda_3 = \frac{1}{\lambda_1}$. Figure 3.10 shows the resulting strain tensor J_1 with respect to the normalized depth $\frac{d}{h}$ within the hull and at different normalized curvatures $\kappa \cdot h$. We can see that J_1 stays surprisingly flat even for moderately thick hulls and at very strong curvatures. The reason is, that with increasing d the increase in λ_3^2 (circumferential) is offset by a reduction in λ_1^2 (longitudinal) and λ_2^2 (radial). The analysis shows that as long as the hull thickness is less than about half the actuator height, we can safely assume a uniform strain energy distribution for modeling. Staying below this limit also prudent in terms of reliability, as it avoids material fatigue of the rubber on the inside of the air chamber.

3.4.6 Approximation: Neo-Hookean Deformation

A more sophisticated alternative to the simple Neo-Hookean deformation model used in our model is the generalized Mooney-Rivlin model for incompressible hyperelastic materials. It states a polynomial instead of linear approximation of strain energy density, based on a polynomial expansion of the strain tensor invariants J_1 and J_2:

$$\frac{dW}{dv} = \sum_{i,j=0}^{n} C_{ij} \cdot J_1^i \cdot J_2^j$$

Silicone rubbers have rather small coefficients for C_{01}, C_{02} and C_{20} though. The coefficients published by Meier, Lang, and Oberthür [76] have the following scale:

$$\begin{aligned} C_{01} &\approx \frac{1}{50} \cdot C_{10} \\ C_{20} &\approx \frac{1}{500} \cdot C_{10} \\ C_{02} &\approx 0 \end{aligned}$$

Setting all coefficients except C_{10} to zero yields the Neo-Hookean model. We can compute the error made by this approximation. For this, we need to set a limit to the highest stretch we encounter in our actuator, which we set to about $\lambda_1 < 3$. This stretch relates to a highly curved actuator bent with a radius of half its height. Equation 3.18 then bounds the strain tensors to:

$$J_1 < 7.11$$

$$J_2 < 7.11$$

The terms dropped from the Mooney-Rivlin model are therefore less than:

$$\begin{aligned} C_{01} \cdot J_2 &< 0.02 \cdot C_{10} \cdot J_1 \\ C_{20} \cdot J_1^2 &< 0.014 \cdot C_{10} \cdot J_1 \end{aligned}$$

Which results in an underestimation of stiffness at large curvatures of less than 3.4% when using the simpler Neo-Hookean model.

3.4.7 Approximation: No Material Stiffening

Elastomers also exhibit a stiffening at large stretches, due to the molecules getting straightened. This is modeled by augmenting the strain energy function with an additional parameter. The Gent model [43] augments the strain energy function with a logarithmic term with the additional material parameter λ_{max} which is the stretch limit where the material exhibits unlimited stiffness:

$$\begin{aligned} W &= \frac{G}{2} \cdot J_1(\lambda_{max}) \cdot \ln\left(1 - \frac{J_1(\lambda_1)}{J_1(\lambda_{max})}\right) \cdot V_{sil} \\ &= \frac{G}{2} \cdot J_m \cdot \ln\left(1 - \frac{J_1}{J_m}\right) \cdot V_{sil} \end{aligned}$$

The rubber used for the PneuFlex actuator typically has $\lambda_{max} \approx 10$, which results in:$J_m \approx 100$ When computing the strain energy gradient using the Gent model, we get:

$$\begin{aligned} \frac{\delta W_{sil}^{Gent}}{\delta \lambda_1} &= C_1 \cdot J_m \cdot V_{sil} \cdot \frac{1}{1 - \frac{\lambda_1^2 + \lambda_1^{-2} - 2}{J_m}} \cdot \frac{2\lambda_1 - 2 \cdot \lambda_1^{-3}}{J_m} \\ &= \frac{1}{1 - \frac{\lambda_1^2 + \lambda_1^{-2} - 2}{J_m}} \cdot \frac{\delta W_{sil}}{\delta \lambda_1} \end{aligned} \tag{3.45}$$

For plausible values of $\lambda_1 < 3$ and $Jm = 100$, the error can be bounded to:

$$\frac{\delta W_{sil}^{Gent}}{\delta \lambda_1} < 1.077 \cdot \frac{\delta W_{sil}}{\delta \lambda_1}$$

Ignoring the material stiffening therefore underestimates stiffness at high curvatures for less than 7.7%.

3.5 Experimental Validation of the Scaling Laws

The model derived in this chapter can be used to dimension an actuators in a simple way by disregarding many nonlinear effects. For these design rules, we will validate the correct scaling behavior for the two main parameters of circumference c and hull thickness d. Additional validation experiments can be found in Section 5.2, which compare the model quantitatively against reference experiments with the help of simulation.

The first experiment tests, whether the rubber hull thickness d linearly determines actuation ratio, as it is predicted by Equation 3.32. The first experiment additionally tests whether the actuation ratio is indeed independent of actuator circumference c. The second experiment

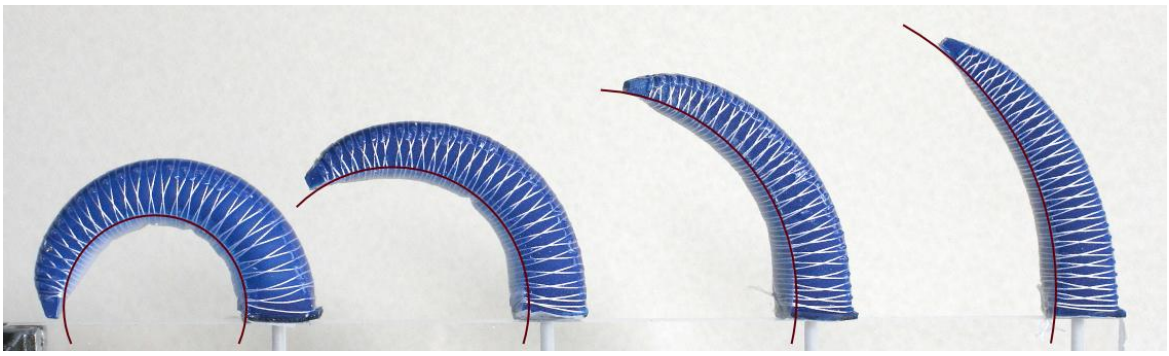

Fig. 3.11 Example of four fingers with different actuation ratios, inflated to 46.3 kPa. The overlaid circle segments indicate the constant curvature along the bottom layer. Figure published in Deimel and Brock [22] ©2016 Sage Publications.

focuses on the stiffness estimated by Equation 3.26, where we test whether stiffness scales with the third power of circumference.

3.5.1 Actuators with Constant Thickness and Varying Circumference

The model predicts that the actuation ratio is only dependent on hull thickness d and the shear modulus of the rubber. To test this, we built four actuators with the same shape, but with different d of 2.5 mm, 3.5 mm, 4.5 mm and 5.5 mm respectively. Circumference of the actuator increases from tip to base, while hull thickness stays constant. The resulting actuator should bend with uniform curvature, i.e. in a circle.

Fig. 3.11 shows the four actuators, all at the same pressure of 46.3 kPa. Despite the change in height, width and circumference, the curvatures of the bottom layers are constant along the actuators, as indicated by the circle segments. We can therefore validate the model's prediction that these shape parameters do not influence actuation ratio.

Fig. 3.12 shows data for the fingertip orientation of all four actuators with respect to air pressure. Fingertip orientation is used here as an measure of average curvature along the actuator. The curves for each actuator show the nonlinear behavior predicted by Eq. 3.31, i.e. an increase in actuation ratio towards higher curvatures. The dotted lines in Fig. 3.12 indicate the actuation ratio when scaling the measurements of the thinnest actuator (2.5 mm) to the thickness of the other actuators according to our design rule. Model and measurement agree well for 3.5 mm and 4.5 mm. At 5.5 mm it is clearly visible that the nonlinearity of the actuation ratio increases, making the actuator stiffer than expected at low pressures.

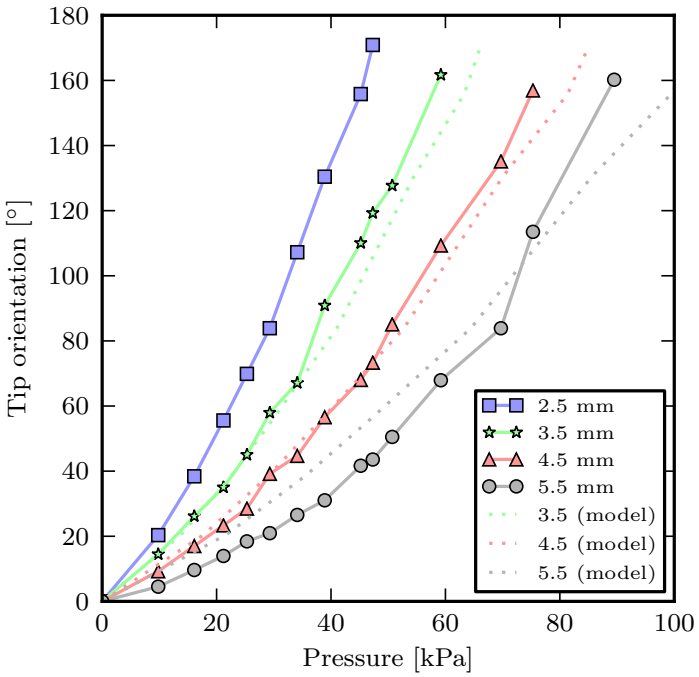

Fig. 3.12 Tip orientation versus inflation pressure for different rubber hull thicknesses. Dotted lines indicate model estimates based on the 2.5 mm measurement Figure published in Deimel and Brock [22] ©2016 Sage Publications.

3.5.2 Actuator with a Linear Stiffness Profile

Equations 3.26 and 3.33 predicts that stiffness increases with the third power of circumference. We can test this prediction with a simple "blocked tip" experiment. If the tip of the actuator is blocked and cannot move, then the resulting external load moments along the actuator will increase linearly with distance from the point contact. If the actuation ratio is constant (which was shown in the previous experiment) *and* the stiffness increases linearly with distance from the fingertip, then the moments will cancel out and the actuator will not bend at all, i.e. it will stay straight.

We therefore built an actuator with a constant actuation ratio (i.e. constant d) and a supposedly linear falling stiffness profile along the actuator. This is achieved by setting the circumference along the actuator to $c = c_0 \cdot \sqrt[3]{1 - \frac{x}{x_{\max}}}$ with c_0 the maximum circumference at the base and $x_{\max}$ the length of the actuator.

Figure 3.13 shows the deformations resulting from inflation at four different pressures while blocking the fingertip. Please note that in Figure 3.13d the finger would bend almost full circle when not being blocked. The curvatures along the actuator stay close to zero, which indicates a linear stiffness profile. Actuator stiffness therefore scales according to Equation 3.26. At the fingertip we can see a slight increase in curvature though. A subsequent analysis of the actuator geometry revealed, that due to an error in the mold creation the circumference close to the fingertip decreases slightly less fast than what a linearly falling

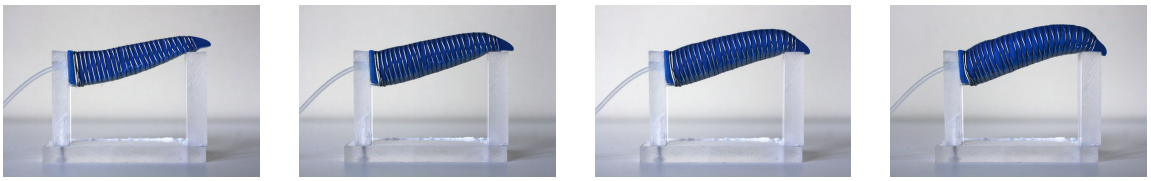

(a) 0 kPa (b) 17.3 kPa (c) 41.6 kPa (d) 80.1 kPa

Fig. 3.13 The finger is blocked by a fingertip contact while being inflated. An actuator with a linearly decreasing stiffness profile will show a constant curvature along the actuator under such load. Figure published in Deimel and Brock [22] ©2016 Sage Publications.

stiffness profile would require. This deviation explains the slight positive curvature exhibited by the actuator for the last 10 mm to 15 mm.

3.6 Best Practices for the Assembly of Soft Robots

A soft hand based on PneuFlex actuators will almost always be composed of many individual PneuFlex actuators. Therefore the aspect of how to scale, combine, assemble and connect PneuFlex actuators should not be underestimated in its importance to enable useful, reliable prototype designs. Such basic knowledge has not been widely disseminated yet and therefore warrants to be included here. This section lists a number of design methods that are of great help for reliably prototyping soft hands.

3.6.1 Rules of Thumb for PneuFlex Actuator Design

Although the previous section elaborated a very detailed mechanical model, we can condense the findings into a few simple rules of thumb, that can be used to avoid building actuators with poor performance or undesired properties. Using the shape variables as defined in Figure 3.9:

- Rule 1: Use $d \approx \frac{\delta p}{\delta \kappa} \cdot \frac{1}{8 \cdot G}$ to design the actuation ratio (Eq. 3.32)
- Rule 2: Use $c \ = 4 \cdot \sqrt[3]{\frac{\delta M_{load}}{\delta \kappa} \frac{1}{2 \cdot G \cdot d}}$ to design the stiffnesses (Eq. 3.26)
- Rule 3: Use $h \approx z$ if you want to avoid changes to shape (Sec. 3.4.3)
- Rule 4: Keep $d < 0.5 \cdot h$ to avoid rubber fatigue (Sec. 3.4.5)
- Rule 5: Use $S = (\lambda_{max} - 1) \cdot \sqrt[4]{G}$ to compare rubbers, higher is better (Sec. 3.3.3)

Please note that these rules of thumb are neither exact equations nor strict constraints. Depending on the desired actuator behavior, it may be perfectly sensible to violate them.

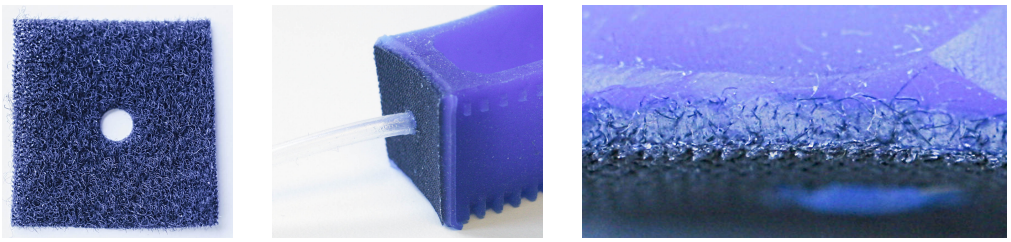

(a) Prepared piece of loop tape

(b) Example use in a PneuFlex actuator

(c) Cross cut of loop tape embedded in blue silicone

Fig. 3.14 The loop side of hook-and-loop fastener tape provides an excellent fabric for creating well anchored, flat, silicone-free surfaces to attach other materials to.

3.6.2 Interfacing Soft Rubber with Much Stiffer Materials

A very important but mostly neglected topic is the interface of soft continuum actuators with much stiffer structures and materials. The big issue here is that at the interface, elasticity changes abruptly by several orders of magnitude. This leads to stress concentrations and huge local strains close to the interface, reducing overall strength of the connection. For a reliable and strong connection, such an abrupt change in elasticity should best be avoided. To aggravate the problem, silicone rubbers have poor adhesion properties to anything else but silicone in the first place. A good connection needs to solve both problems.

For attaching PneuFlex actuators, we developed a simple but very effective method that solves these issues. Instead of bonding rubber directly onto a hard surface, using bolts [35] or clamps [21] we use fibers to mediate forces. We first embed a large number of very small fibers that create anchors within the rubber. The reason we want as small fibers as possible is explained in Section 3.3.2. The fibers themselves are attached to a sheet, which in turn provides a non-silicone surface to bond to non-silicone materials. Fortunately, such a complex fabric is conveniently mass-produced for hook-and-loop fastener tape. The loop fabric, which is shown in Figure 3.14a, provides a smooth surface on one side, and a large number of tiny fiber loops on the other side.

To create an interface, the loop tape is first cut into shape, and then embedded in silicone. Silicone residue on the flat side can easily be peeled off to expose a clean surface. For PneuFlex actuators, the embedding can be done while casting the top part by placing the loop tape on the opening of the mold. Alternatively, the loop tape can first be coated with silicone separately, and then bonded to with silicone adhesive.

The result is shown in Figure 3.14b. The exposed polyamide surface can easily and quickly be bonded with high strength to a large range of materials, e.g. using cyanoacrylate adhesive (super glue). Figure 3.14c shows a closeup of the interface. The fiber loops only extend into

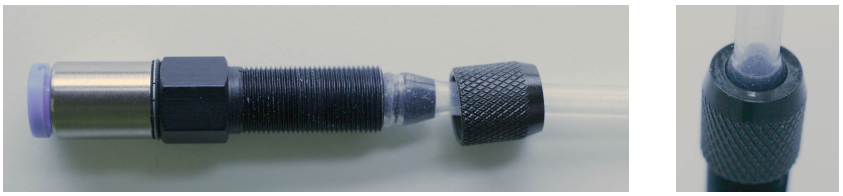

(a) (b)

Fig. 3.15 Fittings with spigot nuts help avoids air leakage at higher pressures.

the rubber for about 1 mm, but this is enough to make the fabric completely inseparable from the rubber.

3.6.3 Interfacing Silicone Tubes With Regular Pneumatic Tubes

Another small detail that nevertheless often creates problems for fluidic soft continuum actuators is the tubing. For PneuFlex actuators, the most reliable method is to use pre-manufactured silicone rubber tubes that are inserted after casting, but before the air chamber is closed. The tube is bonded and sealed with high-quality silicone adhesive. The tube size is selected to provide unrestricted airflow while being able to maintain the air supply pressure, while staying lightweight and flexible. For actuators of soft hands, tubes with 2 mm inner diameter and 5 mm outer diameter have proven to be a good compromise.

For longer distances, and to connect actuators to industrial pneumatics components, we often desire to connect silicone tubes to standard 4 mm pneumatic tubes. For low pressures, rubber tubes can simply be put over the PU tubes. For higher pressures though, this method is prone to leakage. In this cases, we use fittings with a spigot nut on one side, and 4 mm IQS plugs on the other. At higher pressures, i.e. beyond 100 kPa, the spigot nut keeps the tube from expanding and this way prevents air leakage.

3.7 Summary

This chapter provided a comprehensive treatment of the aspects necessary to design PneuFlex actuators according to desired properties, build them, and assemble them into complete soft hands. We provided a concise set of design rules to ensure robust actuators and to predict mechanical behavior, and a comprehensive analysis of material and design choices. We further validated our approximative mechanical model with several experiments that show scaling behavior predicted by the model.

Chapter 4

Compliance-Aware Control of Pneumatic Actuators

This chapter explains the advantage of equilibrium-point control (control in the null-space of compliant actuators) over force or position control of soft actuators. It further demonstrates an implementation of a continuous, fast and stable equilibrium-point control for pneumatic soft hands based on the control of the flow of air mass.

4.1 Control Methods for PneuFlex Actuators

In order to control pneumatic soft robots, several different strategies have been employed in recent years. Published approaches can loosely be classified into four categories: time-based control [21, 23], pressure-based control [87], volume-based control and *equilibrium-point* control. The former three are well established control modes in pneumatic control, while the latter control mode is special to soft actuators.

Time-Based Control In time-based control schemes, airflow is simply controlled by predefined or precomputed inflation or deflation periods. This is the simplest type of control scheme, but it is sensitive to changes and variations in the control system and the air supply. Nevertheless, this control scheme is often used in basic systems as it is simple to implement and does not require any sensors.

Pressure/Force-Based Control In this control scheme, the pressure within the actuator (or in the tube connecting the actuator) is measured and controlled in a closed loop. As air pressure changes instantaneously translate into actuation forces, this can also be considered a variant of force control. Recent examples are the use of commercial pressure regulators [41], a pulse-width-modulation based pressure control [78] and as the inner loop of a more elaborate control setup [70].

While force control is the method of choice for electromagnetic actuators (due to superior control bandwidth), for pneumatic systems it is often not. Control is usually done with discrete valves and not proportional valves due to costs, while pressure control desires the ability for minute changes in pressure. Therefore these types of control often suffer from either "valve chatter", or from unreasonably large pressure hystereses. Commercial pressure regulators are available, but are engineered towards large volumetric flows (usually more than 100 slpm (standard liter per minute), about 10 to 100 times more than needed), making them perform poorly on typical soft robot systems.

A second drawback are the large time delays and the time constants inherent to physically moving pistons and equilibrating air pressure within tubes, which in itself severely restricts the achievable bandwidth of a continuous pressure control loop.

Volume/Position-Based Control In this control scheme, the volume of the actuator is measured and controlled in a closed loop. As volume of a pneumatic soft continuum actuator directly relates to actuator curvature (see Section 3.4), this effectively is equivalent to position control. In some systems, curvature sensors are added to control (free-space) motion in a closed loop [78].

Although popular in classical pneumatics, this control mode does not have the same importance for soft robotics. Soft actuators intentionally are compliant to deviations in position, and this directly conflicts with the primary goal of position-based control: accurate positioning.

In the cases where position control is used nevertheless [70, 87], this contradiction is resolved by low control bandwidth: mechanical compliance provides low impedance at high frequencies, while position control provides high impedance at low frequencies.

4.2 Equilibrium-Point Control

Both pressure/force-based control and volume/position-based control inherently neglect the prime advantage of soft actuators, being compliant. Therefore I propose a third option for controlling compliant actuators. The mechanical compliance of soft actuators towards external disturbance creates motion only in a subspace of the position-force space. This creates a corresponding null space in which we can do control without being influenced by the compliant motion intrinsic to a soft actuator. Such a decomposition is illustrated in Figure 4.1 with violet curves (compliant motion subspace) and green curves (controllable null space) in the force-position space. The actuators state is determined by the deflection along the compliant motion curves (violet) and the position along the green curves. The former is caused by external interaction forces, while the latter is caused by a suitable system variable under control of the robot. Position along the null-space direction can be described intuitively by specifying the position at zero interaction force, i.e. the position the actuator assumes in free motion. This actuator state is known under different names, e.g. free-space position, equilibrium point, prescriptive motion, or soft synergy. Here, I adopt the term *equilibrium point* over the other terms to emphasize that position is not the key property, but the implicit specification of the subspace of compliant motion.

To summarize, equilibrium-point control targets a variable that is independent of the compliant motion of the soft actuator. This definition also captures its main advantage over position or force control: External disturbances (i.e. contact forces and deformation) do not change the equilibrium point, hence the control strategy is amenable to open-loop control. The main perceived drawback of equilibrium-point control is, that it gives up direct control over position and force. But here we need to realize, that we specifically want to use the actuator's compliance, thus we neither need to control position nor force. In the understanding of Soft Manipulation, this is a highly desirable feature, not a bug. Another problem surfaces when considering the interface to planning. Planning is done predominantly in spatial representations, and equilibrium-point control does not offer a direct mapping into

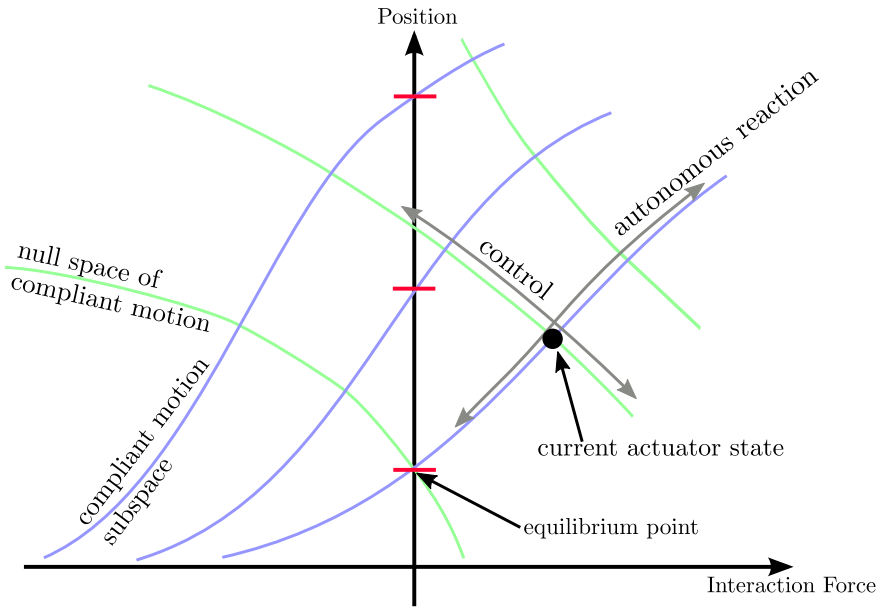

Fig. 4.1 Illustration of equilibrium-point control in the force-position space. Violet isolines indicate subspace along which actuator state can shift autonomously of control due to mechanical compliance. Control operates in the corresponding nullspace. The position assumed with zero interaction force (point of equilibrium) is used as a reference to parameterize actuation orthogonal to the compliant motion inherent in the actuator (violet isolines).

such a space. To do e.g. motion planning, algorithms that are not based on euclidean space and mechanics would need to be developed.

From the perspective of control, the equilibrium-point control scheme promises superior performance in terms of control bandwidth and as a well factorized counterpart of soft actuators. While equilibrium-point control is a general concept applicable to any actuator technology, in the next section we will look specifically at how to implement it for soft pneumatic actuators.

Equilibrium-Point Control with Discrete Valves As already outlined in the previous section, the purpose and distinguishing feature of Equilibrium Point control is to provide control in the null space of an actuator's compliant motion. For pneumatic soft continuum actuators, the ideal gas law gives us an indication of possible control variables we can consider:

$$p \cdot V = k \cdot T \cdot m$$

Both variables on the left hand side, pressure and volume, change upon compliant motion of a PneuFlex actuator. On the right hand side we find the Boltzmann constant, temperature

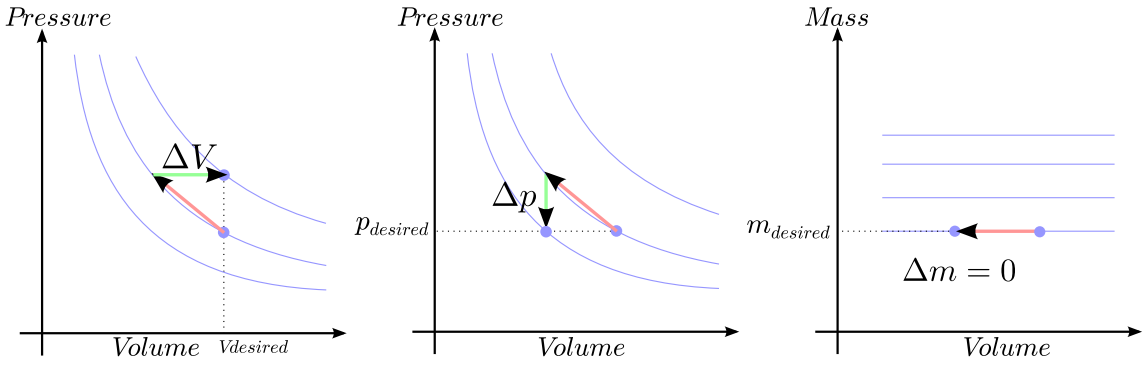

(a) Volume control (b) Pressure control (c) Mass control

Fig. 4.2 Illustration of the key advantage of targeting air mass contained in an actuator as the principal control variable. The violet isolines indicate system behavior when valves are closed. Upon external disturbance (causing shift along the isolines), position and pressure control both require inflation or deflation, while air mass is unaffected.

and air mass. Changing air temperature is difficult to accomplish in a fast and well defined manner, although there are devices that exploit adiabatic expansion by combusting flammable gas mixtures [113]. The by far most interesting variable though is the enclosed air mass m, as it can only change when we take action, i.e. open the inlet or outlet valve. Figure 4.2 reiterates the principal advantage of air mass over pressure and volume. States reachable by compliant deformation only (i.e. closed valves) are indicated with violet isolines (same as in Figure 4.1). When the actuator compliantly deforms due to a change in external forces (indicated by the red arrow), it changes both volume and pressure. That means a corrective action is necessary for both pressure and volume control (Figure 4.1a and 4.1b). When we consider air mass as control variable though, we find that the violet isolines in Figure 4.1c are horizontal – there is no need for corrective action by control. As the air within the actuator is perfectly enclosed when valves are closed, air mass obviously does not change. Indeed, this is exactly what we are looking for: a target variable that is independent of the compliant deformation, but also determines the equilibrium point.

So far, we haven't considered changes in temperature of the enclosed air yet. For small actuators such as those used for soft hands, any strong temperature gradient between enclosed air and environment will quickly equilibrate and we can assume that temperature is controlled by the environment. The temperature of the environment will be constant for the most common application scenarios, so we will assume T to be constant (isothermal compression, not adiabatic). I.e., we assume the term kT to be constant.

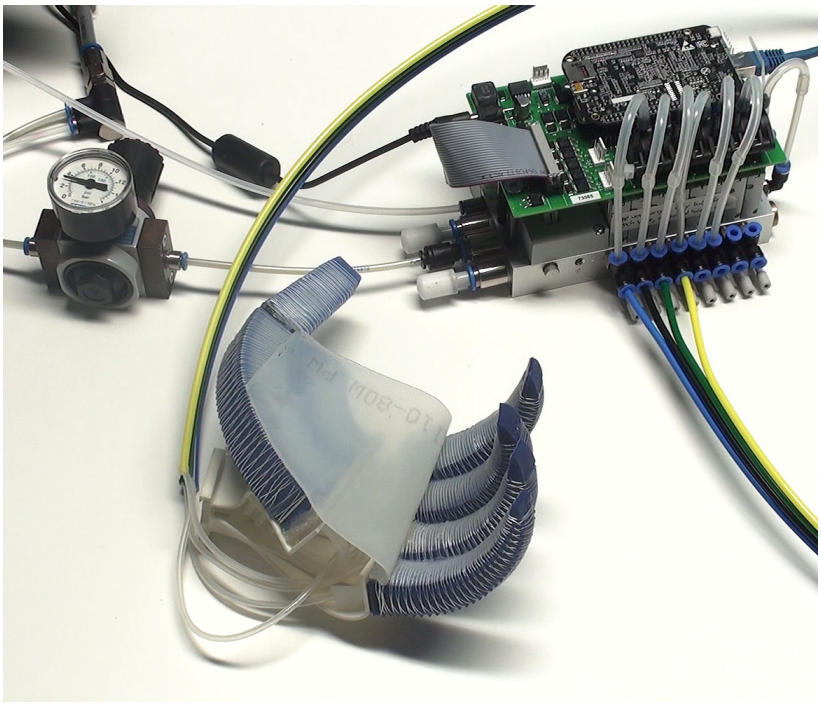

Fig. 4.3 Pneumaticbox control system (top right) with RBO Hand 2.

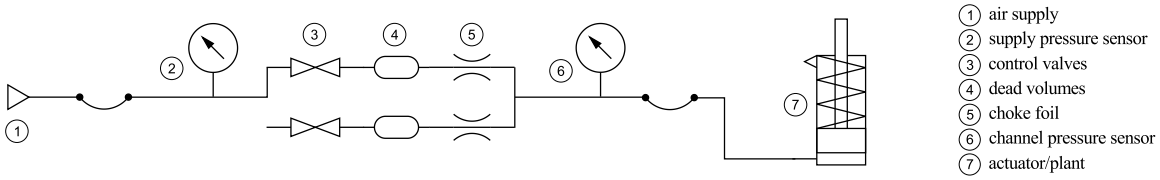

Fig. 4.4 Schematic flow path of one of 16 channels of the Pneumaticbox. Figure published in Deimel, Radke, and Brock [25] ©2016 IEEE

4.3 The Pneumaticbox Real Time Pneumatic Control System

Before we continue to investigate how to implement an equilibrium point control scheme based on air mass control, we take a detailed look at the used control platform. The Pneumaticbox, shown in Figure 4.3, is a pneumatic control systems designed for the control of pneumatic soft hands. The main hardware components are listed in Table 4.1. The Pneumaticbox provides up to eight independently controllable channels. The components of each control channel are illustrated in Figure 4.4. The main components are two discrete valves for inflation and deflation and two pressure sensors for reading channel air pressure and supply pressure. The supply pressure sensor is shared with all channels. All pressure sensors and valves are directly connected via analog and digital I/O to an embedded computer

Component	Description
Valves	Valve array with eight FESTO VTUG series 5/3 pilot valves (20 ms to 40 ms delay)
Pressure sensors	6x Freescale MPX4250 (0-250kPa, 1.4% accuracy) and 1x Freescale MPX5700 (0-700kPa,2.5% accuracy)
Embedded computer	BeagleBone Black rev.C
I/O PCB	custom, contains 16 valve drivers, 7 pressure sensors, 1 compressor driver, I2C bus, SPI bus, 12-24V supply voltage

Table 4.1 Major components of the Pneumaticbox

(BeagleBone Black) running Ubuntu OS. This choice of software provides a very well supported platform which greatly simplifies integration of the Pneumaticbox in existing robot systems such as those based on the ROS middle ware. Real-Time Control is implemented as a high-priority process. This process provides a network-transparent API to configure, run and stop multiple concurrent controllers at 500 Hz, and to monitor signals generated by hardware or control. A reference Python client library provides an easy way of quickly setting up configuration and for remote control without requiring real-time capability on the client side. If necessary though, it also supports sub-millisecond accurate synchronization of signals by scheduling signal events ahead of time, relying on synchronized system times across client and server.

Different control schemes are possible with the Pneumaticbox. In the simplest setup, the client implements a time-based control and directly schedules changes between inflating, deflating, and being detached for each controlled channel. For implementing air mass control, this system was extended with two more controllers which provide control of air mass and control of mass flow respectively. Their design and operation is explained in the following subsection.

Choking of Industrial Valve Arrays The industrial valves used for the Pneumaticbox provide an air flow of about 50 slpm to 200 slpm (standard liter per minute) which means a soft hand can be fully inflated in 250 ms. On the other hand, the valves are relatively slow, and take 20 ms to 40 ms to open or close. This also means that the smallest commandable pulse is about 40 ms long. To allow for a fine-grained control of hand posture, we introduced chokes in the flow path of the industrial pilot valves to reduce the volumetric flow. Additionally, the chokes enable us to adjust flow rates between individual valves while still using only one single valve type. Decoupling choice of flow rate from valve properties greatly simplifies parts sourcing and repurposing for new applications. This was done by placing a perforated plastic foil between the valves and their socket. An example of such a *choke foil* is shown

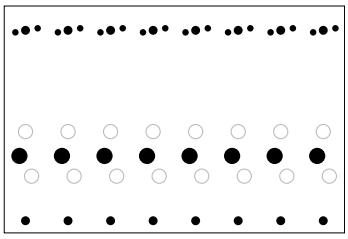

(a) Stencil, gray circles indicate supply and exhaust line ports.

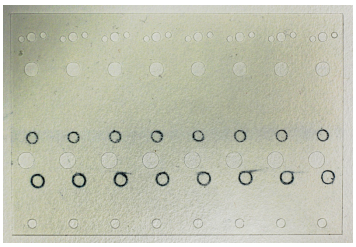

(b) Pre-Cut Blind, areas marked for piercing

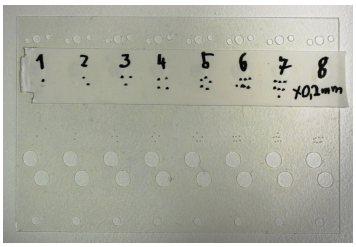

(c) Perforated choke foil with various numbers of 0.2 mm inlet holes and with 4 mm outlet holes

Fig. 4.5 Steps in the creation of a choke foil.

in Figure 4.5. The placement of the choke reduces the dead volume between the valve's orifice and the choke's orifice to 0.15 cm^3. This is important for control, as the dead volume too determines the minimal amount of air that is moved during a pulse. For comparison, an external choke, i.e. one attached to the quick-connect plugs, would create a dead volume of about 1.2 cm^3. The choke foil is made from a 0.1 mm thick PET foil, which is pre-cut using a desktop cutting plotter (Silhouette Portrait). The inlet and outlet holes are pierced afterwards, using needles of different sizes. The steps are shown in Figure 4.5. The choke foil allows us to adjust the nominal air flow by two orders of magnitude. In the experiments of this chapter, the choke foil was configured to an 0.2 mm hole along the inflation path and a 0.6 mm hole along the deflation path of each channel, to balance the mass flow strength between inflation and deflation.

4.4 Air Mass Control on the Pneumaticbox

Unfortunately, there are no commercial systems available that are capable of directly controlling air mass and that fit to the volume and flow requirements of soft hands. While there are fast mass-flow sensors on the market, they are relatively expensive and would increase the hardware cost per channels by a factor of 2 to 4. Therefore we investigate control of air mass by using pressure sensors. These sensors are relatively cheap and provide fast and accurate measurements. These sensors are also multipurpose and can be used for other control schemes and monitoring already. Because of this, it is highly interesting to develop a mass control based on pressure sensing. The core of the controller is an observer model which estimates the mass change within the next time step from the available pressure values and valve state

The basic idea to estimate the mass flow is to use the valves themselves as a defined resistance to air flow, and use the pressure drop along their flow path to compute the instant mass flow. The estimated total air mass is then used by a simple bang-bang controller to decide when to open or close the valves. The controller opens a valve when the error between current estimated and desired mass exceeds a threshold. Depending on the sign, the inflation or the deflation valve is opened. Once a valve is open, the controller continuously compares the estimate with the current desired air mass and closes the valve when the error changes sign. The controller obtains a mass estimate essentially through the summation of estimated mass changes of consecutive pulses. As a result, the controller is subject to drift as estimation errors accumulate. It is therefore paramount for reliable control to estimate the mass delta as accurately as possible across many different pulse lengths and pressure ranges.

4.4.1 Delta-Mass Observer Model

We want to design an air mass change observer for the pneumatic system illustrated in Figure 4.4. The available information is the supply pressure p_{supply}, the ambient pressure p_{ambient}, channel pressure p_{channel}, and the current and previous valve state. As inflation and deflation flow path are distinct, we require two flow path models. Additionally, the flow direction reverses, which also flips the semantics of the pressure sensors. For convenience, we therefore map the pressure signals to a representation applicable to both inflation and deflation:

name	during inflation	during deflation
p_{in}	p_{supply}	$p_{channel}$
p_{out}	$p_{channel}$	$p_{ambient}$
t_{on}	$t_{on}(\textit{inflate valve})$	$t_{on}(\textit{deflate valve})$

In the following model, all pressures are in absolute terms, e.g. $p_{ambient}$ is usually assumed to be 101.3 kPa.

The flow path between the pressure sensors in Figure 4.4 is quite complex, dependent on the exact hardware, but also varies between identical Pneumaticboxes. We therefore require both a model that captures the main contributors to pressure drop, and a straightforward calibration procedure to estimate the model parameters. While it is enticing to follow a black-box approach, e.g. using neural networks as function approximators, the resulting large number of parameters requires a lot of training data, making the calibration procedure tedious. Therefore, we investigate a white-box approach and create a model that covers the main probable contributors to pressure drops along the flow path: the viscous friction along the walls, and the dynamic pressure drop at the valve's orifice or choke. In addition to these

continuous effects, we know that delays in valve switching will also add or remove a discrete amount of air with each pulse. Finally, we may also have a small cavity between the valve orifice and the choke (item 4 in Figure 4.4). In most pneumatic controls the valve's orifice takes the role of the choke and so there is no cavity, but in the case of the Pneumaticbox, these functions are physically separated. Because of this, the cavity will pressurize instantly upon opening. After closing the related air mass will discharge into the channel no matter what. In order to capture all these phenomena, we constructed a model based on a linear combination of terms:

$$\begin{aligned}
\Delta m(\Delta t) = \quad & c_0 && \text{Bias} \\
& + c_1 \cdot \int_{t_{on}}^{t_{on}+\Delta t} (p_{in}(t) - p_{out}(t))dt && \text{Friction} \\
& + c_2 \cdot \int_{t_{on}}^{t_{on}+\Delta t} p_{in}(t) \cdot \Psi(p_{in}(t), p_{out}(t))dt && \text{Injector} \\
& + c_3 \cdot p_{in}(t_{on}) + c_4 \cdot p_{out}(t_{on}) && \text{Switching} \qquad (4.1)
\end{aligned}$$

where Δt denotes the hitherto duration of an ongoing pulse, starting from electrically switching on the valve. $\Delta m(\Delta t)$ denotes the change of mass that we would obtain for the pulse if we were to immediately switch off the valve electrically. The *friction* term models the influence of viscous friction along the inner walls of the flow path. The *injector* term models the influence of the choke, and the *switching* term models discrete effects that happen during switch-on and switch-off. The latter takes into account the pressure before and after the valve, as most effects (such as the dead volume) scale with pressure. The *bias* term captures any absolute errors that may be introduced by the other terms. The model is chosen so that parameters $c_0, \ldots, c_4$ can be determined via linear regression, in order to make calibration simple. Ideally though, the friction and injector terms would need to be combined as both effects rather serial in the flow path and therefore additive in flow resistance, not flow conductance. For the sake of simplicity though, this error in modeling is accepted.

Injector term The injector term warrants additional explanation. The function Ψ is a model of nonlinearity for the flow through small orifices and chokes, and is well known in fluid dynamics [86]:

$$\psi = \begin{cases} \sqrt{\frac{\kappa}{\kappa-1} \cdot \left[\left(\frac{p_{out}}{p_{in}}^{\frac{2}{\kappa}} \right) - \left(\frac{p_{out}}{p_{in}}^{\frac{\kappa+1}{\kappa}} \right) \right]} & \text{at subsonic flow} \\ 0.484 & \text{at sonic flow} \end{cases}$$

κ is the ratio of isobaric to isochoric heat capacity of the gas. For dry air, $\kappa = 1.4$. Below a certain pressure ratio, the air flow is subsonic and increases with $\frac{p_{out}}{p_{in}}$. Above that level the flow within the orifice becomes sonic, mass flow becomes independent of p_{out}, and Ψ becomes a constant. The change from subsonic to sonic airflow happens at the critical pressure ratio β_{cr}:

$$\beta_{cr} = \left(\frac{\kappa+1}{2}\right)^{\frac{\kappa}{\kappa-1}} = 1.894$$

For dry air at room temperature the function becomes:

$$\psi = \begin{cases} \sqrt{7.0 \cdot \left[\left(\frac{p_{\text{out}}}{p_{\text{in}}}\right)^{1.429} - \left(\frac{p_{\text{out}}}{p_{\text{in}}}\right)^{1.714}\right]}, & \text{if } \frac{p_{in}}{p_{out}} < 1.894 \\ 0.484, & \text{otherwise} \end{cases}$$

To numerically simplify the computation of Ψ, we use an approximation published by The Lee Company[1]:

$$\psi \approx \begin{cases} \sqrt{\frac{p_{in}-p_{out}}{p_{in}} \cdot \frac{p_{out}}{p_{in}}}, & \text{if } \frac{p_{out}}{p_{in}} < \frac{1}{1.894} \\ 0.5, & \text{otherwise} \end{cases}$$

In the evaluation experiments, the error (RSME) between textbook model and approximation amounted to 1.4%.

4.4.2 Calibration Procedure

The main goal of the calibration procedure is to provide a simple to execute protocol which also does not require an excessive amount of time. We devised a mostly automated calibration procedure which requires the user to only intervene a few times to vary the supply pressure, as this variable can not be changed autonomously by the Pneumaticbox. In the first phase of the calibration, a sequence of test pulses is generated and the effect on a known, fixed channel volume is recorded. The calibration takes about 10 min to 30 min per channel and about 400 to 1600 data points are sampled. In the second phase, we do a linear regression to fit the delta-mass observer model parameters to the recorded data. The data acquisition algorithm is shown in Algorithm 1. In order to cover a large range of prior channel pressures, we skew the ratio of inflation to deflation period, reversing the skew when we exit the desired

[1] http://www.theleeco.com/engineering/gases/calculate-flow-resistance-gases.cfm

pressure range. This creates a see-saw pattern and ensures that we collect data from the complete range. In order to work correctly, we also need to estimate the ratio between deflation and inflation speed in order to balance the upwards and downwards slope of the see-saw pattern. This ratio can also be computed adaptively during sampling, by computing the ratio between the number of deflation to inflation pulses. Providing a reasonable estimate from the start prevents unbalanced data sets, though. While test pulses are applied, the values of the nonlinear functions are computed online:

$$f_{friciton}(\Delta t) = \int_{t_{on}}^{t_{on}+\Delta t} (p_{in}(t) - p_{out}(t))dt$$
$$f_{injector}(\Delta t) = \int_{t_{on}}^{t_{on}+\Delta t} p_{in}(t) \cdot \Psi(p_{in}(t), p_{out}(t))dt$$

For automated ground truth acquisition, we estimate the change in air mass post-hoc. After the pulse was applied, the difference in pressure before and after the pulse is computed and multiplied by the fixed channel Volume. During the calibration, the user is asked several times to alter the supply pressure – which usually is not under control of the control system – to collect data at different pressure levels. The supply pressures should cover the range of pressure expected during normal operation, but do not need to be set to precise levels. When enough data points are gathered, a linear regression is performed on the acquired data to estimate the model coefficients $c_0 ... c_3$, both for inflation and deflation separately. The detailed steps are outlined in Algorithm 1.

In actual operation, a mass controller can be expected to generate short pulses more often than long ones. To improve accuracy especially on short duration pulses, we used an exponential distribution to sample pulse durations. This gives short duration pulses a larger weight in the linear regression.

4.4.3 Results

We compared the presented mass change observer with a naive baseline model, which assumes that mass flow grows linearly with pressure:

$$m(\Delta t) = \begin{cases} c_{inflate} \cdot p_{supply}(t_{on}) \cdot \Delta t, & \text{when inflating} \\ c_{deflate} \cdot p_{channel}(t_{on}) \cdot \Delta t, & \text{when deflating} \end{cases}$$

Algorithm 1 Calibration Procedure

Let $V_{channel}$ be the fixed volume attached to the channel under test
Let p_{min} be the minimum channel pressure to test at
Let p_{max} be the maximum channel pressure to test at
Let t_{min} be shortest tested pulse period
Let t_{max} be longest tested pulse period
Let $p_{ambient}$ be the ambient air pressure
Let $n_{supply\ pressures}$ be the number of supply pressure levels to test at
Let $\frac{\text{deflation speed}}{\text{inflation speed}}$ be a rough estimate of the ratio of mass flow of deflation vs. inflation
$skew\ factor \leftarrow 2.0$
procedure DATA ACQUISITION($p_{min}, p_{max}, t_{min}, t_{max}, n_{samples}, n_{supply\ pressures}, skew\ factor$)
    $n_{user\ interaction} \leftarrow \frac{n_{samples}}{n_{supply\ pressures}}$
    $skew \leftarrow \sqrt{skew\ factor}$
    for i in $[1 \ldots n_{samples}]$ **do**
        if $p_{channel} < p_{min}$ **then** $skew \leftarrow \sqrt{skew\ factor}$
        else if $p_{channel} > p_{max}$ **then** $skew \leftarrow \sqrt{\frac{1}{skew\ factor}}$
        end if
        if $i \mod n_{interaction} = 0$ **then**
            Request variation of supply pressure
        end if
        $t \leftarrow$ RANDOMEXPONENTIAL($t_{min}, t_{max}, \lambda = 1$)
        $t_{inflation} \leftarrow t \cdot skew$
        $t_{deflation} \leftarrow t \cdot \frac{1}{skew} \cdot \frac{deflation\ speed}{inflation\ speed}$

        Measure $p_{channel}, p_{supply}$
        INFLATE($t_{inflation}$)
        Record $f_{injector}$ and $f_{friction}$ values.
        Measure $\Delta p_{channel}$
        Compute ground truth $\Delta m_{inflation} = \frac{\Delta p_{channel} \cdot V_{channel}}{k \cdot T}$

        Measure $p_{channel}, p_{supply}$
        DEFLATE($t_{deflation}$)
        Record $f_{injector}$ and $f_{friction}$ values.
        Measure $\Delta p_{channel}$
        Compute ground truth $\Delta m_{deflation} = \frac{\Delta p_{channel} \cdot V_{channel}}{k \cdot T}$
    end for
end procedure
procedure CALIBRATION($f_{injector}, f_{friction}, p_{supply}, p_{channel}, \Delta m_{inflation}, \Delta m_{deflation}$)
    $[c_0, c_1, c_2, c_3]_{inf} \leftarrow$ LINEARREGRESSION($[1, f_{injector}, f_{friction}, p_{supply}, p_{channel}], \Delta m_{inflation}$)
    $[c_0, c_1, c_2, c_3]_{def} \leftarrow$ LINEARREGRESSION($[1, f_{injector}, f_{friction}, p_{channel}, p_{ambient}], \Delta m_{deflation}$)
end procedure

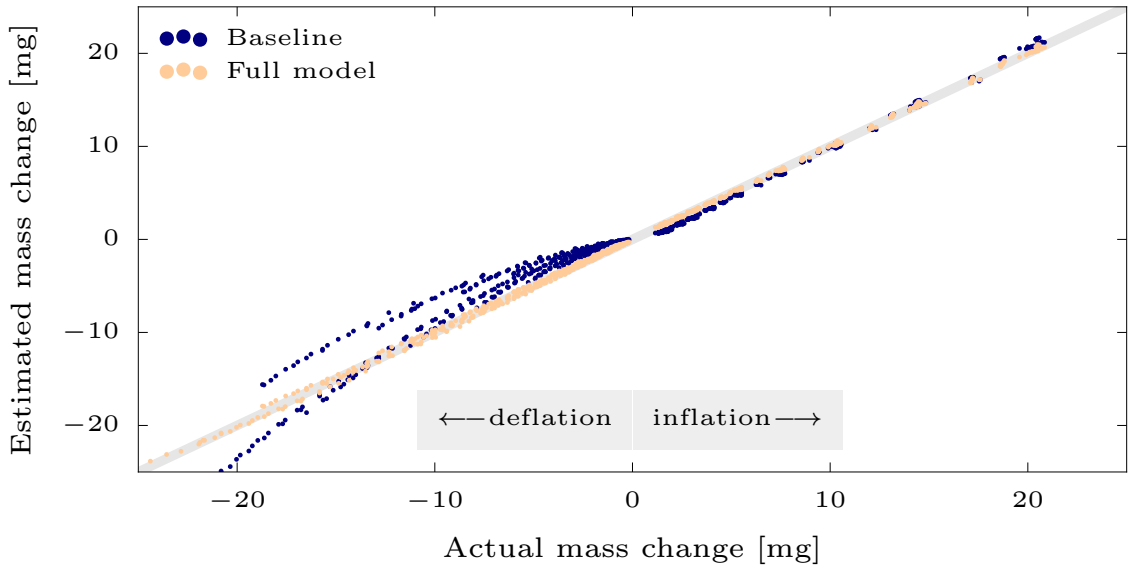

(a) Scatter plot of estimation accuracy against ground truth

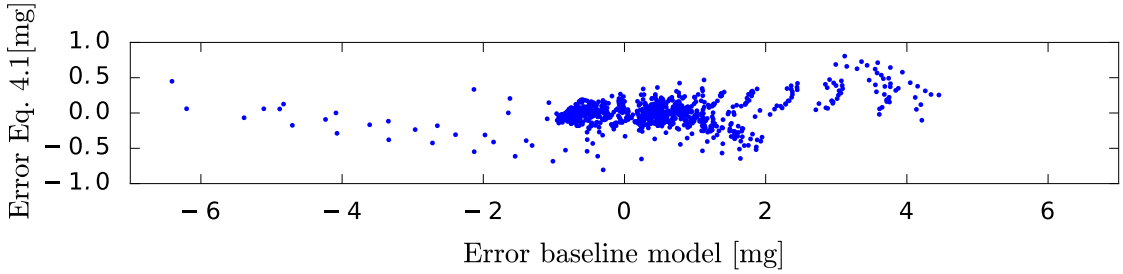

(b) Scatter plot of estimation errors between naive and calibrated model, which reduces error about seven-fold

Fig. 4.6 Results of estimating the mass change of single pulses for the calibrated mass observer versus a naive baseline model. The full model improves the mass estimate especially for deflation pulses, but also inflated masses are estimated more accurately. Figure published in Deimel, Radke, and Brock [25] ©2016 IEEE

This model was used in previous work [21, 22] for control. The model assumes mass flow to be constant during inflation and to only depend on the presumably constant inlet pressure. These assumptions make it possible to precompute the required pulse duration and execute them using time-based control. Figure 4.6a shows a direct comparison between the precomputed baseline and the mass-change-observer model, relative to the ground truth. Ground truth was acquired by multiplying the difference in pressure before and after the pulse with the attached reference volume (a 0.5 L PET bottle), assuming dry air and constant temperature (20 °C). The gray line indicates a perfect mass observer. For inflation, it turns out that the precomputed estimates are almost as good as the estimates of the mass-change

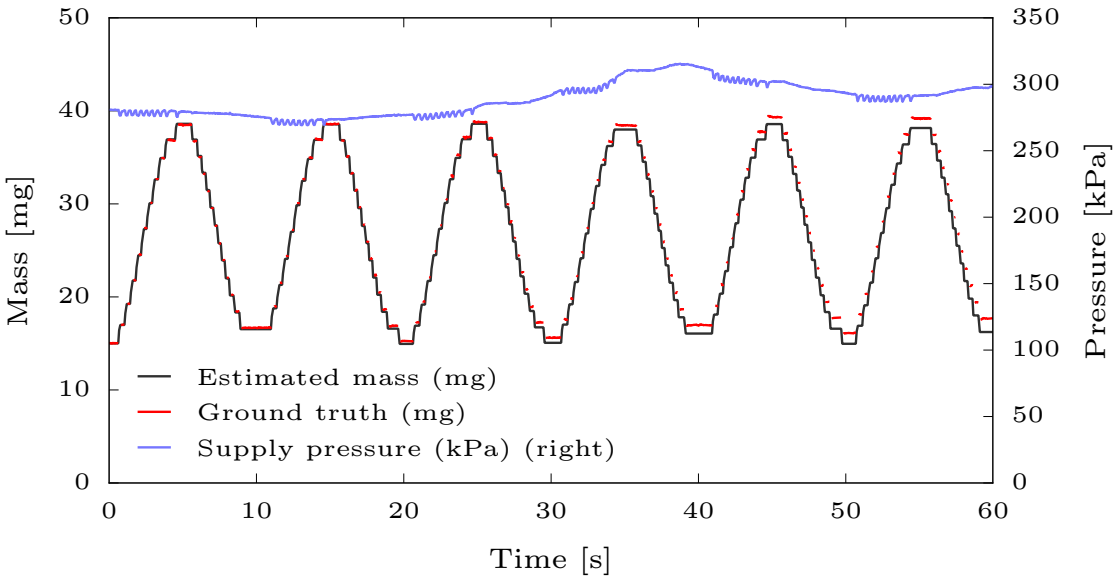

Fig. 4.7 Experiment illustrating the capability of the mass controller to account for and compensate changes in supply pressure. Supply pressure was changed manually with a regulator to simulate variations that can be caused by other consumers, exhausting a small air reservoir, or intermittent compressor activity.

observer. For deflation though, the calibrated model clearly outperforms. For completeness, Figure 4.6b shows the absolute error for both models. The error bound of the calibrated model is 7 times narrower than the baseline.

Baseline Model Performance The baseline model performs surprisingly well for inflation pulses. The reason probably is the large pressure difference between air supply and actuated channel. This results in a sonic flow within the choke, which is only dependent on the supply pressure. Such a large pressure difference is easy to obtain for inflation, although this is not very energy efficient. For deflation, it requires a very low ambient pressure (below $0.4bar$), effectively requiring an additional vacuum pump. This would drive up system costs and build volume considerably.

Rejection of Supply pressure changes While for stationary systems it is common to employ a line regulator, mobile systems would benefit from not requiring a stable pressure supply. Avoiding the necessary pressure drop to stabilize air supply improves energetic efficiency too. It also reduces the number of necessary components. But even for stationary systems, being able to not care about an accurate supply pressure is desirable as it avoids user errors and improves the reproducibility of control patterns. Figure 4.7 shows a test where mass control is used to effect a sinusoidal motion while the pressure regulator is adjusted

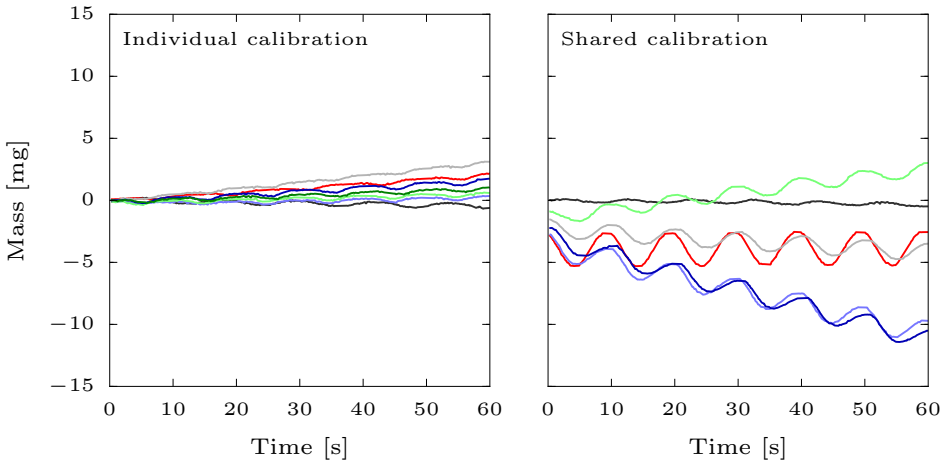

(a) Individually calibrated

(b) One channel calibrated, calibration shared with other channels

Fig. 4.8 Tracking error of six individual channels using the sine pattern shown in Fig 4.9. Figures published in Deimel, Radke, and Brock [25] ©2016 IEEE

manually. Ground truth is obtained by measuring the pressure in between pulses and by using a fixed volume attached to the channel. The relative variation in supply pressure is about 25%, but shows no discernible effects on the controlled air mass. Please note that the data also show a a small drift in the mass estimate. This effect is independent of the pressure variation.

Accuracy To estimate the attainable accuracy of a calibrated mass controller, we calibrated five individual valves and evaluated their ability to track a sinusoidal mass trajectory for 60 s. The training set for each calibration was reduced to 100 data points, and only supply pressures of 260 kPa and 320 kPa were sampled to simulate an adverse case. The resulting error is shown in Figure 4.8a. After a total duration of 60 s, the error of all but one valve stays below 2.5 mg which is the smallest possible mass change the valves can command. In addition to testing the properly calibrated channels, we also investigated if channels really need to be calibrated individually, or if the calibration can be shared by many channels. Figure 4.8b shows the evaluation when sharing the calibration of one channel. Mass control exhibits a considerably larger error, and the average error increases about four times. This clearly indicates that each channel – and each control system – should be calibrated individually to avoid drift.

Finally, Figures 4.9 and 4.10 demonstrate the performance attainable with a well calibrated system, using 1600 samples per channel. The mass controller is able to enact arbitrary air mass trajectories for an extended period without accumulating excessive drift.

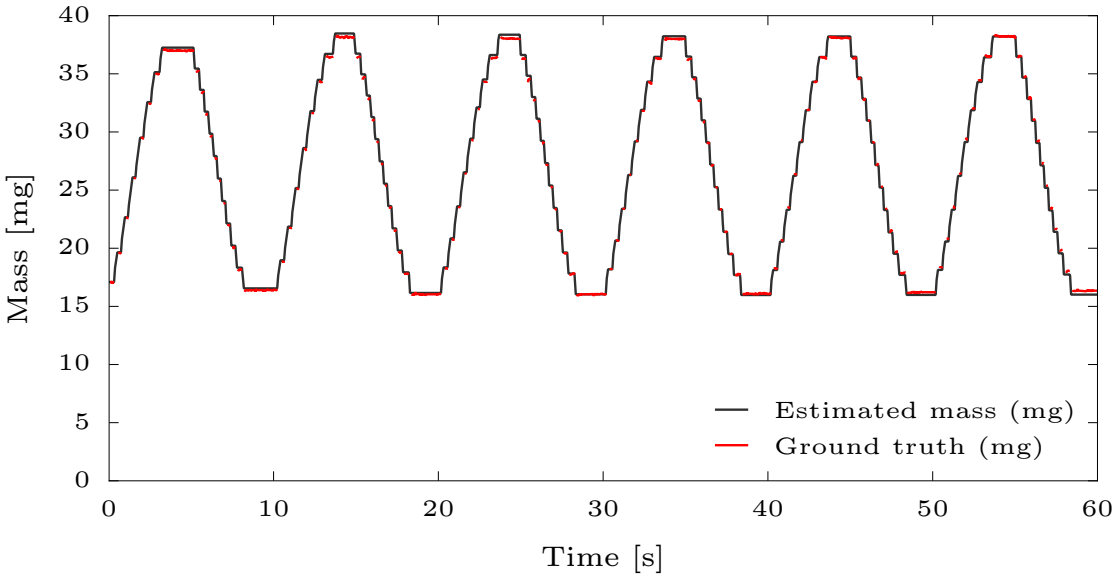

Fig. 4.9 Tracking performance of one calibrated channel over 60 s and 122 individual pulses. Figure published in Deimel, Radke, and Brock [25] ©2016 IEEE

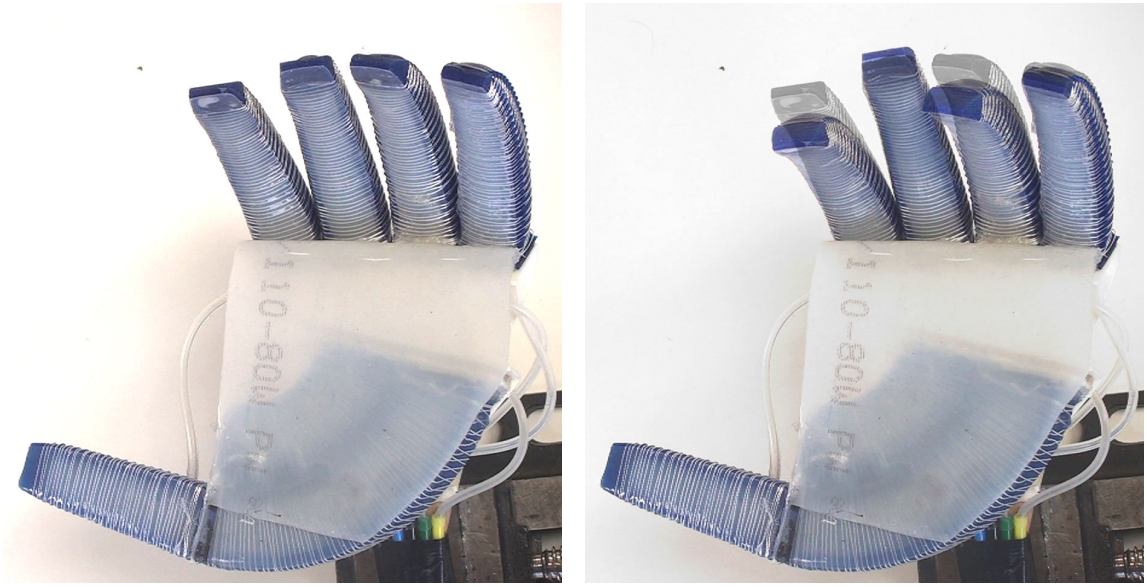

(a) Before (b) After 60 s

Fig. 4.10 Effect of drift after sinusoidal finger motion: Initial posture (left), posture after 60 s of continuous motion (right); middle and small finger return to the initial posture, while index and ring finger show a slight deviation.

4.4.4 Limitations

While air mass control has very desirable properties for controlling soft continuum actuators, major challenges still exist for using it to control soft hands. These are: managing mass drift, handling leakage, and reducing the control hysteresis.

Managing Drift Mass control based on mass flow integration inherently drifts over time. Therefore, this type of control is best suited for short or moderately long actuation patterns that require less than 20 to 50 pulses. If longer sequences are desired, then the mass reference can be reset at intermediate, well defined hand postures. A more challenging approach is to use sensor fusion to overcome issue, e.g. strain or bending sensors [78] could be used to compensate the long term drift. Proportional valves suffer from this problem too.

Leakage Mass control is sensitive to air leakage, as this leads to an error in estimated air mass independent of control accuracy. Quality valves usually are perfectly airtight, but sometimes can start leaking due to dust specks. More often, though, we experienced air leakage at quick-connect plugs. With respect to control, air leakage can be handled like drift. Alternatively, an additional leakage model could be introduced and calibrated to account for a constant, slow loss of air. In most cases though, improving the plumbing is a more straightforward approach to fix this issue.

Hysteresis and Actuation speed A big limitation of the current control system is the large amount of time it takes to physically open and close commodity pilot valves. These valves have a minimum pulse duration of 20 ms to 40 ms. This effectively limits the attainable hysteresis and actuation speed. We can trade off either by choosing a different choke, but their product is limited by the pulse duration. We can improve performance by an order of magnitude though, by changing to a system with faster solenoid valves, capable of 1 ms to 4 ms pulses.

Proportional valves would alleviate this limitation, as they provide an alternative to avoid short pulses altogether.

4.5 Conclusion

In this chapter we presented the motivation behind investigating equilibrium-point control as an alternative to classical position and force control for soft continuum actuators. We proposed air mass as the variable to control pneumatic soft continuum actuators, as it does not interfere with actuator motion due to compliance. We then demonstrated an implementation

of mass control using an existing pneumatic control system based on commodity components. The system performs well enough to enable continuous equilibrium-point control via air mass for tens of seconds, which ought to be enough for most grasping strategies. Due to its nature, mass control is very stable and can be extremely fast, especially compared to continuous pressure control.

Chapter 5

Towards Automated Design: Fast and Stable Simulation of Soft Hands

In this chapter, we develop a method to create dynamic simulations of grasping attempts with soft hands. We validate the simulation accuracy and also demonstrate that computation is fast enough to enable an interactive design work flow on a desktop computer and to enable automated design on cluster computing infrastructure.

5.1 A Simulation Model for Soft Hands

Simulation of soft hands has been an elusive topic so far. Soft hands can enact a huge number of possible deformations. Approximating them with kinematic chains requires a large number of individual links and joints, which typically leads to unstable simulations in rigid-body simulators that are optimized for small numbers of articulations. Another approach is to simulate soft hands by the finite element methods (FEM) of continuum mechanics. But the complex morphology of PneuFlex (and related) actuators with their intricate, embedded fiber patterns necessitates a very detailed model, which again leads a high computational cost. Even for actuators which employ homogeneous, isotropic materials (PneuNets, fast-PneuNets), simulation is still slow and therefore often limited to pseudo-static simulation.

This section outlines a model that goes considerably beyond the performance of prior examples of soft continuum actuator simulations, and provides the first practical implementation of a soft hand simulator capable of dynamical simulation of complete strategies. It builds on recent advances in ODE solvers, which improve the stability of kinematic chain (i.e. Cosserat beam) based models. Ultimately, having a fast simulation opens up a completely new research opportunity: Automated co-design of soft hands and their motion primitives to obtain reliable grasping strategies. By optimizing both control and hardware together, we could leverage the strengths of each domain in the best possible way to develop hands that fit well to motion primitives and vice versa. This outlook makes the findings of this chapter especially exciting.

Existing simulation approaches Dynamic Simulation of complete pneumatic soft hands has not been attempted so far, but simulation of individual actuators has. Even for single actuators, most simulations consider only pseudo-static motion and no environmental forces. There are two main approaches. One is to use volumetric FEM, where the actuator structure is modeled in its full complexity [80, 15]. A big disadvantage of this approach is that a sufficiently detailed model of a complete hand has hundreds of thousands of degrees of freedom that makes simulation very expensive. Because of this, all simulation attempts so far have targeted single actuators only. The second approach represents actuators as one-dimensional beams, either as Euler or Cosserat beams [93, 91, 92]. Continuous deformation is most often discretized by assuming piecewise-constant-curvature [93, 87], or by assuming constant-strain [92]. The latter enables coarser segmentation and thus faster computation. These beam-based models require several simplifying assumptions that reduce simulation accuracy, but nevertheless they are able to capture the main deformations of a soft hand. At the same time they use a radically lower number of degrees of freedom, on the order of

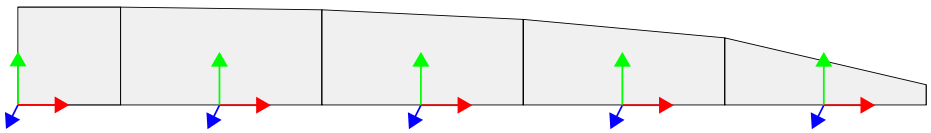

Fig. 5.1 A PneuFlex actuator gets discretized into several segments along the main axis, effectively forming a chain

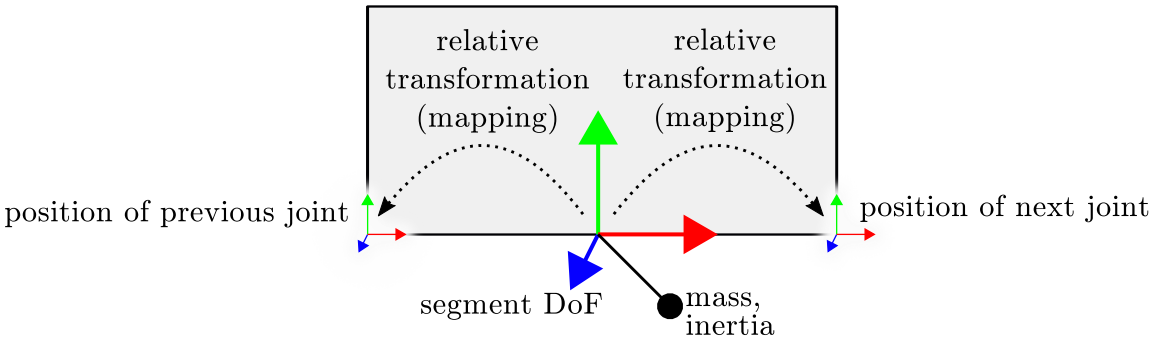

Fig. 5.2 Model of a single segment of an actuator. Segment position is represented as a single frame onto which two other frames representing the joint to the previous and next segment are attached. Masses and inertia matrices are aggregated at the segment frame.

$10^2 - 10^3$ versus $10^5 - 10^6$ degrees of freedom necessary for volumetric models. The model in this chapter also follows the second approach.

5.1.1 Discretization Strategy

In order to convert an actuator into a beam model, it has to be discretized. Figure 5.1 shows our discretization strategy. The actuator is divided into a small number of segments, usually between 5 and 10 per actuator. Figure 5.2 illustrates how each segment is then modeled as a single frame (rigid body). The frame is placed on the bottom of the actuator on the neutral layer defined by the embedded mesh. Two supplemental frames are defined at the beginning and the end of a segment, which represent the locations where adjacent segments connect. The mass and inertia of each segment is aggregated to a 6×6 inertia matrix expressed in the segment frame.

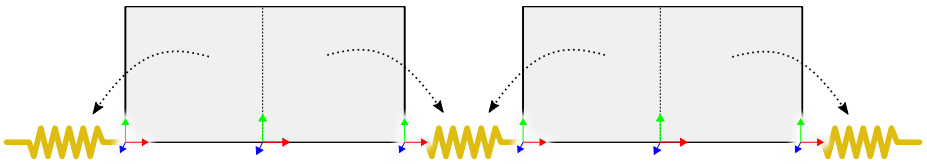

Fig. 5.3 Segments are connected to each other by a 6D spring. This component captures the mechanical compliance between the two segment's frames. Translational spring stiffness is very high compared to rotational stiffness, effectively implementing a Cosserat beam model.

5.1.2 Mechanical Stiffness

PneuFlex actuators are intrinsically compliant, we therefore include a spring-like element in between segments, as shown in Figure 5.3. This effectively creates a passively compliant joint in between two segments. The stiffness matrix of each passive 6D joint is:

$$K = \begin{bmatrix} \infty & 0 & 0 & 0 & 0 & 0 \\ 0 & \infty & 0 & 0 & 0 & 0 \\ 0 & 0 & \infty & 0 & 0 & 0 \\ 0 & 0 & 0 & k_{44} & 0 & 0 \\ 0 & 0 & 0 & 0 & k_{55} & 0 \\ 0 & 0 & 0 & 0 & 0 & k_{66} \end{bmatrix} \tag{5.1}$$

The spring's stiffness matrix given above is a simplification of the actual stiffness of a PneuFlex actuator. For example, when bending the actuator sideways, it usually also introduces a slight twist along the actuator, indicating that $k_{45} \neq 0$. A complete, accurate stiffness matrix has not been derived from a model yet. For now, we simply assume all non-diagonal terms to be zero, and translatory stiffness to be very large due to the embedded fibers.

5.1.3 Actuation

In order to actuate the beam model, we can choose between two methods: We could either model the air pressure as a torque acting in parallel to the passive spring, or we could deform the segments themselves into the shape they assume without external forces. This can be achieved by locally adjusting the joint locations relative to the segment frame. While the former method is the more obvious choice, the latter provides a better stability in the simulation. The reason we believe is, that the solver can consider the effects of actuation on

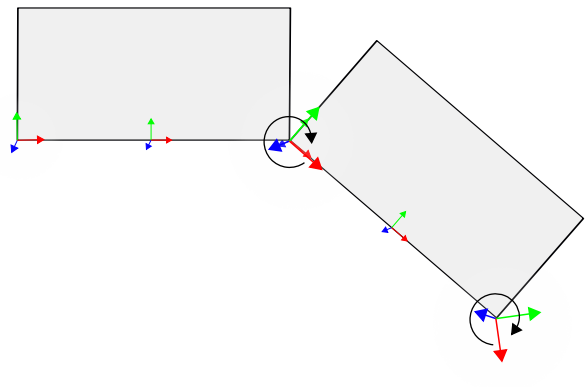

Fig. 5.4 Actuation, which in reality happens by inflation, is implemented by modifying the joint frame orientation relative to the segment's frame.

constraints within the time step, and not just after integrating the effect of a force after a time step.

Figure 5.4 shows the actual implementation of pneumatic actuation. For a given pressure, the equilibrium (zero external force) angle of the actuator at the joint is computed using the model from Section 3.4 together with a constant-curvature assumption around each joint. In addition to the design rules, the simulator also implements a refined computation of the actuation ratio, explained in the next paragraphs, to better approximate real actuators. Specifically, the refined model includes a model of the pressure-curvature nonlinearity and a compensation for side walls.

Approximation of nonlinear actuation ratio In order to approximate the actuation ratio (i.e. the pressure-curvature relationship) well, the simulation implements a nonlinear function related to Equation 3.37 instead of relying on the simpler Equation 3.32. For implementation, Equation 3.32 is augmented with two correction factors, one for the contribution of side walls (Equation 3.36) and one for the nonlinearity w.r.t. air pressure:

$$\kappa(p) = \frac{1}{8 \cdot G \cdot d} \cdot \text{ratio}_{\text{side walls}} \cdot \text{nonlinearity}(p) \cdot p \tag{5.2}$$

Unfortunately, Equation 3.37 states the nonlinearity in terms of curvature ($\text{nonlinearity}(\kappa)$) instead of pressure ($\text{nonlinearity}(p)$). The exact solution is quite convoluted, so we chose an approximation based on a sigmoidal function parameterized by the constants p_0 and a:

$$\text{nonlinearity}(p) = \frac{1}{\sqrt{a}} + \frac{p}{\sqrt{\frac{1}{a-1} \cdot p^2 + (a-1) \cdot p_0^2}} \tag{5.3}$$

The parameters can be adjusted to the theoretic model, but they can also be used to adjust to actual actuator behavior if data are available. Parameter a represents the ratio between the nonlinear terms at zero and infinite pressure, while p_0 parameterizes where transition between both values happen. First, we will consider an approximation to the theoretic model, and then compare it with validation data.

To set a, we first consider the nonlinear term of Equation 3.37 in isolation:

$$\text{nonlinearity}(\kappa) = \frac{2}{1+3\left(1+h\kappa\right)^{-4}} \tag{5.4}$$

This term modulates the slope (tangent actuation ratio) from 0.5 at zero pressure to 2.0 at very high pressures. We can therefore derive parameter a as:

$$a = \frac{\lim_{\kappa\to\infty}\frac{\delta\kappa}{\delta p}}{\lim_{\kappa\to 0}\frac{\delta\kappa}{\delta p}} = 4 \tag{5.5}$$

The change between slow and fast actuation ratios is dependent on the cross section shape and curvature, so we need to derive p_0 from geometric parameters. We do this by computing p_0 from actuator height h:

$$p_0 = -\frac{0.90}{h}\cdot 8\cdot G\cdot d \tag{5.6}$$

The resulting approximation function is illustrated in Figure 5.5, where it is plotted against both the linear and nonlinear analytic models from Chapter 3. The approximation matches the analytic model well, and much better than the linear approximation.

5.1.4 Collision Model

To enable collision detection and contact simulation, the beam model needs to be augmented with a mesh representing the surface of the actuator. A major disadvantage of the beam model is, that it does not provide information about the actuator surface. Fortunately, the linear blend skinning method [64] which is popular in 3D animation provides a computationally cheap heuristic to approximate the actuator surface, without computing the actual deformation.

The biggest drawback of this approach is, that this method keeps the cross section rectangular, instead of deforming into a circular shape at higher pressures. Accuracy could be improved by deforming the mesh into a tube prior to skinning, but is not implemented in the simulator.

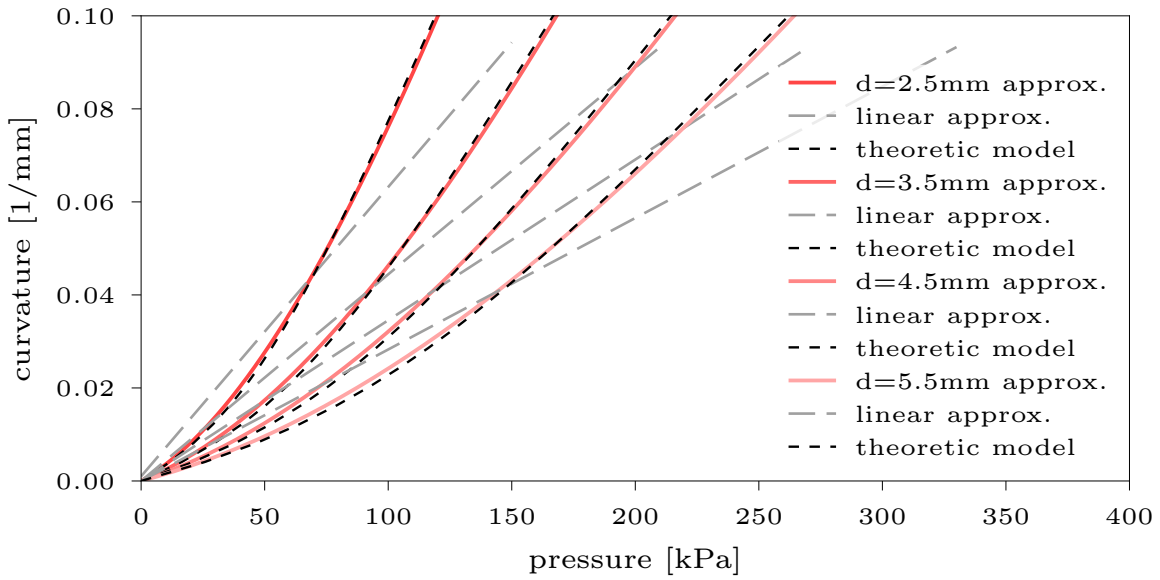

Fig. 5.5 Comparison of the pressure-curvature relationship of the nonlinear approximation of Eq. 5.2 (red) and the linear approximation of Eq. 3.32 (gray) against the theoretic model of Eq. 3.37 (black).

A second drawback of stock linear blend skinning algorithm is, that the actuator flattens visibly for large joint rotations between segments. This may introduce deviations in behavior between simulated and real soft hands. More sophisticated blending methods [55] could probably alleviate this particular problem.

5.1.5 Solver Configuration

Until now, we outlined the basic simulation model for PneuFlex actuators. An equally important topic for successful and fast simulation is the choice of algorithm for system resolution. This section details a solver setup suitable for soft hand simulation, and investigates the contribution of specific components to overall simulation reliability and speed. We rely on the excellent set of tools provided by the SOFA project[1] [1], especially its Compliant module [114].

Compliance Formulation of Constraints A key problem for the formulation of a discretized beam-like model of a PneuFlex actuator is the implementation of translational springs that approximate the almost inextensible passive layer. These springs need to be very stiff with respect to the rotary degrees of freedom which are mostly governed by rubber deformation. This results in a very large range of element values in the Karush-Kuhn-Tucker

[1] https://www.sofa-framework.org/

(KKT) equation system which needs to be solved at each time step. The matrix has a bad condition and this greatly affects the convergence speed of ODE solvers, i.e. it increases computational cost.

Recently, Tournier et al. [114] developed a method to circumvent this issue by modeling springs as a constraint with low (or even zero) compliance. Compared to a spring with stiffness, the compliant constraint is added in a different part of the KKT matrix, and because the respective compliance values are very small, the condition of the matrix does not deteriorate. This formulation leads to an improved stability and convergence speed of the simulation.

Sequential Impulse Based Solver Another key component for a simulation is the solver employed to invert the KKT matrix. A robust choice for the simulation of soft hands is a sequential solver (SOFA component `SequentialSolver`) that computes corrective impulses for each degree of freedom.

We found that this solver greatly outperforms conjugate gradient based equation solvers (e.g. as implemented by the SOFA component `CGLinearSolver`) in terms of stability when simulating more than a hundred contacts.

Time Integration Scheme For time integration, we use a regular Implicit Euler integration scheme. We evaluated both linear (SOFA component `CompliantImplictEuler`) and nonlinear version (SOFA component `CompliantNLImplicitEuler`). With the necessity of frequent collision detection in mind, we favor the faster, linear version.

Collision Detection Collision detection is done using SOFA's default implementation. In our implementation, we additionally shrink the collision mesh by a small offset (1.0 mm) and set the collision to occur at a positive distance ($contactDistance = 1.0$ in SOFA's `NewProximityIntersection` component). This erode-dilate like operation effectively smoothens any sharp edges and corners of the collision mesh. This better reflects the actual surface of the actuator, but we also noticed an improved stability in grasp simulations. This improvement in stability was recently also reported with the Klamp't simulator [95], where they implemented a collision method referred to as "BLEM", which effectively results in the same behavior as our modification.

5.1.6 Simulation Speed

Simulations of grasping with soft hands has two application scenarios: interactive hand design by an expert user, and automated design on e.g. a computation cluster. For interactive

(a) Mechanical Degrees of Freedom (b) Visualization (c) Complete scene

Fig. 5.6 Simulation configuration for grasping a cylinder from a table surface with the RBO Hand 2

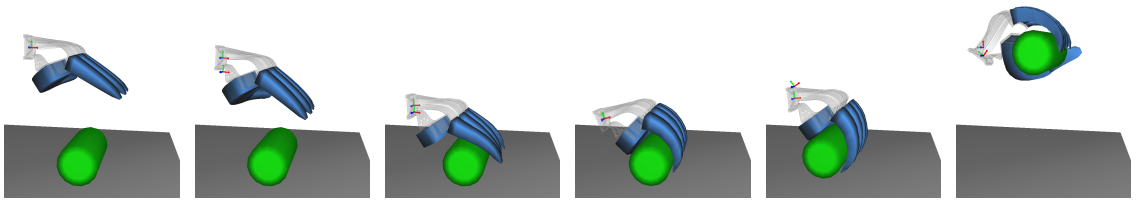

(a) 0 s (b) 0.2 s (c) 0.4 s (d) 0.6 s (e) 0.8 s (f) 1.0 s

Fig. 5.7 Illustration of a grasp attempt simulated at 10 ms time step with the default solver configuration

use, the simulation should run in real-time, or near real-time to give the designer an intuition on the dynamics. For automated design we simply want to be as fast as possible but we need to ensure that simulation results stay plausible most of the time, because manually checking millions of grasps is not possible.

In order to characterize the simulation speed attainable with the presented model, we measured computation times on a typical use case. The simulation contains three object, a cylinder to grasp, a table surface the cylinder rests on, and the RBO Hand 2. Its morphology is discussed in detail in Chapters 7). The hand model and the simulation scene are visualized in Figure 5.6, while Figure 5.7 illustrates the progression of a simulated grasp attempt. The hand is constructed from six individual PneuFlex actuators, which are attached to a common wrist frame. The two parallel, curved actuators of the palm are modeled as a single PneuFlex actuator that can actively bend and twist. Each actuator is discretized to a number of segments, which determines the overall number of degrees of freedom in the simulation. In the experiment we use five segments per actuator for a fast but slightly inaccurate deformation model, and fifteen segments for a slower but more accurate modeling. The simulations were computed on a regular desktop computer (Intel® Core™ i5-6600K

	precision	max. iterations	omega
fast	1e-2	100	1.5
default	1e-4	500	1.3
stable	1e-5	2000	1.0

Table 5.1 Tested configurations of the `SequentialSolver` component

Segments per actuator (segments total)	Solver configuration	time step 1 ms	2 ms	5 ms	10 ms	20 ms	50 ms
5 (30)	fast	0.06	0.13	0.28	0.45	0.89	1.92
	default	0.04	0.06	0.10	**0.17**	0.34	0.84
	stable	0.02	0.02	0.04	0.06	0.11	0.26
15 (90)	fast	0.02	0.04	0.11	0.18	0.27	0.60
	default	0.01	0.01	0.02	**0.04**	0.08	0.22
	stable	0.00	0.00	0.01	0.01	0.02	0.06

Table 5.2 Run times in seconds per simulated second for different time steps and configurations. Bold values indicate results for recommended parameters which balance speed with the stability margin. Light gray values indicate results where the simulation is stable, but collisions are missed due to the large time step.

CPU @ 3.50GHz), using SOFA simulator version v16.12. Please note that all simulator components used are single threaded, i.e. only one CPU per simulation was used. We simulated two different actuator discretizations and three different solver configurations with simulation time steps in the range of 1 ms to 50 ms. The solver parameters for each configuration are listed in Table 5.1. The solver configurations were chosen to cover the range of possible trade off between efficiency and stability. The *fast* configuration shows visible jumps in object position between time steps, but demonstrates the upper limit on simulator speed. The *stable* configuration is reliable and accurate for various simulation scenes, and provides a conservative bound when correctness and reliability of results are paramount. The *default* configuration represents a balance between both, yielding good simulation speeds while maintaining a stability margin so that we can expect more complicated simulation scenes to remain stable too.

Table 5.2 shows the resulting simulation speeds as a ratio of simulated seconds per second of computation time, i.e. higher is better and a ratio of one or above represents real-time simulation capability. The simulation itself stays stable for very small time steps and also for very large time steps up to the maximum tested 50 ms. To emphasize the stability of the simulation, a conjugate gradient based solver was not able to converge at all for this simulation, probably due to the large number of redundant contacts between hand and object which is typically in the range of 50 to 150. For the largest time step, values are grayed out

because at this time step collision detection was not working properly any more, and resulted in penetrations of hand-object and object-table collision meshes. Nevertheless the values are reported as they indicate the performance that could be reached with improved collision detection, as the constraint solver still converges. But even for less aggressive configuration (fast configuration and 20 ms time step), the simulation is able to run close to real-time. This indicates that even the current simulation model is already suitable for interactive design, and that reliable desktop real-time performance is well within reach, e.g. if the implementation is parallelized or ported to run on a GPU. For the automated design use case, the results are also promising. Indicated by the results in bold, a grasp attempt can be reliably simulated at approximately $0.1\times$ real-time. For a moderately sized compute cluster with 2000 CPU cores, this translates to a throughput of about one million grasps per day. This makes it possible to search the design space of soft hands for novel solutions, or to locally optimize the many available shape parameters. Furthermore, it opens up the possibility to co-design motion primitives and hand morphology together. This approach may enable the design and optimization of soft hands to specific task domains, which would provide quick solutions to existing problems and also intermediate steps towards a – currently hypothetical – general purpose soft hand.

The presented speed test only considered the efficiency of simulating complete grasps. The next section will complement it by validating the quantitative and qualitative accuracy of the underlying actuator model.

5.2 Validation Experiments

In order to evaluate the accuracy of the simulation model for PneuFlex actuators – and to validate its implementation – we conducted three experiments. The first experiment validates that the simulation is insensitive to the chosen discretization. The second experiment validates the correct pressure-curvature relationship. The third experiment validates the absolute stiffness of an actuator.

5.2.1 Discretization

Ideally, the simulation should be tolerant to the chosen discretization, i.e. the segment length should not have a considerable influence on the overall mechanical properties. If it does, it would indicate a poor discretization strategy.

We therefore compare in simulation a set of five identically parameterized actuators, that only differ in their number of segments. To compare them, we recreated the blocked fingertip

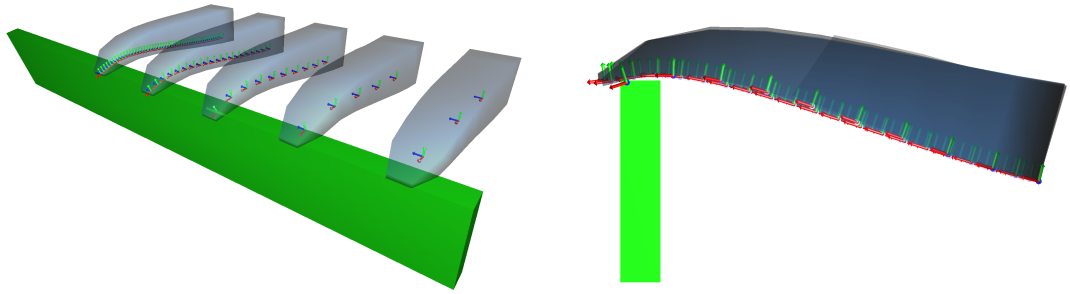

(a) Simluation scene (b) All actuator shapes are congruent

Fig. 5.8 Simulation to validate the the influence of discretization on the simulation accuracy. The simulation scene contains five P10 actuators modeled with (f.l.t.r.) 50,20,10,5 and 3 segments, pressing against a block obstacle with the fingertips. The orthonormal projection in (b) shows that segment size does not influence the deformation behavior.

experiment from Section 3.5. Figure 5.8 shows the simulation scene. Figure 5.8b shows the scene from an orthonormal view where all fingers overlap. This view makes it easy to see that all actuators show practically the same static deformation, except at the outermost fingertip. The deviations there are mostly caused by differences in the contact location and the ability of the finer discretized fingers to better adapt their shape to small obstacle surface features.

Overall, the experiment shows that static actuator behavior is not affected by the choice of segment length. The shape deviates noticeably from the other models only for the actuator with three segments at the fingertip. As simulation complexity scales with the third power of degrees of freedom though, it is advisable to lean towards a low number of segments. Additionally, it improves solver stability. This validation experiment suggests to use a segment length of about 10 mm to 20 mm by default.

5.2.2 Actuation Ratio

We can check the actuation ratio of the simulation against the data of freely bending actuators from Section 3.5.1 (also published in Deimel and Brock [23]). We recreated the experimental setup in simulation, which is shown in Figure 5.9, and recorded the orientation of the last frame at the pressures of the ground truth data. We changed the shear modulus of the rubber to 1.1 times the nominal value of 67 kPa (Dragon Skin 10) , in order to adjust the scale of the simulation model to the ground truth data. Please note that this is well within the range of deviations we have to expect for material properties of silicone rubbers. Figure 5.9 shows the direct comparison of the theoretic model to ground truth for the four actuators. The simulation model fits actuators with low hull thickness well. It deviates clearly for the actuator with the

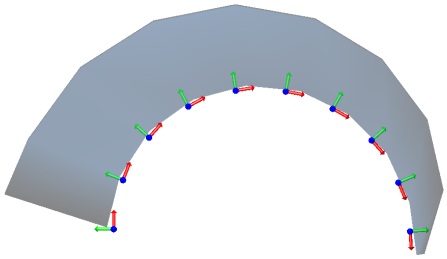

Fig. 5.9 To validate the actuation ratio, four actuators were inflated in simulation without contact and compared against fingertip orientations measure on real actuators from Figure 3.12

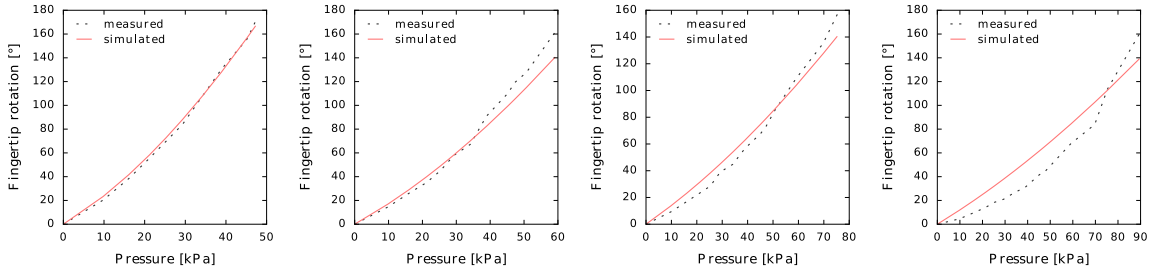

(a) 2.5 mm (b) 3.5 mm (c) 4.5 mm (d) 5.5 mm

Fig. 5.10 Comparison of simulated fingertip rotation of four actuators with different hull thicknesses to their ground truth data from Figure 3.11.

thickest hull, in Figure 5.9d. Most of the error could be removed by increasing the parameter a of Equation 5.3 with increasing hull thickness, but it is unclear what the cause of this effect is. Overall though, the theoretic actuation ratio model incorporating the corrections from Section 5.1.3 does a very good job at modeling the actuator motion out of the box.

5.2.3 Stiffness in Actuated Direction

The scaling behavior of stiffness design rule has already been demonstrated in Section 3.5.2. Corroborating this, we can compare the actuator shape in Figure 3.13c with the simulated equivalent in Figure 5.8. The curvature along the actuator and the curvature in simulation are very similar. This indicates that the relative stiffnesses in simulation model those in real actuators well.

In addition to the relative stiffnesses, we also validate the absolute magnitude of finger stiffness and the pressure-force relationship with a blocked-fingertip experiment. Figure 5.11a shows the experimental setup. Fingertip motion is restricted by an obstacle, which is instrumented to measure the applied contact force. The finger is then inflated to different pressures, and the resulting contact normal force is measured. The measurement was repeated 10 times for each pressure and averaged. Figure 5.11b shows the corresponding simulation setup. Similar experimental setups have been used to assess the strength of other pneumatic soft continuum actuators before [87, 80].

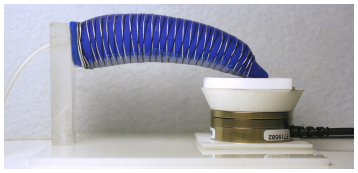

(a) Experiment

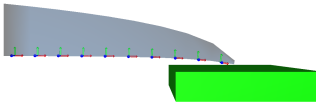

(b) Simulation

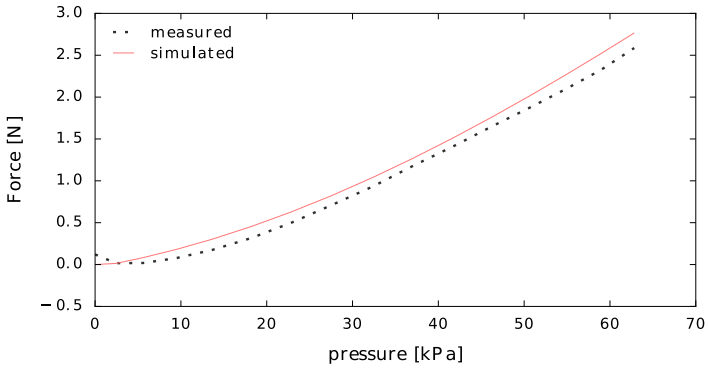

(c) Comparison with different simulated heights

Fig. 5.11 Validation of the stiffnesses computed by the actuator model. The test compares the vertical contact force generated by a P10 actuator with empirical measurements.

Figure 5.11c shows a comparison between real actuator and simulation. The simulation model recreates the contact forces with high accuracy, without adjusting any parameters, such as nominal actuator height. This accuracy is rather unexpected, as we use some strong simplifications for the analytical model, such as assuming a rectangular cross section. Another promising detail is the good match in nonlinearity, even though the mechanical compliances are modeled just as linear springs. The nonlinearity is caused by the nonlinear actuation ratio instead. The spring linearity seems to be a convenient side effect of choosing to model actuation by deforming the links instead of applying joint moments, which would then require a nonlinear spring model.

5.2.4 Stiffness in All Directions

The analytic model employed for the simulation does not provide us with stiffness estimates for the two unactuated rotation axes. As a very crude approximation, we set their stiffnesses to be the same as the stiffness of the actuated axis. This is a strong assumption, as the shape of a segment differs for ZY, XZ and XY plane. So we conducted another validation experiment that gathers data depending on the stiffnesses of all three axes. The experiment is complicated by the fact that an inflated, bent actuator behaves different from one that is not inflated. So we cannot gather data on a straight actuator, which complicates the analysis.

Figure 5.12 shows the chosen experimental setup. We instrumented a finger with a force-torque sensor on its base and an L-frame on its fingertip to record fingertip motion with a marker-based motion-capture system. The finger was inflated to rotate the fingertip by 90°, which corresponded to a pressure of 31 kPa. We then applied consecutive disturbances to the fingertip in three distinct directions, which are shown in Figure 5.13. The disturbances were

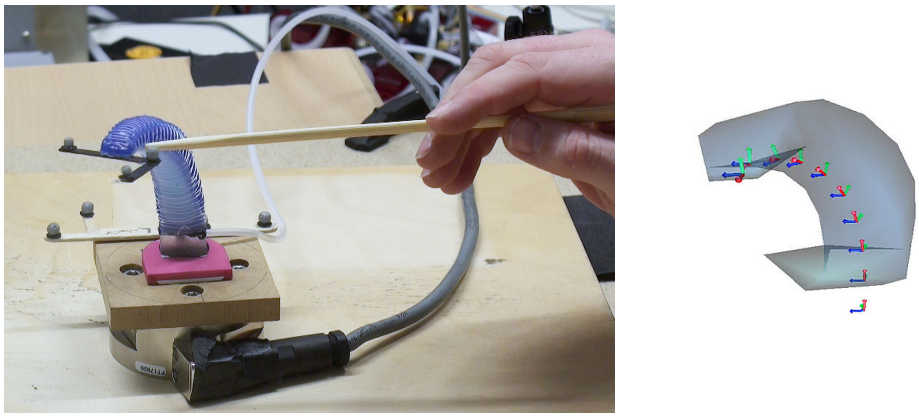

(a) Data acquisition

(b) Reenactment in simulation

Fig. 5.12 An instrumented actuator is inflated and then disturbed by forces applied to the fingertip. The resulting force wrenches at the base of the finger are recorded with a force-torque sensor underneath the finger. The fingertip motion is then reenacted in simulation and the resulting force wrench at the finger base compared to the ground truth.

applied with chopsticks to ensure marker visibility and a clear contact point location. During the recording, we bent the finger sideways left two times, sideways right two times, down two times and up two times. Finally we apply a torsional moment by rolling the fingertip between two chopsticks several times. This disturbance results in a counteracting force wrench at the base of the actuator, which is measured by the force-torque sensor.

In simulation, we recreated the experiment by commanding the same air pressure and then imparting the fingertip motion onto the last actuator segment. We recorded the resulting force wrench acting on the fixed base segment, and compared the torque trajectories. The translational forces are mostly transmitted by the passive layer which makes them very sensitive to position errors between simulation and motion-capture data. We therefore only consider torques here. The results for the complete trajectory is shown in Figure 5.14. Overall the moments are tracked very well, considering the strong assumption we made for setting the stiffnesses. The simulation shows a slight drift in moments during the experiment. This is actually caused by a minute hysteresis in the actuator motion, which makes the finger to not return exactly to the initial position. The hysteresis is on the order of 1 mm to 2 mm, the visible effect in Figure 5.14 testifies the sensitivity of the setup.

The simulation deviates from the measurements at the sideways motions (7 s, 10 s, 18 s and 23 s). The moment around the y axis is considerably less than expected. This may indicate that the stiffness of the axis along the actuator, which aligns with the y axis at the base of the

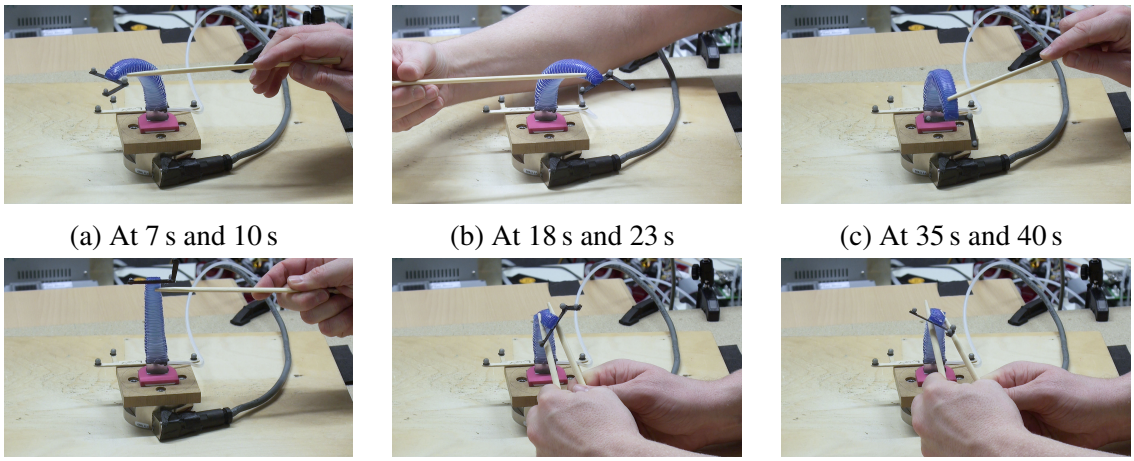

(a) At 7 s and 10 s (b) At 18 s and 23 s (c) At 35 s and 40 s

(d) At 45 s and 55 s (e) At 67 s, 72 s, 79 s and 84 s (f) At 70 s, 75 s and 80 s

Fig. 5.13 Disturbances applied during the measurement. Left-right corresponds to the x-axis, up-down to the z-axis of the world frame and F/T sensor data.

finger, is underestimated. But the torques are also influenced by other axes due to the curved shape of the actuator. This makes a clear interpretation of the source of this error difficult.

Another deviation can be seen at the x axis torque at 35 s and 40 s. Here the simulation overestimates the stiffness of the actuator in the bending direction. This deviation does not appear on the two subsequent disturbances in the opposite direction. The cause of this nonlinearity is not known, but we suspect it is related to the fiber tension in the passive layer.

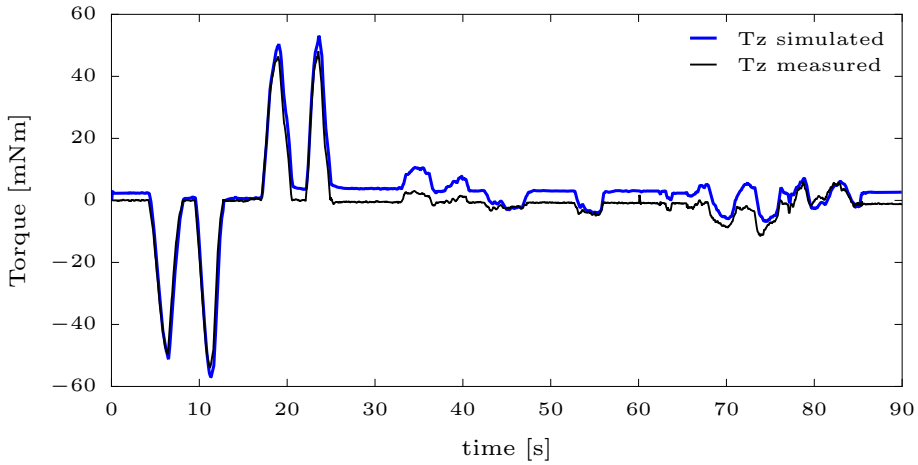

(a) Torque around vertical axis (z-axis)

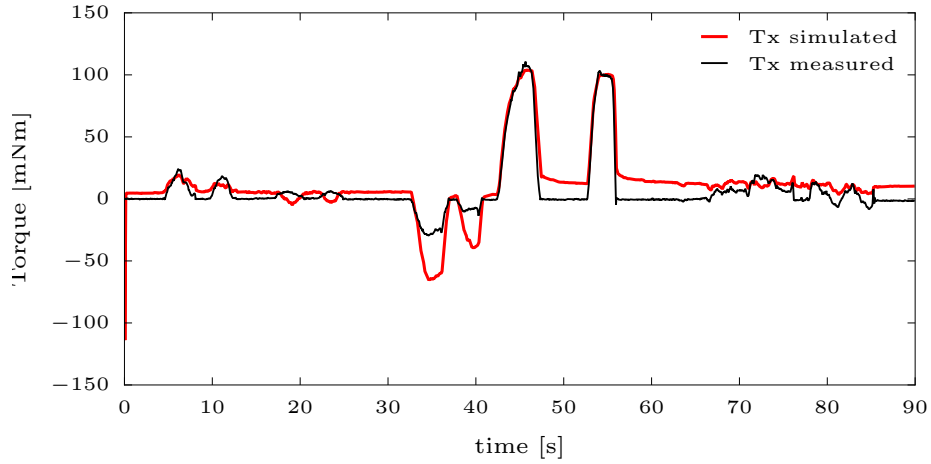

(b) Torque around left-right axis (x-axis)

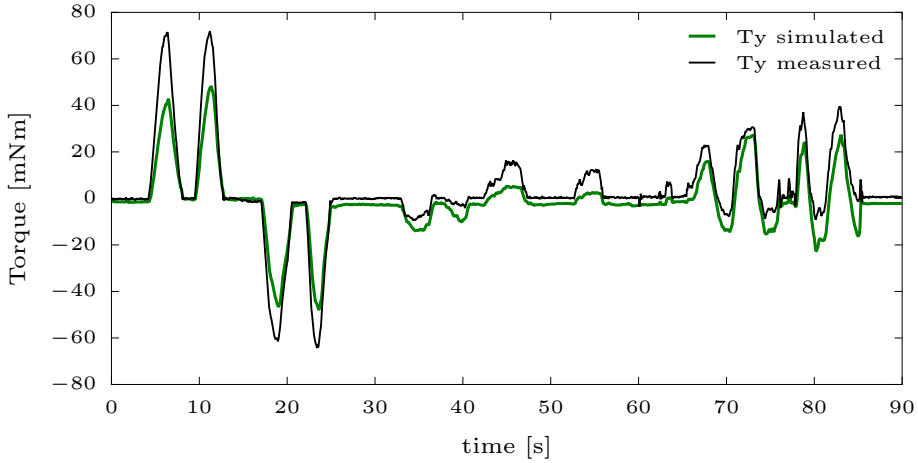

(c) Torque around axis towards camera (y-axis)

Fig. 5.14 Comparison of simulated torques (solid) vs. measured torques during the complete recording.

5.3 Conclusion

In this chapter we presented a comprehensive model for dynamic simulation of PneuFlex actuators and complete soft hands. The simulation is fast and stable, and can reliably simulate complete grasping attempts at a speed of about $0.1\times$ real time on a regular desktop computer. With proper parallelization, real-time performance for interactive hand design is within reach. The performance is also sufficient for attempting automated design of soft hands to specialize them to specific applications. Additionally, we performed a number of experiments to validate the simulation model against real actuators. They indicate that the presented simulation model is capable of capturing the main mechanical behavior of the PneuFlex actuator. Both motion and applied forces are accurately simulated, and errors do not exceed levels which tolerances in material parameters and manufacture would introduce anyway. While the validation results are all consistent so far, they should be corroborated with further experiments using a wider variety of actuator shapes. Another limitation of the current model is, that we can only compute the compliance along the bending axis, while the other two axis are simply assumed to have an equal stiffness. It is unlikely, that this is a good heuristic for all actuator shapes. The simulator would therefore greatly benefit from a complete model that accurately estimates rotational compliances for all axes.

Part II

Properties of Soft Hands

Chapter 6

The Soft Manipulation Paradigm

Soft hands are motivated by the Soft Manipulation paradigm, which considers grasping as a process, facilitated and simplified by the mechanical interaction between hand, object, and environment. In this chapter we will build the paradigm from a few basic observations and elaborate on its consequences to robot systems.

6.1 The Path To a New Approach in Grasping

Often, soft hands are mistaken as classical robot hands, just with lower payload. Indeed, the virtues of soft hands cannot be appreciated unless one changes his view on what is important to robust and reliable grasping. This shift in perspective – a paradigm shift – requires us to rethink methods, tools and language. But we believe we have to face this effort. Chapter 1 already highlighted the main problem of the classical, *mechanistic paradigm* to grasping. It presupposes almost perfect perception and actuation to handle the highly nonlinear behavior of contact points. To make things worse, we avoid many contacts in contact point based models due to the incurred computational complexity, but more contacts make a robust grasp likely. Over the years research provided many incremental changes such as more accurate hands and more sophisticated perception, but today's robots still cannot grasp reliably unless their environment is carefully selected or engineered to support them. The time seems ripe to completely rethink the way we explain and understand grasping.

In this section, we will first give a condensed explanation of a method designed to achieve such profound changes in understanding. Then, we will apply it to the phenomenon of grasping to create a new paradigm, *Soft Manipulation*, which motivates the research into a completely new type of robot hands: soft hands. The term Soft Manipulation was first used for the "Soft Manipulation" project of the EU Horizon2020 programme, and incorporates several prior concepts, such as the Environmental Constraint Exploitation hypothesis [20, 32], soft synergies [46] and shape adaptability [30]. The reader is invited to jump to Section 6.1.3 in case they are more interested in applying the Soft Manipulation paradigm rather than understanding its origin.

6.1.1 Presencing: A Method for Constructing New Paradigms

In order to understand what to do to construct a new paradigm, we can let ourselves be guided by the triple-loop-learning technique [85]. The name refers to three distinct modes of learning-by-interaction with a phenomenon. These three loops are ordered in terms of consequences and required cognitive effort: learning single facts (easy), consolidating a body of facts by reflection (difficult), and changing how possible facts are formulated (hard). We will use the latter loop to construct the Soft Manipulation paradigm. The first loop of interaction with a phenomenon formulates hypotheses (i.e. possible facts), tests them, and refines them iteratively to arrive at robust facts. This is the by far most common mode of learning and progress, and well suited for incremental improvements. It lends itself to dividing research into small, well defined questions that can be tackled independently of each other. The second loop reflects on deviations and failures uncovered by the first loop. As

a reaction, we incrementally adjust axioms and explanations to account for the deviations. This mode of learning tries to organize a larger set of hypotheses into a coherent story, based on repeated patterns or common axioms. In research, outcomes of this type of learning are usually communicated with manifests, position papers, reviews, and standard textbooks.

Reflecting on existing bodies of verified or falsified hypotheses implies that we don't question whether we ask the right questions in the first place. The frame of reference we use to formulate hypotheses is not changed. Peschl [85] and others therefore propose yet another distinct learning loop, which operates *above* the level of reflection. In this third loop of learning we learn entirely new ways of looking at a phenomenon. We use metaphors like "changing the point of view", or "reframing the problem" to refer to this process. If successful, we create a new paradigm which suggests completely new questions and possibly offers an escape route from impassés of prior paradigms. To give an example from Physics, the introduction of the quantum mechanics provided an escape from the stubborn contradictions that arose when classical mechanics was applied to systems on an atomic scale. It is important to understand that paradigms can coexist though, we can switch between them based on their utility for a given problem. Mechanics is not superseded by quantum mechanics and both have their legitimate uses today. In this chapter we will argue for a similarly complementary perspective on grasping, away from the mechanistic description to one centered on robustly executable interaction heuristics.

The difficulty in third-loop learning is, that we have much less practice and experience than for first and the second loop learning. Therefore, when we want to engage in third-loop learning, we inadvertently fall into the practices of second-loop and first-loop learning by habit. One cognitive technique to help here is called "presencing" [85], which is related to U-Theory [102]. We first try to explain an observed phenomenon and then we try to formulate the hidden assumptions we made. We then iterate by formulating an explanation of the phenomenon while avoiding the identified assumptions. When this iterative, reflective process is done several times, we are not guaranteed but more likely to arrive at descriptions that are not tainted by our existing paradigms – at least as untainted as we can hope for. The iterative process also helps us to notice "blind spots", i.e. to notice patterns that are ignored by the existing paradigm. At this meta-level we cannot formulate the precise, well defined hypotheses we need for empirical experiments, though. We need to take our newfound understanding and propagate it back to the second-loop and first-loop level.We can do this by e.h. formulating first principles coherent with the observations, and then testing hypotheses informed by those principles. Of course, negative results may force us to reconsider our first principles or our proto-paradigm. This mutual influence is emphasized by the *loop* term in triple-loop learning.

In this chapter, we will apply this technique to grasping. We will first describe observations that are not readily explained by the mechanistic paradigm. We will then use these descriptions to propose new principles for grasping, and translate them into concrete hypotheses on how to build robots that can grasp.

6.1.2 Observations Not Described By Mechanistic Paradigm

We begin with listing several observations that have been mostly ignored in classical grasping, as they are not considered important in the mechanistic paradigm.

Observation 1: Compliance is always present There are many examples of robot systems that are capable of grasping and manipulation, although they usually are not versatile and competent. For these systems, grasping is not their focus of work, so their creators "make things work" by e.g. using scripted motion primitives that work , but only under a strictly defined set of circumstances. Conspicuously, the manipulator hardware of such systems always includes soft and compliant parts: parallel jaw grippers get padded with foam, joints are made dislocatable [45, 8, 30], and the surface of robot hands almost always gets covered in rubber [45, 8]. Several recent gripper designs even rely on completely soft structures [2, 53]. It seems like compliance and softness is always present in any system capable of grasping. Even though in the mechanistic paradigm we consider this compliance disadvantageous for reliable modeling and control.

Observation 2: Most grasps are lazy A second observation can be made by looking at how humans grasp. Humans are perfectly capable of "precision grasping" by placing few contacts – usually fingertip contacts – at very specific locations. But most of the time, especially when they do not pay attention to, humans seem to apply rather simple and robust heuristics for grasping. Quantitative analyses of grasping behaviors show, that the vast number of everyday grasps are power grasps [36], and that the interaction before attaining a grasp can be classified into relatively few strategies [49]. Again, the mechanistic paradigm is at odds here, which focuses on precision grasps with their small number of contacts.

Observation 3: The triangle of hand-object-environment interaction The third observation highlights a property of the world often ignored by mechanistic models: An object almost always is surrounded by other objects, e.g. a table surface. Additionally, during the act of grasping contact with the object to grasp has to be established before contact with other, environmental objects cedes, which creates a mechanical interaction between hand, object and environment. In many examples of robust grasping strategies, these interactions

are not instantaneous but extended in time [27, 84, 74]. The popular model of grasping [89] ignores this completely and considers the transition to be an instantaneous event. Interactions with those environmental objects are seen as either irrelevant or detrimental.

Observation 4: Most grasps use the environment Two independent studies show that humans intentionally prefer contact with the environment before and during grasping [61, 32]. It seems like humans, when not being told to otherwise, prefer to use power grasps and simple heuristics that involve auxiliary contact with the environment [90, 49]. More refined pre-grasp manipulation is mostly seen in response to failure of initial, simple strategies. The same can be observed with robot grasping: many strategies work only in the presence of certain objects, e.g. a flat horizontal surface [62], an edge [32], or a corner [32].

6.1.3 Guiding Principles for Robust and Reliable Grasping

We can now use these observations (and the supporting related work) and condense them into principles that sketch the new paradigm.

These principles may not be universally true, but they are good first approximations. Most importantly, they provide us with valuable anchors to resist our habit to think in the prevalent mechanistic paradigm.

Consider power grasps as the main mode of grasping. The model grasp is the power grasp which envelopes the object, and makes contact with a large area of the hand.

Use contact redundancy and large contact areas to make a grasp reliable. As a corollary to the previous principle, it gives a concrete design guideline that can also be applied to precision grasps.

Use compliance to balance contact forces heuristically. As the number of contacts are high and their location uncertain, use compliant joints and structures to balances contact forces sufficiently well, instead of computing the perfect balance.

Provide compliance mechanically if possible. Mechanical compliance is superior to closed-loop control in terms of control bandwidth and costs. It should therefore be the first choice whenever possible.

Outsource control to the hardware. Adding complexity to the hardware can be used to simplify higher-level control, i.e. we can outsource parts of control into the morphology by using compliant and coupled structures.

Make unexpected collisions non-catastrophic. As grasp strategies are selected based on incomplete world knowledge, some attempts will fail. Make sure that failures do not break the hand, so the risk of trying out a grasp strategy remains low.

Use compliant contact with the environment before and during grasping to constrain undesired motions. Except for very rare cases, the object to grasp is always in contact with another, environmental object such as a table or box. Use the environment to your advantage, e.g. for caging, instead of avoiding contact with it.

Compose grasping strategies by sequencing interactive, haptic behaviors. Grasping is a complex, prolonged interaction, not a state transition. But the process can often be segmented into phases with distinct purposes.

Act to reduce uncertainty instead of adjusting to variations in the scene via perception. Certain interaction patterns reduce variations in spatial relationships which then don't need to be modeled anymore during subsequent steps of the grasping strategy.

Formulating these principles is an ongoing process and not yet finished. Each of these principles will need to be corroborated with empirical evidence, and possibly refined or amended. We believe though, that they provide a valuable starting point to rethink robotic grasping and that they provide a valuable frame of reference to investigate new grasping strategies and to organize existing work.

We also want to stress again that adopting the proposed paradigm does not preclude one from using the mechanistic paradigm where it provides useful results. Both paradigms have their strengths, and we should strive to become proficient in both.

6.2 Empirical Support for Soft Manipulation

In the previous section we identified several principles for the new paradigm, which we call *Soft Manipulation* due to its central reliance on compliant actuation. The remaining chapters will investigate empirical experiments to corroborate the principles, with a special focus on the role of soft hands. Here, we will take a broader look at existing literature that already

employed some of the proposed principles to corroborate the usefulness of the new paradigm, but also to highlight the profound changes that are needed on all levels of a robotic system to implement Soft Manipulation.

The research field of compliant and underactuated robots provides a large body of literature that elaborates the advantages of mechanical compliance. The SDM and iHY hands demonstrated the use of coupled finger joints to simplify hand control [30, 83]. They also show that adding compliant flexure joints can be beneficial to grasp quality as each link can (within limits) adjust to the object's local surface. Another impressive example of mechanical force balancing heuristic is the Pisa/IIT SoftHand [9]. It uses a single motor and tendon to actuate nineteen joints. The balance between them is determined by a complex interaction between rubber springs, friction, and the object shape. Despite the complexity of the interaction, the hand provides a surprisingly robust and easy tool for grasping and manipulation.

From the side of planning and control, there is an important line of research that fits almost perfectly into the new paradigm. Mason pioneered the planning with uncertainty-reducing actions [74], and the notion of "funnel" actions that allow chaining them to construct predictable action sequences [75, 73]. Indeed, those early papers served as an important source of inspiration during the development of the Soft Manipulation paradigm.

Corroborating evidence can further be found in research on how humans execute robust grasping behavior. They seem to utilize some of the proposed principles to arrive at a successful grasping strategy. Eppner et al. [32] show that humans intentionally favor contact with the table surface if they are confronted with uncertain perception, a finding that was corroborated by independent research [61]. Kaneko et al. [57] observed a grasp strategy that uses the table surface and rolling contact to slide under small cylindrical objects, an idea that was also picked up and implemented by Kazemi et al. [60].

Another source of evidence comes from the results of recent manipulation competitions, such as the DARPA ARM challenge and the Amazon Picking Challenge. In the key opening task of the DARPA ARM challenge, successful teams relied on using intentional collisions to align the key with the lock, enabling successful insertion actions despite the comparatively large position inaccuracy of the used arm. Compliant motion and preparatory actions were also a key ingredient with the winning entry of the first Amazon Picking Challenge [33]. In this challenge, robots had to autonomously pick objects from compartmentalized shelves. In the winning system, perception only provided an approximate bounding box of the object. The overall grasping strategy relied on compliant motion to adjust the position of the robot's suction cup end effector in order to contact the object's surface. It also used either the walls or the floor of the shelf to cage objects prior to activating the suction cup, by choosing from

three different approach directions. This greatly simplifies the requirements on perception and planning, which facilitated a reliable execution of the system during the competition.

6.3 Exploiting Latent Environmental Constraints to Motion

Switching from the mechanistic paradigm to the Soft Manipulation paradigm has profound consequences on all levels of a robotic system. Especially the internal representations that separate perception, planning, control, and hardware need to be adapted to reflect the change in focus. But what replaces the mechanistic concepts of hand posture, contact points and force balancing? In this section, we develop one possible answer to this question, in order to give the reader a context for the remaining chapters of this thesis.

We propose that grasping should primarily be understood in terms of interaction patterns between multiple bodies, often more than two. The interactions are extended in time and not instantaneous mechanical states. Competent grasping and manipulation, in this concept, is simplified by using a sequence of mechanical interactions with the environment, prior to attaining a grasp. The main intention of these interaction patterns is to increase the predictability of subsequent actions.

An example for the type of grasping strategy we envision is the push-grasp strategy proposed by Dogar and Srinivasa [27], and which is also shown in Figure 8.1 for the RBO Hand 1. In this strategy, the robot sweeps an open gripper across a surface before attempting the grasp action. If the object is positioned within a certain, contiguous region in front of the hand, the strategy will succeed with high probability. The important thing is, that the region of object positions that leads to success is considerably larger before the sweep than before the grasp action, making the grasp strategy applicable to more situations, but also less reliant on prior perception of object position. This idea of using uncertainty-reducing actions to complement "regular" actions is not new. Mason proposed planning with compliant motion using "pre-images" [65], "funnel" actions [75, 73], and sensorless action sequences [34].

The Grasp as Adaptation of Hand to Object Shape If a hand attains a grasp with a large number of contacts, or even a large contact area, then the surface of the hand will necessarily match the object shape. We can therefore see the capability of a hand to assume the shape of the object to grasp as a necessary (albeit not sufficient) condition. The hand needs to adapt its shape to the object. Traditionally, robot systems match the object shape by perceiving the object visually, computing a hand posture, and then enacting it. But there are also hand

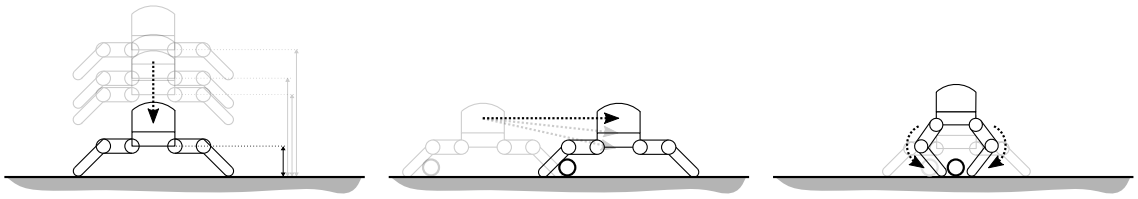

(a) Position or orient relative to each other

(b) Move in subspace

(c) Reduce uncertainty by acting

Fig. 6.1 Three different schema for exploiting contact with the environment. Light gray drawings illustrate possible scene variations, which are collapsed into a single configuration after the action. Images taken from Deimel and Brock [24] ©Springer-Verlag 2015

morphologies that directly implement shape adaptability, most notably underactuated hands and grippers [2, 83, 13, 112].

Positioning by Colliding The first interaction we consider is to collide with a surface (see Figure 6.1a). The collision path can e.g. be guided by visual servoing. This interaction removes the uncertainty about the distance between the two colliding objects. To be able to implement this interaction easily, the hand must limit impact forces and be able to react to disturbances quickly.

In a special case, the object to grasp itself provides the constraining surface. Compliant actuation of each joint then makes it easy to establish many contact points on the object and to balance contact forces to achieve a grasp [2, 30, 21, 22].

Moving in Spatial Subspaces The second interaction we consider is to slide fingers and object along a surface and is shown in Figure 6.1b. This interaction fixates motion along the surface normal and rotation out of plane, which in turn simplifies the control of finger position and hence object position. For most reliable execution, the fingers should always stay in contact with the constraint during the sliding motion.

Reducing Uncertainty by Acting The third interaction we consider is to close a cage around an object that was previously formed with the hand and a surface (see Figure 6.1c). Sliding continuously moves the contact between surface and fingertip. This shrinks the cage which an enclosed object cannot escape and effectively removes the uncertainty about object location. For maintaining the cage, the fingers should continuously stay in contact with the surface. Additionally, the cage can also reject disturbances that may be introduced by concurrent manipulation, such rotating the object with the hand. This makes caging a very useful interaction in a grasping strategy.

In addition to the proposed interaction pattern categories, grasping strategies may also include intermittent servoing to be able to concatenate interactions. Servoing should be used sparingly though, as those steps introduce new uncertainty and therefore lower the reliability of the overall sequence of actions.

6.4 Hardware Requirements for Soft Manipulation

Constraint based motion – which was explained in the previous section – can be used to remove perceptual uncertainties and reject disturbances that we anticipate from our planned actions. In the best case, this results in a fixed sequence of interactions that yields a predictable outcome in many situations. While better perception reduces uncertainty about the state of the world too, using constraints also simplifies planning. A planner that constructs these strategies will greatly benefit from a large and diverse set of interactions to choose from, therefore manipulator hardware should facilitate as many different interactions as possible. Additionally, this approach frees up perceptual resources for other tasks. From this problem description, we can extract a set of goals for hand design:

Low Inertia Movable parts of the robot should exhibit a low apparent inertia. It enables reaction to fast changes in contact location and limits the energy transferred upon impact. The former makes it easy to maintain contact, while the latter limits the increase of uncertainty to position and orientation of the contacted object.

No Reaction Delay Actuation should provide a very low time delay for reactive motion to stay compliant during fast disturbances. This requirement is especially difficult to achieve when actively controlling compliance, e.g. with geared electric motors.

Robustness to Arbitrary Collisions The hardware has to be robust against arbitrary collisions. The robot needs to contact objects of unknown shape and position frequently, and quickly without having full or accurate knowledge of the world. Errors will happen, and therefore unexpected collisions will occur. A suitable hardware will tolerate these collisions and not break. Robustness can e.g. be accomplished by providing compliance in every direction and about many rotation axes.

Safe for the Environment To a lesser extent, it is also desirable for the manipulator to generally not break or damage objects. If safety to the environment can be ensured by passive, mechanical means, more actions can be tried without risking catastrophic damage. This

requirement also facilitates autonomous learning and workspaces shared between humans and robots.

We want our pneumatic soft hands to excel on all of those requirements. Their instantaneously reacting mechanical compliance makes it easy to create and maintain contact. Their large number of mechanical degrees of freedom imply the propensity for many contact points. Most degrees of freedom are controlled by a fixed coupling, which can be adjusted to heuristically balance forces during grasping.

6.5 Conclusion

In this chapter, we took a step back and looked at how soft hands fit into the larger picture of a robot doing grasping not by planning trajectories and contact points, but by compliantly interacting with its environment. We constructed and elaborated on the *Soft Manipulation* paradigm. To explain and design grasping strategies, we proposed the concept of *exploiting the environmental constraints* to motion. We further argued, that soft hands should provide four properties that are highly desirable for learning those grasping strategies and executing them reliably: Low inertia, zero reaction delay, robustness to collisions, and safety for the robot's environment.

Soft Manipulation also poses new challenges for all components of a robot system. It drops the classical separation between hand hardware and control created by the concept of enumerable, well defined contact points. It remains to be seen whether or not there exists an equally powerful concept that factorizes grasping into separate tasks for hand hardware and control as well. For now, we need to assume that control and hand morphology are intricately intertwined, and cannot be treated separately under this paradigm.

Chapter 7

Soft Hands

In this chapter we introduce and describe the RBO Hand 1 and RBO Hand 2, which are two robotic manipulators built with the PneuFlex toolkit described in the first part of the thesis. We also analyze related grippers and hands for whether we can use them as soft hands too.

7.1 Related Work

In this section, we will have a look at robotic grippers and hands that incorporate softness and compliance in various ways. This overview will serve as a context for the subsequent description of the pneumatic soft hands RBO Hand 1 and RBO Hand 2.

Over the years, robotic end effectors developed into two distinct branches: simple grippers that provide robust grasp capability on a very limited number of object shapes (e.g. box shapes), and hands that provide as much actuation and and controllability as possible. The latter often are anthropomorphic, and aim to fully control few contact points located at the fingertips for precision grasps. Robotic hands are often used in grasping research, to avoid being limited by the hardware. Grippers, on the other hand, are more popular in research where grasping is not the central topic and manipulators "have to work", but where it is feasible to make the grasping task very specific. Especially with the latter category, there has always been an ad-hoc use of soft materials and structures. Often it is as simple as adding a rubber or foam pads, while other designs add compliance through structural deformation [47, 2, 39] or by adding passive or underactuated joints [96, 30, 14]. Fully actuated hands, e.g. the Allegro hand [3], the Awiwi hand [45] or the Shadow hand and TUM hand [98] incorporate compliance too, but in a different way. They can actively create compliant motion via admittance or impedance control [3, 45, 98]. Their compliance capabilities are necessarily limited to the actively controlled joint axes, though. All other motions are suppressed as much as possible to avoid instability of control, and therefore those hands usually have very stiff links.

Albeit both approaches are very different, soft hands can (and should) incorporate ideas from both areas. Compliant and underactuated grippers provide us with templates for how to implement desired behaviors without delegating the complexity to control, while fully actuated hands offer versatility for prototyping coupling patterns, which can later be translated into the morphology for a soft hand. Actually, these two distinct aspects already began to merge with the development of underactuated and compliant hands: manipulators that provide a low, easy to command number of actuation signals similar to parallel jaw grippers, but also have morphologies that create behaviors as complex as those of fully actuated robotic hands, such as the Pisa/IIT SoftHand [9] or the ISR hand [110].

Overall, there are far more robotic hands and gripper designs than could possibly be covered here. An excellent overview on influential robotic hands of the last decades is given in Controzzi, Cipriani, and Carozza [17]. With respect to soft grippers and hands a recent literature study [53] provides an extensive overview on methods and technologies for building soft robots. In this chapter, we focus our analysis on hands and grippers that were specifically developed in the context of grasping research and which include some form

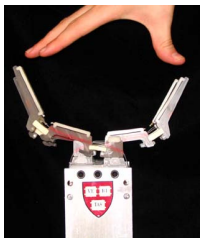

(a) SDM-Hand, from Dollar and Howe [29] ©2008 IEEE

(b) Positive Pressure Gripper, from Amend et al. [2] ©2012 IEEE

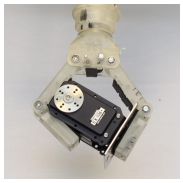

(c) Optimized single-tendon gripper, from Ciocarlie, Mier Hicks, and Stanford [12] ©2013 IEEE

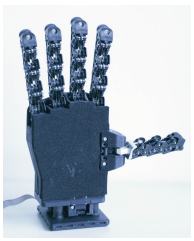

(d) Pisa/IIT SoftHand

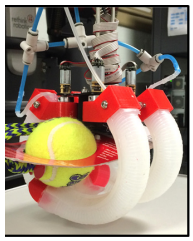

(e) SPA-based gripper, from Morrow et al. [78] ©2016 IEEE

Fig. 7.1 Selection of grippers of hands that can use softness and compliance in their design.

of passive compliance into their design intentionally. We will analyze the related work in their use of mechanical compliance, compliance provided by control, and design choices that pertain to making grasping strategies more robust and reliable to execute.

7.1.1 Passively Compliant and Underactuated Hands and Grippers

Passively compliant and underactuated hands and grippers distinguish themselves by having a moderately high number of mechanical degrees of freedom, but only a small number of degrees of actuation or even just one. The difference between degrees of freedom and degrees of actuation is usually created by either using passive compliance or underactuation. Based on those two approaches Grioli et al. [46] proposes a categorization into hands that implement “rigid synergies” (no compliance), “soft synergies” (independently compliant degrees of freedom), “adaptive underactuation” (uncontrolled null space motion) and “adaptive synergies” (compliant null space motion). Many recently developed hands fall into the latter two categories.

iHY and SDM hand The SDM hand was developed based on a rapid prototyping process called Shape Deposition Manufacturing [30] (hence its name), which adds materials by printing or casting, and subtracts materials by milling. Done iteratively it enables the semiautomated creation of structures composed of multiple materials. The original design [29, 30] spawned several variations, most notably the iRobot-Harvard-Yale (iHY) hand [83], a two-fingered gripper [84], and several other gripper designs which were open-sourced by

the OpenHand Project [1] which includes the Yale OpenHand [67]. All hands share the same basic finger morphology of the SDM hand, except for the first joint. The iHY hand and Yale Open Hand replace the joint's rubber flexure with a hinge to increase torsional stiffness.

The design of the SDM Hand embraced compliance and coupling as a central design objective [30]. Mechanical coupling through a tendon-pulley system balances grasping forces between all fingers. Non-actuated but compliant degrees of freedom are provided by the elastomer joints, which improves the hand's capability to align link surfaces to the object's surface to provide a larger contact surface. The SDM hand shows a considerable dexterity with respect to the object shapes it can grasp [30], and was also demonstrated to tolerate errors in pre-grasp object locations, caused by limited perception. Both are considered important, desirable properties of soft hands. In the iHY hand, the joint coupling is further refined to provide a distal link that has no mechanical compliance in the direction of the surface normal [83]. This enables the hand to project large contact forces. The iHY hand was also used to demonstrate in-hand manipulation [82] even though the hand is highly underactuated. Similarly, the two-fingered version was used to demonstrate a complex grasping strategy named "flip-and-pinch" grasp [68], where a coin is picked up in a two-step pre-grasp manipulation process which only requires a very simple wrist and finger motion to execute.

Overall, the SDM hand and its offspring incorporate many morphology details that also are useful for a soft hand, and are a valuable example for the potential of underactuated mechanisms. They don't provide a large number of degrees of freedom and the ability to maintain many redundant contacts though, which contrasts them to our pneumatic soft hands.

Velo Gripper The Velo gripper is a two-fingered gripper whose joint coupling was optimized to perform well on certain shape primitives (elliptical prism, rectangular prism) with variations in size, representing the occurrence of those parameters in common household objects. [12]. Even though the gripper only sports four degrees of freedom, it is a good example of how the right morphology – in this case the tendon routing that determines the balance of joint forces – can greatly improve grasp reliability when object shape and orientation are uncertain. At the same time it also leverages the task-specificity: the gripper was not optimized on all possible objects, but on the most common ones, enabling to trade off success rate on rare objects against the success rate on common objects.

Pisa/IIT SoftHand The Pisa/IIT SoftHand [9] is shown in Figure 7.1. It was developed based on the "grasp posture synergy" hypothesis [100, 99], which posits that grasp posture

[1] https://www.eng.yale.edu/grablab/openhand/

can be expressed in large part by a linear combination of all joint angles. A relatively small number of such co-actuation patterns ("synergies") can recreate most of the hand motion. Additionally, its anthropomorphic shape and behavior makes the hand intuitive to teleoperate by humans. The Pisa/IIT SoftHand implements the coupling of the most pronounced synergy with a single motor, which projects its motion on a total of 19 underactuated joints. In order to adjust the posture to the actual object, the joints can move freely in the null space of the actuated degree of freedom. Motion is subject to considerable friction caused by the tendon routing, though. A recent iteration of the hand design though, exploits this tendon friction by adding a second motor to the opposite end of the tendon [101]. The direction of accumulating friction forces along the tendon then differentiates the hand motion between both motors. This effect was then used to adjust grasp posture during a grasp, enabling coordinated finger motion patterns with a very low number of motors. For soft hands, this shows that mechanical complexity (in this case tendon stiction/friction) can be used advantageously to keep control of complex motions simple.

Another unique feature of the hand is that its joints can temporarily dislocate which enable the fingers to bend in almost any direction. This makes the hand robust against collisions when the tendon is not tensioned. The hand usually is covered with a rubberized work glove to protect the joint mechanics, and to improve the surface friction.

Overall, we can consider the Pisa/IIT SoftHand to be a soft hand, as it provides a large number of degrees of freedom. It also incorporates a refined coupling between joints to provide a reliable grasp motion.

UC Softhand The UC Softhand [112] is an anthropomorphic hand which uses tendon-driven flexural joints similar to the SDM hand. The fingers incorporate finger pulp by adding foam padding to the actuator. This enables the finger to adapt to edges and groves of objects. The authors explicitly note the advantage to grasping: "The novel fabrication method of the fingers allowed for the integration of a compliant skin all over the fingers, which resulted in improved grasping and more anthropomorphic look compared to the previous version." The hand is driven with three motors, and a backdrivable transmission system, which enables active compliance. The hand provides some limited passive compliance in the joints due to being flexural, which is exploited in the example grasps [112]. Coupling is limited to the joints within each finger.

The UC hand incorporates some of the features we desire for soft hands, e.g. it provides underactuation and a soft, adaptive surface.

FESTO FinGripper The FESTO FinGripper [47] is a gripper with three fingers arranged symmetrically around a circular palm. The special feature of the fingers is, that they are completely passive except for one rotary joint at the finger base. Instead, they feature a large number for four-bar-linkages, which couple the motion of each segment to the global motion in a specific pattern. The result is a finger that can "wrap" around an object by itself when being pushed against it. This makes control of the hand simple, as we only need to command a single joint rotation.

The FinGripper demonstrates, that a complex morphology can greatly simplify the control effort. Instead of directly controlling tens of joints individually, control only needs to command a single degree of actuation for a successful grasp.

Positive Pressure Gripper The Positive Pressure Gripper [2] design consists of a simple rubber balloon filled with ground coffee. Its phase can be altered from fluid to solid by evacuating the balloon. When fluid, the gripper can match the shape of even relatively small or thin objects, such as coins, screws and pens. After evacuation, the contact stiffens and contact points are effectively created on the whole surface of the object.

The gripper offers a unique approach to the concept of a gripper, and probably represents the most committed example of using softness and compliance in grippers to date. The gripper itself is limited to a single grasping strategy though, as it needs an opposing surface to press the object against, e.g. it cannot grasp free-standing objects from the side.

Soft Gripper Based on Electroadhesion Dielectric Elastomer Actuation An altogether different approach to grasping is taken by Shintake, who developed a completely soft gripper based on a dielectric elastomeric actuator [106]. The gripper has two sheets that act as fingers. Each sheet is composed of layers of conductive and insulating silicone. The layers are structured so that the sheets can be bent using the electrostriction effect. Additionally, the gripper exploits the electroadhesion effect and provides a controllable adhesive force when contacting an object. This enables the gripper to obtain a grasp even with very compliant fingers. Unfortunately though, the attained electroadhesion strength still requires $13\,\mathrm{cm}^2$ of contact surface to achieve 1 N contact force, and the force scales only with the surface area (vs. object weight that scales with volume). This restricts the technology to rather small scales or lightweight objects. The technology could be integrated with fluidic soft continuum actuators to boost contact strength though, as the sheets are completely soft.

7.1.2 Soft Pneumatic Actuator Based Hands

Starfish Shaped Gripper The starfish shaped gripper [54] is made entirely out of silicone. Its simple symmetric design, similar to a starfish has six highly flexible fingers. This allows the gripper to comply well to an object surface. The starfish gripper is based on PneuNet actuators, which use the same actuation principle as the PneuFlex actuators, but operate at about 5-10 times lower stiffness, making the gripper much weaker.

SPA-based Hand Recently, a four-fingered hand with actuators similar to the RBO Hand 1 has been developed by Morrow et al. [78]. Pairs of fingers oppose each other, and each of the fingers also has a hard fingertip to improve the ability to slip under objects during a surface-constrained grasp (top grasp) strategy. Additionally, they instrumented the finger with bending sensors to provide closed-loop position control.

The researchers demonstrate that the pervasive compliance of the fingers can be used beneficially during grasping to conform to the object. With their investigation into fingertip shapes they also provide evidence that spatially small changes to morphology can have a great effect on grasp reliability.

fPN Based Hand and Gripper A design similar to the SPA based hand was also investigated by Galloway et al. [42]. The hand is based on fPN actuators, augmented with foam pads on the hand inside. The design also has four fingers, but opposing fingers are not aligned, so they don't collide during bending. The authors provide an evaluation of the gripper in an underwater teleoperation application (coral sampling on an ocean floor) to demonstrate that fluidic soft continuum actuators can be used in harsh environments, as they do not have moving parts and need not be sealed. The authors also investigated the use of "boa" fingers, which wrap around a cylindrical object to provide a much stronger grip, and reverberates the seminal soft gripper design by Hirose and Umetani [50]. The grasp strategy for this boa finger also relies heavily on the ability of the finger to adapt to the object shape.

Homberg et al. used a variation of fPN actuators, for the construction of a three-fingered gripper [52] which they sensorized for haptic feedback.

7.2 RBO Hand 1

In this section we describe the morphology of the RBO Hand 1. The hand is shown in Figure 7.2 and was the first functional soft hand built from PneuFlex actuators [21]. The hand is made up of two distinct parts: the fingers and a palmar plate opposing them.

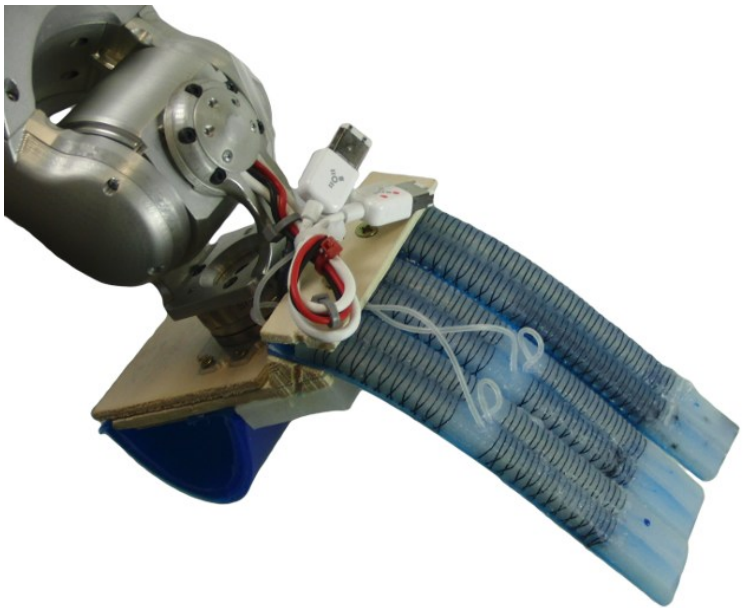

(a) RBO Hand 1

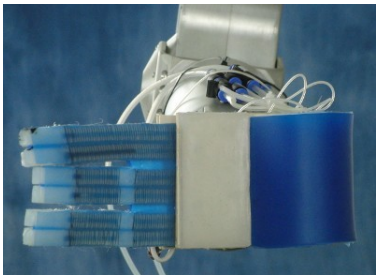

(b) Front view

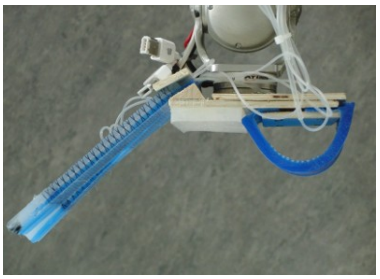

(c) Side view

Fig. 7.2 Image of the RBO Hand 1, which was the first functional soft hand based on PneuFlex actuators.

Fingers The hand employs three fingers, with each one made from a pair of PneuFlex actuators. The exact number of digits was not considered important and was chosen based on the number of digit of other grippers designs (e.g. Barret WAM hand, SDM gripper [29]). Figure 7.3 shows actuator version *P5*, which was used to build the RBO Hand 1. This actuator version is 120 mm long, has a height and width of 9 mm, and a hull thickness of 3 mm. The resulting actuator can be inflated up to 250 kPa, but is relatively weak due to its low height. The actuator is about 5 times more compliant than the actuators later used for the RBO Hand 2. Different to later actuator versions, the helical thread was wound before the

(a) Single actuator

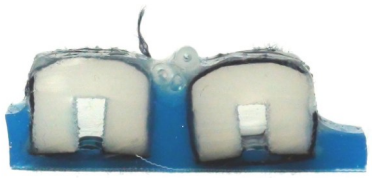

(b) Cross cut of a finger

Fig. 7.3 Actuator version P5, used in pairs for the fingers of RBO Hand 1. Images taken from Deimel and Brock [21] ©2013 IEEE

bottom, passive layer was bonded. This makes it easy to place several actuators on a common sheet of mesh, as it was done with the RBO Hand 1. The three fingers are connected to each other by a mesh up to about half their length, which can be seen in Figure 7.2b. This was done to increase the otherwise very low torsional stiffness of the fingers. Additionally, the air chambers of two fingers were split at 70 mm length, to provide the option to test different actuation patterns.

The fingers are mounted to a palmar plate with a clamp. While this offers a simple method to attach and detach fingers, the fingers are also prone to slip out of the clamps eventually. This method of assembly is by now superseded by the one documented in Section 3.6.2.

Palmar Plate The second distinct part of the RBO Hand 1 is the palmar plate which is used to both mount the fingers onto a robot arm, but which also provides a palm-like surface for the fingers to grasp against. This is a distinct feature with respect to many other gripper designs, which usually provide opposing fingers instead. The plate itself is covered with silicone rubber to improve friction and avoid exposure of a hard surface.

Due to the shape of the plate, the fingers were placed in parallel to attain a cylindrical shape when closing. Additionally, the fingers are mounted at a 30° angle to the plate, to support implementation of a push grasp [27], and pre-grasp caging of objects. The angle is low enough so that the gripper can still conform to a flat surface by bending the fingers backwards.

Palm Sheet The prominent feature of the palmar plate is the ”palm sheet“ though. Our intention here was to mimic the palmar pulp found in human hands, which together with the tough skin provides a surface that conforms well to object surfaces when pressed against them. The palm sheet consists of a $100\,mm \times 80\,mm \times 5\,mm$ sheet of silicone rubber ($E \approx 600kPa$). Two strips of fabric were embedded on either of the long end to be able to clamp them to the palmar plate. The strips are oriented orthogonal to the sheet's plane, this causes the sheet to bend by about 180° when it is mounted on the palmar plate. The resulting shape can best be seen in Figure 7.2c.

Even though it is not filled with gel, fluid or granular material, pre-tensioning the rubber by bending creates a similar effect. At the same time, this structure is light weight and very easy to manufacture. In contrast to fingers, this structure does not actively bend, but it provides a large contact area which helps to counter rotational forces that are applied to a grasped object.

Actuation To inflate and deflate the actuators, each chamber was connected with thin silicone tubes (1.5 mm outer diameter, 0.5 mm inner diameter) after manufacturing by inserting them with a 2 mm cannula, a technique adopted from Ilievski et al. [54]. From the perspective of control, this method is problematic, as it restricts the maximum possible cross section available to move air. This severely limits attainable flow rate, which scales to the fourth power of tube diameter according to the Hagen–Poiseuille equation [86]. The actuators of the RBO Hand 1 have a tiny chamber volume though (1.6 cm^3), which partially alleviates the problem. Actuators that are parallel to each other were directly connected with each other with a tube. Otherwise, tubes were routed to the palmar plate and connected there with Y-fittings to obtain different control setups. The most common setup connected all actuators together to form a single control channel. An alternative setup is to connect the distal chambers of the two segmented fingers separately, to e.g. provide a pincer-grasp like motion pattern.

7.3 The RBO Hand 2

In this section, we describe the morphology of the RBO Hand 2, which is shown in Figure 7.4 and 7.5. The RBO Hand 2 is an anthropomorphic soft hand and its shape was chosen for several reasons. First, objects in human environments are designed for the manipulation with human hands. Therefore, by using hand of size and shape similar to the human hand we can leverage this advantage. Second, the human hand shape enables many different forms of grasping, when considering that there are ”seven billion different hands“ [45] which are all slightly different, using a humanoid hand shape as template is a design choice worth investigating. Third, the anthropomorphic shape enables us to more directly compare the capabilities of the RBO Hand 2 with the capabilities of humans [23, 32]. It also enables us to apply well-established human grasp taxonomies to our hand for comparative studies. Another possible advantage of a humanoid hand may be the more intuitive transfer of grasping strategies observed with humans to robotic systems.

In the following paragraphs, we elaborate on the design of the main parts of the RBO Hand 2, which are the four fingers, the palm and thumb, and the ”scaffold“ that arranges the actuators.

The complete set of printable CAD models necessary to build an RBO Hand 2 are published [19], to facilitate replication of the RBO Hand 2.

Fingers The five fingers of the RBO Hand 2 are single PneuFlex actuators. The index, middle, ring, and little finger are 90 mm long and of identical shape (named `P10.finger`),

Fig. 7.4 The RBO Hand 2, an anthropomorphic soft hand. Images taken from Deimel and Brock [24].

Fig. 7.5 Different views of the RBO Hand 2. Images taken from Deimel and Brock [21].

name of shape	P10.finger	P10.thumb	P10.PalmInner	P10.PalmOuter
base curve	straight	straight	circular, r=37.5 mm	circular, r=62.5 mm
max. height, width	20 mm	25 mm	25 mm	25 mm
length	90 mm	70 mm	90°	90°
rubber thickness	2 mm	3.46 mm	3.46 mm	5.76 mm

Table 7.1 Main parameters of the four different PneuFlex actuator shapes used in the RBO Hand 2.

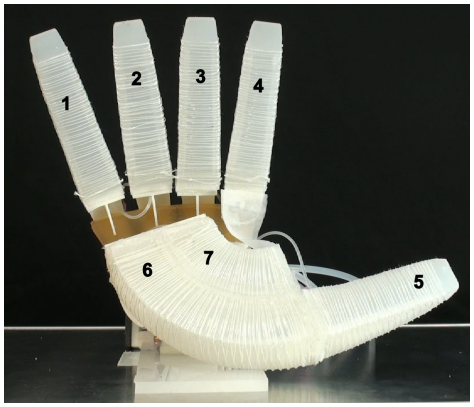

Fig. 7.6 The RBO Hand 2 consists of seven individual PneuFlex actuators, mounted on a scaffold.

while the thumb actuator (P10.thumb) has the same shape but is slightly thicker and shorter. The thumb is not directly connected to the scaffold, but attached via the palm actuators. The main shape parameters for all actuators are listed in Table 7.1.

The fingers of the RBO Hand 2 were the first ones were we applied the design rules of Section 3.4 to intentionally shape the mechanical parameters along the finger. The actuation ratio along the finger (actuation ratio profile) is constant, whereas the stiffness along the finger (stiffness profile) drops linearly from maximum stiffness at the base to reaching zero stiffness at the tip. Such a stiffness profile has also been used in the soft gripper design [50].

This results in an actuator circumference following $c(x) = \sqrt[3]{\frac{x}{x_{tip}}}$, where x is the distance from the actuator base along the actuator and x_{tip} is the finger length. The width of the actuator follows the profile $w(x) = h_{max} \cdot \sqrt[8]{1 - 0.925 \cdot \frac{x}{x_{tip}}}$ instead of $w(x) = h(x)$ to give the finger a broader tip. It also makes fingers visually more appealing as they are less pointy.

Palm A key feature of the human hand is the opposable thumb. Unfortunately, directly implementing the kinematics of the thumb's carpometacarpal joint which makes the thumb opposable is not possible with PneuFlex actuators. Continuum actuators can only bend gradually, extreme curvature can therefore only be attained by trading off either strength or wear, as elaborated in Section 3.3.3. Therefore, instead of imitating the skeletal motion, we

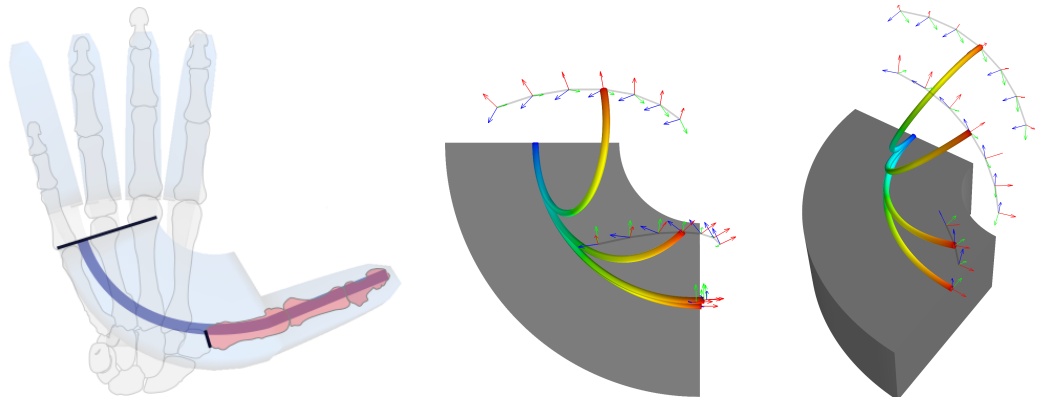

(a) RBO Hand 2 thumb vs. human thumb kinematics

(b) Top view

(c) Isometric view

Fig. 7.7 Concept study of the opposable thumb. Figure (a) illustrates the difference to a humanoid hand in terms of how the thumb is attached to the wrist. Figures (b) and (c) indicate the attainable locations of the thumb's base frame. The effect of inflating both actuators equally is visualized by the colored beams, while the gray lines indicate the motion possible by differential inflation.

imitate the deformation of the hand inside. The thumb is connected to palm actuators which are not mounted at the wrist, but at the location where usually the metacarpophalangeal joints of the fingers (i.e. the knuckles) are located. From there, we mimic the gradual bending of the hand inside using two PneuFlex actuators. The resulting compound of three actuators can best be seen in Figure 7.6, as in this illustration the palmar sheet is removed. We realize the palm with two special, curved actuators, `P10.PalmInner` and `P10.Palmouter`; Table 7.1 lists their parameters. The actuators are curved perpendicular to the passive layer, leveraging the capabilities of the PneuFlex design. Their radii are chosen such that there's a 5 mm gap between both actuators, allowing them to deform freely when being inflated. The gap is also used to route a tube from the scaffold to the thumb for actuation. The stiffness as well as the actuation ratio remain constant along the curved actuator. The palm's actuators are designed to be twice as stiff as the fingers to account for the fact that two palm actuators oppose four fingers. This is done by increasing the height (and width) of the actuator by just 5 mm to 25 mm. Furthermore, the actuation ratio between inner and outer actuator is chosen such that inflation with the same pressure yields a curvature proportional to the inverse of the radius of the base curve of the actuator. This results in the palm assuming the shape of a segment of a cone. By inflating the two actuators with a pressure difference, we can impose a twist along the palm actuators. The effect on the orientation and position of the thumb is illustrated in Figure 7.7. Related to this, Figure 8.8 in Section 8.2.1 shows the motions the actual hand is capable of.

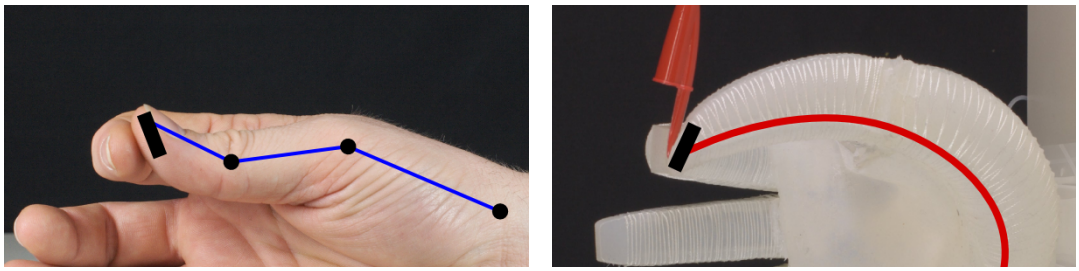

(a) Human thumb during a pincer grasp (b) RBO Hand 2 thumb during a pincer grasp

Fig. 7.8 Difference in thumb configuration and fingertip use during a pincer grasp between a human hand and the robotic hand

Augmenting the actuators, the palm also features a sheet of silicone with an embedded mesh. This sheet covers the gap between the fingers and the palm and stabilizes the flexible scaffold the actuators are mounted on, especially during power grasps and heavy loads, as shown in Fig. 7.10. But it is also intentionally bulged to mimic palmar pulp to improve contact with objects, much like it we did in the RBO Hand 1.

Mounted on the end of the outer palm actuator is the thumb actuator.

Thumb Another difficulty in the design of the RBO Hand 2 was the range of motion of the thumb. A faithful imitation of how humans use their thumb would require a negative curvature close to the tip, to tilt the surface of the thumb tip for correct opposition for a pincer grasp. Figure 7.8a shows an example of a human hand. While it is possible in principle to build a backwards-curved actuator, it would significantly increase complexity of manufacturing the thumb. We therefore deviate here from the human hand too. Instead of the inside of the thumb, we use the backside (dorsal side) as the primary contact surface for pincer grasps. This reassignment effectively changes the orientation of the contact surface by about 45–60°, relative to the orientation found in a human thumb. This avoids the need for a negative curvature of the passive layer which is inconvenient to manufacture.

Scaffold The ”scaffold“ of the RBO Hand 2 refers to the plastic structure holding the actuators in place. It consists of five struts that attach one actuator each to a common wrist plate, similar to the metacarpal bones in a human hand. Different to bones, though, these struts are flexible by design.

The scaffold is shown in Figure 7.9. Is printed with polyamide using selective laser sintering. The individual struts (2 mm thick, see Fig. 7.9) have a flat cross section, which facilitates bending along one axis. This results in a spreading of the fingers when the hand is

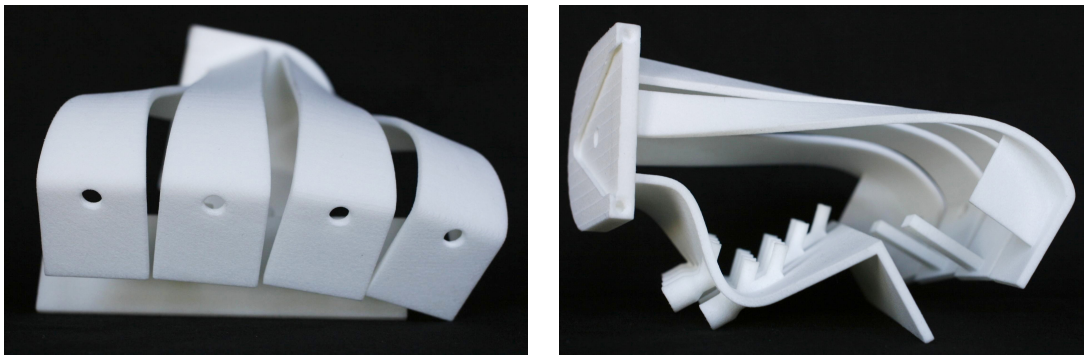

(a) (b)

Fig. 7.9 Polyamide scaffold of the RBO Hand 2. Images taken from [24]

loaded as shown in Figure 7.10a. The struts decouple displacement between fingers, which increases the passive compliance of the hand. The flexibility of the struts limits impact forces too, while providing sufficient stiffness for heavy payloads without excessive deformation (see Fig. 7.10). The fingers and the palmar actuator compound are bonded to the supporting scaffold using the method described in Section 3.6.2. The palm is supported by parts of its strut to increase its stability under heavy load.

The entire hand weighs 178 g and can carry a payload of up to 0.5 kg. The RBO Hand 2 was designed with maximum compliance in mind, though, so this is not the limit for soft hands in general. Higher payload can e.g. easily be achieved by increasing finger stiffness.

7.3.1 Grasp Strength

While grasp quality and grasp strength was not the driving design criterion for the hand, it is important to verify that a compliant hand is capable of lifting objects of reasonable weight. To give the reader an intuition on the capabilities of the hand, we provide a few tests regarding grasping forces.

The heaviest objects used in the Feix taxonomy grasps were the rectangular plate in grasp 22 (156 g), the metal disc in grasp 10 (181 g), the wooden ball in grasp 26 (183 g), and the circular plate in grasp 30 (240 g). Note that in grasps 26 and 30, the shown posture offers the least structural support of possible hand poses. Fig. 7.10 shows two additional heavy objects, a wooden cylinder (541 g) and a lead ball (1.650 g). Fig. 7.10 also shows three different directional disturbance forces on a cylinder which is power-grasped with grasp 1. If forces above 6-8 N are applied, the cylinder will slide in the hand.

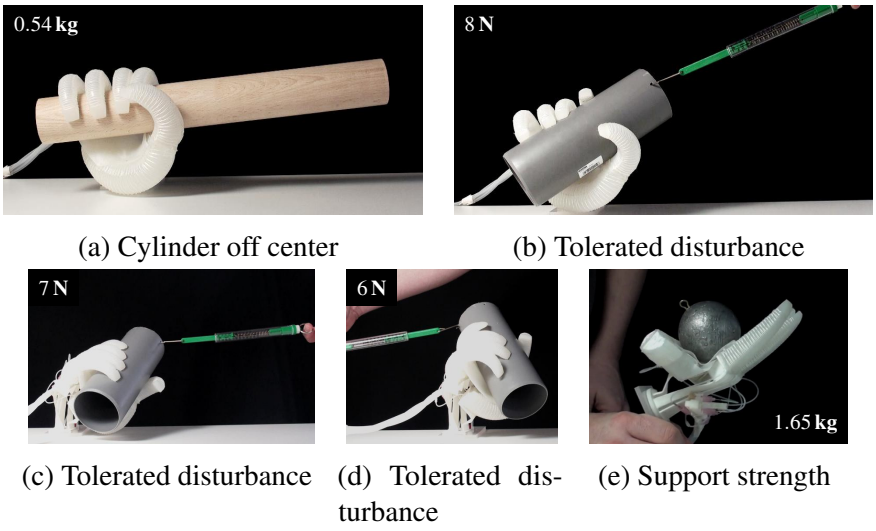

(a) Cylinder off center (b) Tolerated disturbance

(c) Tolerated disturbance (d) Tolerated disturbance (e) Support strength

Fig. 7.10 Illustrations of grasping force capabilities: (a) finger strength and palm support strength, (b)–(d) tolerated disturbance forces in different directions, and (e) strength provided by the scaffold

7.4 Conclusion

This chapter gave an overview on robotic manipulators and hands that incorporate softness in various ways to improve grasping capabilities. It also documented in detail two hand artifacts that were built with PneuFlex actuators. The RBO Hand 1 provided a proof-of-concept for the actuator technology, while the subsequent RBO Hand 2 leveraged capabilities specific to the PneuFlex toolkit from Chapter 3, such as curved actuators, or actuators with designed actuation ratios and non-constant stiffness profiles. Issues with excessive softness in the RBO Hand 1 where also addressed in subsequent hands in order to provide a more useful payload weight limit. The RBO Hand 2 further demonstrated a new thumb kinematic suitable for continuum actuators without requiring discrete joints for the thumb's base. The design files (scaffold and mold models) for building an RBO Hand 2 are published [19] to facilitate replication and reuse in future research.

Chapter 8

Shape Adaptability and Grasp Posture Dexterity of Soft Hands

In this chapter we present experiments with pneumatic soft hands that corroborate the importance of softness and compliance for robust grasping. We also demonstrate that soft hands can provide diverse grasp postures with only limited control.

8.1 Shape Adaptability

We intend soft hands to simplify higher level control and planning, and one crucial task during grasping is to establish force closure between hand and object. An almost trivial, but important observation is, that adding more contact points between hand and object either improves force closure, or adds redundancy to the force transmission, making the grasp overall more robust. At the very least, we can expect that additional contact points do not decrease the grasp quality. This expectation may still be jeopardized sometimes by introducing a new, particularly unfavorable coupling of contact forces. So it is not a direct, deterministic relationship. To summarize, having as many contact points as possible seems to be a plausible heuristic for ensuring a grasp. The number of contact points a typical robot hand can create is usually limited to one or two per link, though. Overall, the number of contact points is limited in two ways: by the number of available rigid links, and the reachability of the object surface for each link.

The former limitation is lifted by soft hands by providing many degrees of freedom. Probably the most extreme example is the positive pressure gripper [2], which is a rubber balloon filled with small granular material (e.g. ground coffee) and which can be evacuated to become stiff. Each small surface patch can rotate and move almost independently of its neighboring patches, creating a large number of contacts. PneuFlex actuators are less shape-adaptable, but due to their softness still provide a large effective number of degrees of freedom. But also the SDM hand [30] already provide 27 degrees of freedom (3 rotations per joint) by using flexure joints made of rubber. The same is true for the Pisa/IIT SoftHand, which has 19 dislocatable joints, providing at least 19 and up to 57 degrees of freedom.

The second potential limitation is that a hand does have many links, but most of them may never be able to contact the object in the first place. The capability of a hand to have many links and to put many or most of them in contact with the object is captured in the term *shape adaptability*. The term stems from the observation that during successful grasps, the hand surface of soft hands often matches the object surface well. Shape adaptability is very much related to the concept of power grasps, which distinguish themselves from precision grasp by having many, large, and areal contact patches.

Of course, shape adaptability is not the only property required from a good soft hand. It has to be balanced against the goal of grasp strength to yield a hand that is both strong enough to actually transmit forces, and compliant enough to adapt to the object shape. Fortunately though, for tasks in human-centered environments there seems to be a sweet spot. Statistics on human manipulation activities show that most manipulated objects weigh less than 1 kg [118], and several prior grippers demonstrated extensive shape adaptability while being able to cover this range of payload weight. [30, 2, 9].

(a) Front view (b) Top view

Fig. 8.1 Experimental setup: RBO Hand 1 is mounted as an end effector on a Meka robot to execute the strategies. Objects are placed on a table in front of the robot. In (b) the robot attempts a push-grasp on a cylinder. Images taken from Deimel and Brock [21] ©2013 IEEE

(a) Test objects for push grasp (b) Test objects for surface-constrained grasp

Fig. 8.2 Test objects for each grasp strategy. Images taken from Deimel and Brock [21] ©2013 IEEE

8.1.1 Implementation of Shape Adaptability in the RBO Hand 1

The RBO Hand 1 is shown in Figure 7.2 and 8.1 and is explained in detail in Section 7.2. It was the first functional soft hand built from PneuFlex actuators [21]. Shape adaptability was the main driving design goal of this hand, and it was maximized in several ways. Each finger is made from a pair of especially compliant PneuFlex actuators. Each finger is made of two parallel actuators, which creates a broader finger and therefore a larger contact area.

A second structure that improves shape adaptability is the bent palm sheet, which can be seen in Figure 7.2c. The sheet can deform upon contact with an object, and it can also conform to an object and a table surface at the same time.

8.1.2 Testing the RBO Hand 1 on Grasping Complex Object Shapes

To demonstrate shape adaptability the RBO Hand 1 should be capable to grasp objects with different and irregular shapes. Shape adaptability also implies that the hand can adapt to

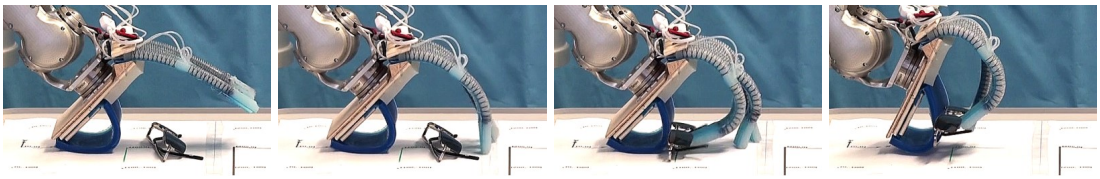

Fig. 8.3 The surface-constrained grasp approaches the object from the top and first collides the palm with the table. Subsequently the finger are inflated to cage the object. The grasp motion is completed by rolling the hand around the palm-table contact, letting the finger slide towards the caged object. Images taken from Deimel and Brock [21] ©2013 IEEE

deformable objects that change their shape during interaction, e.g. a bag or ballon. The latter type of object is especially interesting, as it precludes classical grasp planning approaches based on the perception of visual object shape. For these cases, having a shape-adaptable hand is especially useful.

Experimental Setup For the experiment, two grasping strategies were implemented for the RBO Hand 1: the *push-grasp* strategy (Figure 8.1) and the *surface-constrained-grasp* (top-grasp) strategy (Figure 8.3). While the former was modeled on prior work [27], the latter was developed to optimally exploit the morphology of RBO Hand 1. Strategies closely related to the surface-constrained-grasp can be found for other grippers too [59].

The RBO Hand 1 was mounted on a seven degree-of-freedom robotic arm (Meka Robotics A2) for positioning and execution of the synergy. Control of the hand and arm during grasping was done without tactile or haptic feedback, but relied on active compliance provided by the arm joints of the robot. In each grasping trial, an object is placed as close as possible to a reference frame origin (see Figure 8.1a), while keeping its full volume in the $y < 0$ and $x > 0$ half-spaces, touching the $x-z$ and $y-z$ planes. We chose this placement because surfaces are usually much easier to perceive (visually) than for example center of mass or symmetry axes. The hand is then positioned in a fixed configuration relative to the object, and the arm and hand perform a scripted grasp. To perform the grasp, the actuators are inflated to 210 kPa. Following the grasp, the hand is lifted 100 mm along the z-axis, holds still for 1 s, and lowering the hand again, in small steps, for a total duration of 7 s. A grasp is deemed successful if the object followed the hand's motion, did not slip, and only contacted the hand. The test objects we selected to grasp are shown in Figure 8.2. The objects were selected to vary significantly in size, weight, shape, surface texture, and rigidity. We did not include objects that exceeded the inherent weight or size limitations of the hand.

For the push-grasp strategy, the robot arm first attains a fixed pre-grasp position, which is shown in Figure 8.1a. The hand then moves forward, making contact with the object and

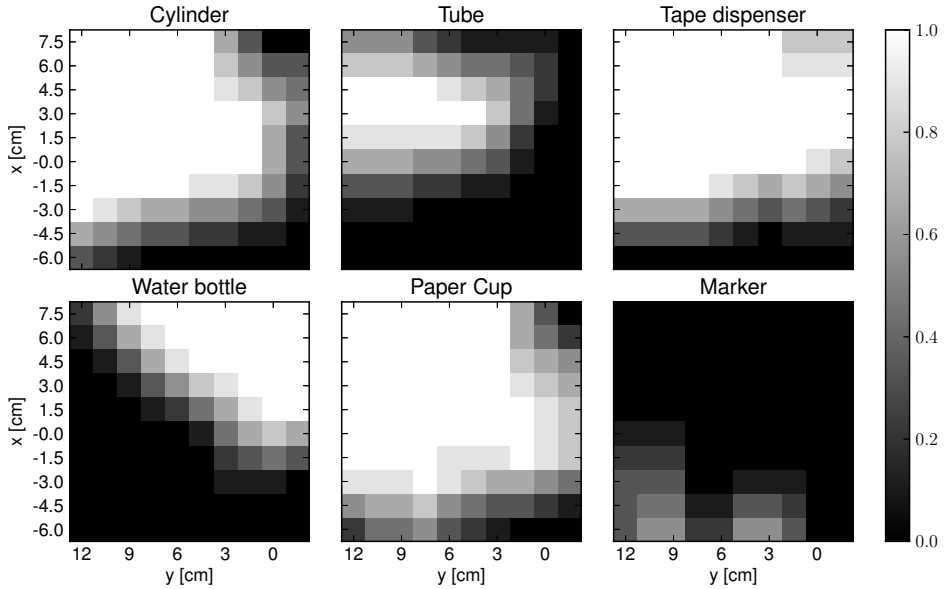

Fig. 8.4 Results of grasping six different objects with the push-grasp strategy. Pixel intensities denote grasp success probability, given the arm displacements in the horizontal plane and given the object. Images taken from Deimel and Brock [21]

possibly pushing it along the surface. The fingers are then flexed to cage and contact the object between fingers and palm.

The surface-constrained grasp exploits the support surface to guide the grasping motion, with help of the compliance of the palm. The hand is positioned above the reference frame and approaches the table surface from top down, with the palm pitched at 45°. The individual steps are shown in Figure 8.3. In these experiments the hand displacements were varied relative to a fixed object position.

To keep the number of trials feasible to execute, we restricted the experiment to only vary object type and two more spatial variables (object's (x,y) position) with an otherwise fixed action sequence and environment. In total, we conducted 1240 trials on ten different objects with two different grasps. Each object position was tried only once, and the success was recorded. The results are filtered with a 3×3 sliding window average, to model perceptual uncertainty and to estimate probabilities of grasp success over the x/y-plane. We expected the hand to be able to grasp all objects at least at one place, and that generally due to the compliance of the hand, we should find contiguous areas of successful grasps.

Results for the Push Grasp The success probability for the push-grasp is shown in Figure 8.4 and for the surface-constrained grasp in Figure 8.6. With the push grasp the hand can grasp most of the tested objects in an extended and contiguous range of object placements, which indicates a tolerance to position uncertainties. Although there are significant

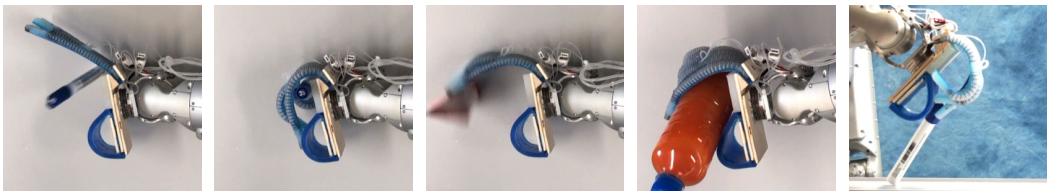

(a) tipping over (b) caging, no contact (c) fingers eject object (d) slipping (e) slipping

Fig. 8.5 Examples of grasp failures. Images taken from Deimel and Brock [21] ©2013 IEEE

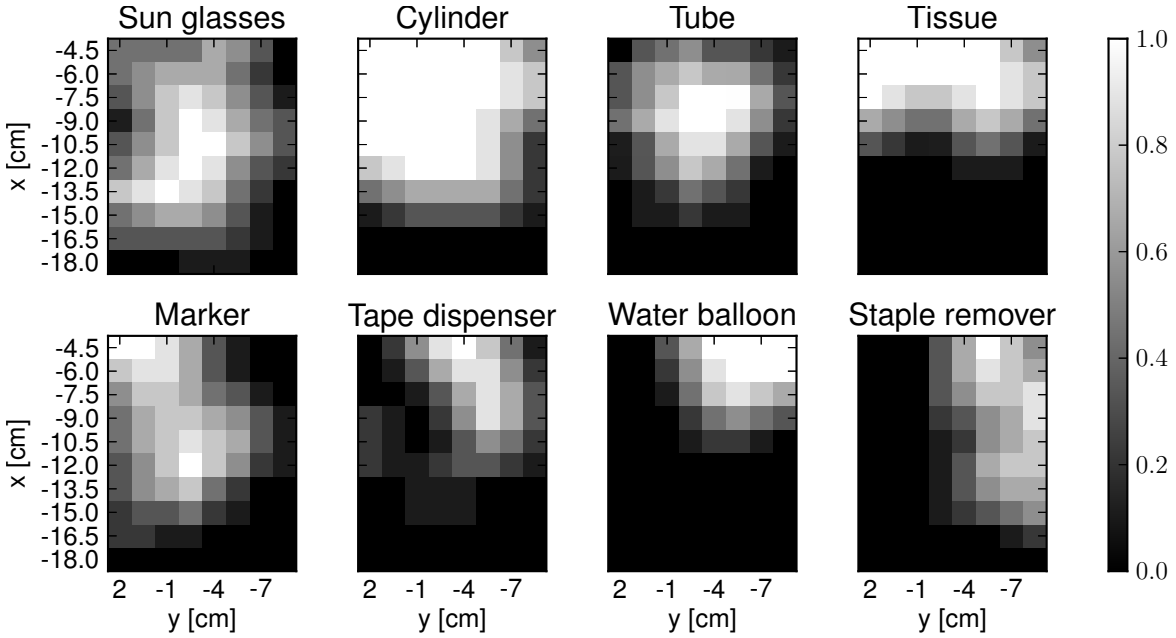

Fig. 8.6 Results of grasping eight different objects with the surface-constrained-grasp strategy. Pixel intensities denote grasp success probability, given the arm displacements in the horizontal plane and given the object. Images taken from Deimel and Brock [21] ©2013 IEEE

differences between the tested objects, a robot capable of distinguishing between them could easily select a reliable action sequence for each. The most difficult object for the push grasp was the marker, whose outer diameter is smaller than the inner diameter of the fully flexed fingers.

Results for the Surface-Constrained Grasp The success probability for the surface-constrained grasp is shown in Figure 8.6. The results are similar to those of the push-grasp experiment in Figure 8.4. All objects show a contiguous region in parameter space. This is expected when using compliant mechanisms, as they often exhibit gradual failure modes

Object	Surface material	Size	Weight
water bottle	PET	⌀63 mm × 215 mm	546 g
tube	PVC	⌀33 mm × 178 mm	114 g
cylinder	cardboard	⌀65 mm × 175 mm	106 g
water balloon	latex rubber	125 mm × 63 mm × 35 mm	99 g
tape dispenser	PP/PE	56 mm × 28 mm × 77 mm	30 g
staple remover	metal, PP	57 mm × 47 mm × 32 mm	20 g
sunglasses	glass, metal	125 mm × 36 mm × 23 mm	16 g
marker	PP/PE	⌀17 mm × 138 mm	14 g
paper cup	paper	⌀88 mm × 110 mm	13 g
tissue	PET fiber	150 mm × 150 mm × 0.2 mm	1 g

Table 8.1 Properties of tested objects, data from Deimel and Brock [21]

rather than abrupt changes in performance. The regions of success are comparable to other compliant hands as surveyed in [2]. Even though object properties vary significantly, the regions of success possess large overlaps — in this areas the robot can grasp many objects without requiring prior knowledge from perception about the exact object shape. With the sunglasses and marker we observed a fuzzy transition between the regions of success and failure that did not occur with the other objects. This suggests that these objects are difficult to adapt to for the hand, as even small variations in object placement can influence the grasp success.

8.2 Grasp Posture Diversity in the RBO Hand 2

The previous section demonstrated the advantage a compliant hand for grasping objects whose shape and position is not accurately known. In this section, we will investigate shape adaptability from a different direction. We will investigate the effect of compliance on the complexity of observed behavior. We will show that the RBO Hand 2 is able to produce a large number of grasp postures, almost on par with the diversity observed with humans, and that this diversity is created by compliant interaction with the grasped object. We will call this capability to enact diverse grasp postures *grasp posture diversity*.

Diverse grasp postures are a prerequisite for task-dependent manipulation. Examples of grasp postures can be found in grasp taxonomies from Cutkosky [18] and Feix et al. [37]. Such variability enables versatile grasping and manipulation: Small objects can be picked up with pincer grasps, large objects with enveloping power grasps. Depending on the task, a cylindrical side-grasp can be used to pick up a glass for drinking, whereas a disk grasp from above is appropriate to lift a glass off a cluttered table. We have to make clear the distinction

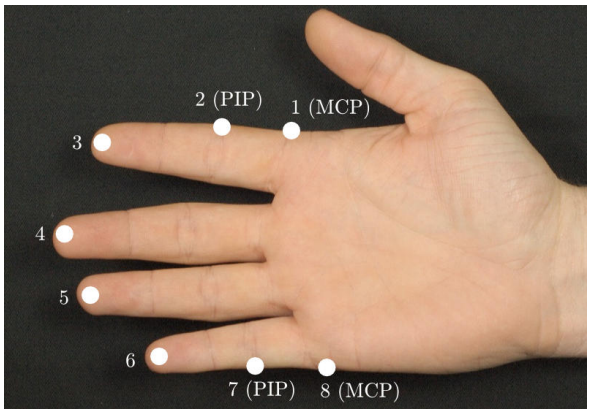

Fig. 8.7 The Kapandji test counts the number of indicated locations that can be contacted with the thumb tip. Image taken from Deimel and Brock [22] ©2016 Sage Publications

between grasp posture diversity and grasping dexterity as used in the context of in-hand manipulation, though. The former relates to final grasp postures and therefore considers a static state, while the latter is concerned about the diversity of motion patterns a hand is capable of while maintaining contact with the object.

Soft hands are often faced with the preconception that underactuation and mechanical compliance make diverse grasps difficult, if not impossible. Both properties make it hard to estimate or plan contact location and forces, as the hardware interacts with the object. From the view of the mechanistic paradigm, this precludes accurate control of posture and thus soft hands are not capable of enacting the postures we need at will. In this section we will show experiments that indicate the opposite. Soft hands are capable of providing the postures we need almost automatically, by virtue of their morphology and the mechanical interaction with the object. In Soft Manipulation, hand postures are seen as a *result* of interaction, and not a control target by itself. We will first investigate the range of thumb positions the RBO Hand 2 is capable of. Then, we will investigate how many grasps of a well known human grasp posture taxonomy we are able to enact, while relying only on a limited amount of control.

8.2.1 Thumb Dexterity

A dexterous, opposable thumb is known to play a pivotal role in the versatility of anthropomorphic hands. With humans, medical doctors employ the Kapandji test [58] to assess thumb dexterity during rehabilitation after injuries or surgery. This test was also used by Grebenstein [45] for evaluating and improving the thumb dexterity of the Awiwi hand. For the Kapandji test, the human subject is asked to touch a set of easily identifiable locations on the fingers with the tip of the thumb. These locations are indicated in Fig. 8.7. The total number of reachable locations serves as an indicator of overall thumb dexterity. A thumb is considered fully functional if it is able to reach all locations.

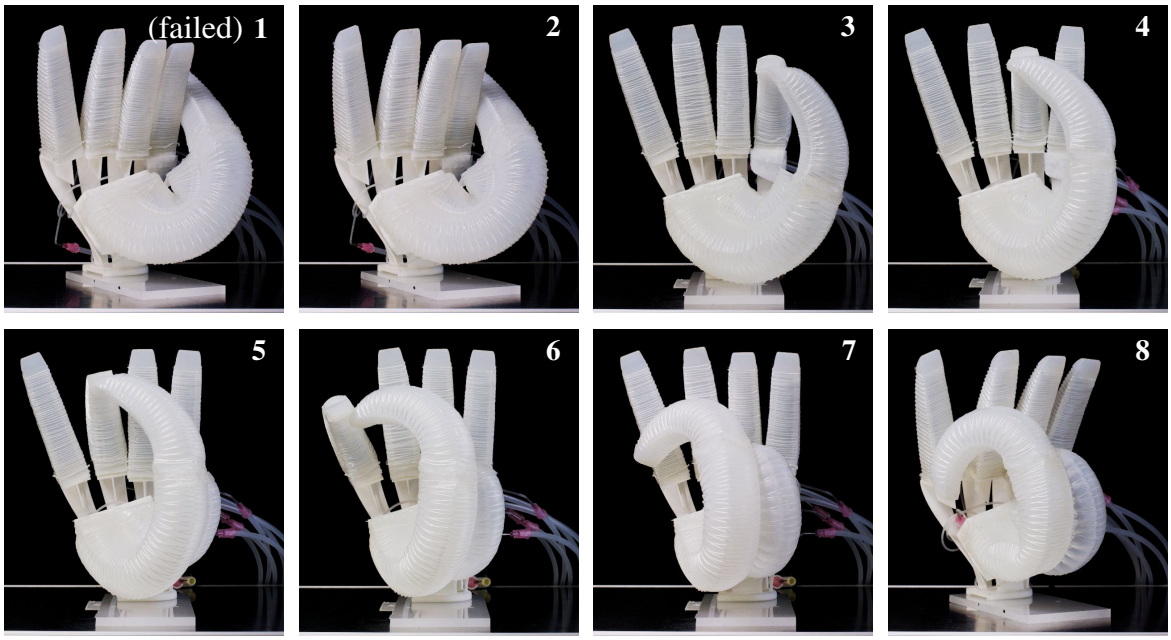

Fig. 8.8 The RBO Hand 2 succeeds in the Kapandji test for all but one position (position 1, upper left, showing best effort). Images taken from Deimel and Brock [22] ©2016 Sage Publications

To perform the Kapandji test on our hand, we manually selected actuation pressures that would position the thumb as desired. Figure 8.8 shows the performance for each of the eight locations. The thumb tip could reach all but one location. Location 1 was not possible to reach because it would require a stronger twist along the palm actuators. Still, the hand scores seven out of eight points on the test, indicating a high thumb dexterity. This result indicates that the palm and thumb kinematics of the RBO Hand 2, and its overall finger placement are well designed. It also suggests that – as with humans passing the Kapandji test – the hand is capable of dexterous grasping. We will now go on and further corroborate the claim that soft hands can provide grasp posture diversity by evaluating the number of grasp types we are able to attain with the RBO Hand 2.

8.2.2 Grasp Posture Diversity

A common way of assessing the dexterous grasping capabilities of hands is to demonstrate grasps for a set of objects. For example, the THE Second Hand was evaluated with four objects and two grasp types [46], the SDM hand on ten objects and a single grasp type [29], the Velo Gripper on twelve objects and a single grasp type [12], and the Awiwi hand on eight objects and 16 grasp types [45]. We follow these examples in our evaluation. We base our

investigation on the most comprehensive grasp taxonomy to date, the Feix taxonomy [37]. It covers the grasps most commonly observed in humans and therefore is a realistic reference for assessing the dexterity necessary for common human grasping tasks. The taxonomy encompasses 33 grasp types, out of which the first 17 are identical to the grasps in the Cutkosky taxonomy [18]. To demonstrate these 33 grasps, the original publication illustrates 17 different object shapes [37]. We therefore also used 17 objects and 33 grasp types to evaluate our hand.

We implemented the grasps from the Feix taxonomy by defining appropriate actuation pressures and actuation sequences. With most grasps, it is sufficient to inflate all actuation channels concurrently. For certain grasps though, such simultaneous actuation would result in inadvertent collisions between thumb and the other fingers. In these cases, we inflated the two channels controlling the palm actuators first, and then inflated the other two channels.

The commanded actuation pattern was then modified and tested iteratively to improve the quality of the grasp in terms of grasp stability and robustness against external forces, and to ensure the proper types and locations of contact. Grasp quality was judged by manually rotating and translating the hand, a grasp was considered successful when contacts between hand and object did not change during the disturbance. Each grasp was tested several times to ensure repeatability.

To simplify the search for appropriate actuation patterns, we attached the seven actuators to four actuation channels. Figure 7.6 enumerates these actuators. Channel A drives actuators 1, 2, and 3 (small, ring, and middle fingers), channel B drives actuator 4 (index finger), channel C drives actuators 5 (thumb) and 7 (inner palm), and channel D controls actuator 6 (outer palm).

To perform a grasping experiment for a particular grasp type, the experimenter triggers the actuation sequence to attain the pre-grasp posture, holds the object in the seemingly most appropriate location relative to the hand, and then triggers the actuation sequence for the grasping motion. The resulting postures for each empirical actuation pattern are shown in Fig. 8.9; high resolution images are provided in Extension 1. Out of 33 grasp types, the hand is able to perform 31 repeatably (three consecutive successful trials).

The two grasps that failed are the *light tool* grasp and the *distal type* grasp, both are shown in Figure 8.10. The light tool grasp fails because the hand does not possess any finger pulp that fills the cavity formed by the bent fingers, which causes the object to slip. The distal type grasp fails because, even though it is possible to put the soft fingers through the scissors' holes, the resulting grasp is nonfunctional with respect to proper use of the scissors. Attaining this grasp also requires an excessive amount of pre-grasp manipulation.

Fig. 8.9 Attempts to enact all grasps enacted from the Feix taxonomy [37], the hand failed to replicate grasps 5 (Light Tool) and 19 (Distal Type, Scissors). Images taken from Deimel and Brock [22] ©2016 Sage Publications

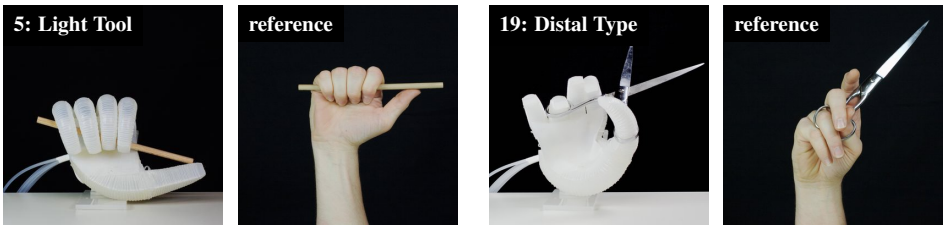

(a) Failed Light Tool grasp: no force closure

(b) Failed Distal Type grasp: functionally defective

Fig. 8.10 Grasping postures not successfully attained by the robotic hand. Image taken from Deimel and Brock [22] ©2016 Sage Publications

8.2.3 Postural Diversity by Interaction

We demonstrated grasp posture diversity of the RBO Hand 2 in the previous experiment, but it is possible (although not likely) that the grasps listed in the Feix taxonomy are not diverse enough to require a large number of hand postures, and the demonstrated diversity therefore is mostly a result of control. Such a finding would speak against the Soft Manipulation paradigm, and for a classical mechanistic view. To investigate this question, we compare the dimensionality of both control and hand posture when enacting Feix grasps. First, we will establish the complexity of observed behavior, then we will consider the complexity of the hand's actuation signals in relation to the observed behavior. We will see that control can not explain all observed behavior, and that we can contribute a substantial amount of postural diversity to come from the hand-object interaction.

Postural Diversity of the Feix Taxonomy To assess the dimensionality of the attainable grasp posture space, we first have to assert that the grasp set that we use to sample from that space is diverse enough, i.e. that the employed grasps span the space of possible grasps. For this, we recorded humans doing Feix taxonomy grasps with exactly the same objects as used with the RBO Hand 2, using the method published by Santello, Flanders, and Soechting [99]. We then compare the results to existing published data sets (the data published in Santello, Flanders, and Soechting [99], the UNIPI data set[1], and UNIPI-ASU data set[2] to check for consistency.

In the experiment, we asked five healthy human participants to enact every grasp of the Feix taxonomy five times while wearing a Cyberglove II data glove, using exactly the same objects as used for the experiment in the previous section. Participants were allowed to use their

[1]Data set available at http://handcorpus.org
[2]Data set available at http://handcorpus.org

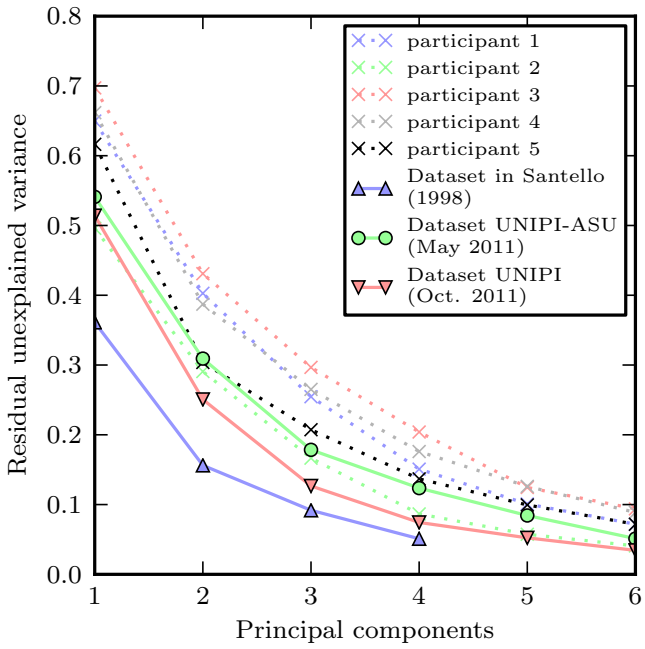

Fig. 8.11 Residual variances of PCA on joint measurements taken with data gloves. Solid lines denote published data sets using the method of Santello, Flanders, and Soechting [99], dotted lines denote the data acquired using the Feix taxonomy and the objects shown in Fig. 8.9. Image taken from Deimel and Brock [22] ©2016 Sage Publications

other hand to assist in assuming the grasp posture, but had to achieve a successful grasp in the sensorized hand without additional support. The resulting postures were sampled 50 times within 500 ms and averaged over samples and episodes. We then performed dimensionality reduction by applying principal component analysis (PCA) for each subject individually to exclude inter-subject variance in accordance with the data analysis procedure used in Santello, Flanders, and Soechting [99]. We then compared the resulting residual unexplained variances with data from literature.

The results are shown in Fig. 8.11. For four out of five participants, the unexplained variances were higher than those of the three independently published data sets, suggesting that the grasps span the space of possible grasp postures more effectively than the considerably larger but less structured set of objects that was used for the data sets we compared our data with. Therefore we can conclude that the grasps shown in Figure 8.9 indeed span the space of human grasp postures well.

The discrepancy between the published data sets and ours may be explained by the fact that the Santello and UNIPI data sets were recorded on grasping *imagined* objects, while our data and the UNIPI-ASU data set are recorded while grasping real objects. The additional variance observed may come from the interaction between hand and object, whereas with imagined objects, hand posture may be more related to actuation pattern than the actual grasp posture. This interpretation of existing data is consistent with our hypothesis that hand control is simpler than the effected posture.

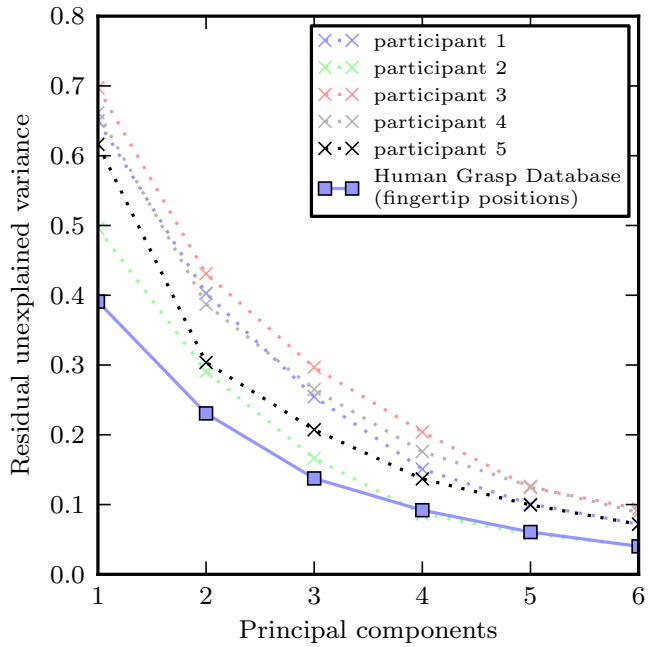

Fig. 8.12 Residual variances of PCA on grasp postures enacted by humans using data from different acquisition methods, joint angles and fingertip positions. Solid line denotes data from the Human Grasp Database [97], dotted lines denote the data acquired using the Feix taxonomy and the objects shown in Fig. 8.9 Image taken from Deimel and Brock [22] ©2016 Sage Publications

Diversity in Joint Angles vs. Fingertip Positions The comparison so far operated in the space of joint angles. Unfortunately, such a representation is not available for the RBO Hand 2, as it does not have joints. An alternative method is to express posture diversity in terms of fingertip position relative to the wrist. This has e.g. been done by Romero et al. [97], whose data are published in the Human Grasp Database experiment[3]. To use fingertip positions, we have to establish that their complexity is comparable to that of joint angle configurations. Figure 8.12 shows a comparison of the residual unexplained variances of a principal component analysis for fingertip position and joint angles (from the previous experiment), both acquired on human hands using the Feix taxonomy (31 grasps, excluding grasps 19 and 23 in Fig 8.9). The graph shows that fingertip positions may be an even more compact representation than joint angles. Therefore we can safely use fingertip position data as a conservative estimate of joint posture posture diversity. We also tested if omitting fingertip orientation data from the Principal Component Analysis decreases unexplained variance, but it did not significantly. It was therefore excluded from analysis to simplify the data acquisition with the RBO Hand 2 using a motion capture system.

Putting the pieces together, we have established that the grasp list and objects the RBO Hand 2 was tested with indeed provides a faithful coverage of grasp diversity in line with data published in literature on human grasping. We also established that fingertip position is a viable alternative to joint angles for assessing postural diversity of human hands and therefore

[3]Data set available at http://grasp.xief.net/

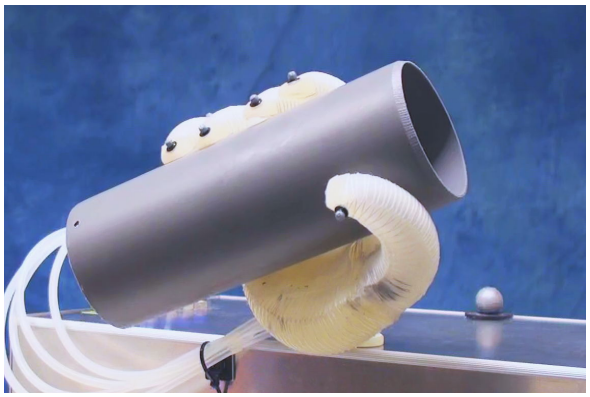

Fig. 8.13 Screen shot from video Extension 4, showing the marker placement on the fingertips for Motion Capture. Image taken from Deimel and Brock [22] ©2016 Sage Publications

also of anthropomorphic robot hands. This provides a strong support for the significance of the results on postural diversity with the RBO Hand 2 in the next experiment.

Postural Diversity of RBO Hand 2 grasps The previous subsection gives us a solid justification to use fingertip positions of grasps from the Feix taxonomy to assess the RBO Hand 2 in terms of grasp posture diversity. To acquire the fingertip positions we used a camera-based motion capture system and placed 3 mm retroreflective markers on the backside of the fingertips of the four fingers. The marker placement can be seen in Fig. 8.13. On the thumb tip, the marker was placed on the side to not interfere with the pincer grasp.

The motion capture system has a spatial noise of 0.05 mm, as measured using 205 frames recorded for a stationary hand (at 50 Hz). For each grasp, two trials are recorded, fingertip positions are extracted and averaged over the trials before applying Principal Component Analysis. The data set from the Human Grasp Database is subjected to the same procedure. The results are shown in Fig. 8.14. The postural dimensionality exhibited by the RBO Hand 2 matches the human hand data well. This strongly supports our claim that our robotic hand is as dexterous as a human hand with respect to attainable grasp posture, taking the Feix taxonomy as a reference.

8.2.4 Actuation Complexity

Fig. 8.15 shows a scatter plot of the actuation patterns (amount of inflation per channel) for the 31 successfully achieved grasp types of the Feix taxonomy. The actuation patterns relate to final grasps, not pre-grasp postures. The plots reveal an even distribution of activation levels for all channels and do not reveal obvious correlations that could be leveraged to further simplify actuation. A principal component analysis of the actuation patterns is shown in Figure 8.14, where residual unexplained variances of the actuation (dotted line) are compared with those of the resulting hand posture (solid line). The space of grasp postures is of

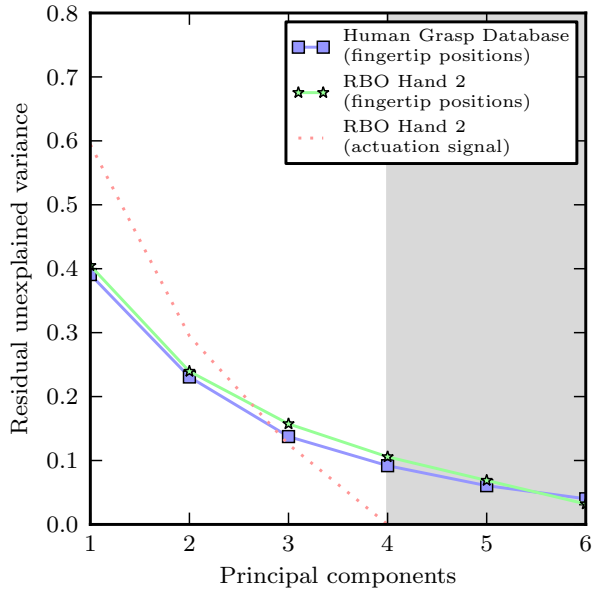

Fig. 8.14 Dimensionality of fingertip positions for a human hand, the RBO Hand 2, and its respective control signal. The gray region indicates where the dimensionality of fingertip posture exceeds control dimensionality. Image taken from Deimel and Brock [22] ©2016 Sage Publications

higher dimensionality than the actuation space, which is of dimension four. Where does this increase come from? It must be introduced by the diverse shapes of the grasped objects. The interactions between the hand and the object differentiates the postures, facilitated by the hand's ability to adapt to objects compliantly. Tavakoli et al. [111] also obtain the minimum of four to six actuated degrees of freedom to implement dexterous grasping for their anthropomorphic, compliant hand.

The diversity and consistency of evidence we presented here strongly suggests that compliant hands benefit dexterous grasping. The presented evaluation, based on published data sets, measurements of human grasps, and of grasps with the RBO Hand 2, paints a consistent picture: The robotic hand performs similar to a human hand, both in terms of grasp posture diversity, and in terms of covering sets of grasps, again, using the Feix taxonomy as a reference. This diversity in grasping posture is achieved by the RBO Hand 2 with only four actuated degrees of freedom. This is possible because the interaction of the compliant degrees of freedom with the diverse objects introduces additional variance in the posture.

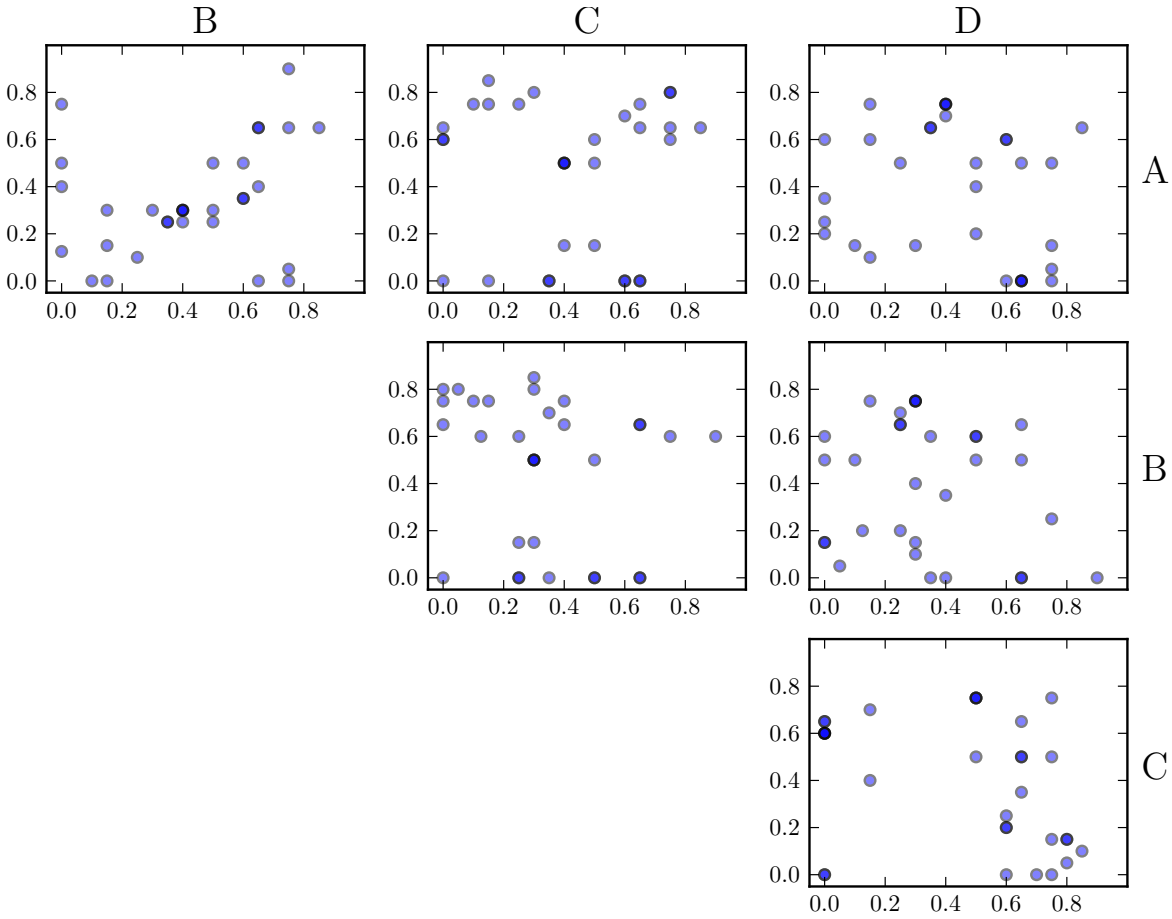

Fig. 8.15 Scatter plots of the four actuation channels for the actuation patterns of the 31 successful grasps. Darker color indicates overlapping dots. Actuator to (A,B,C,D) channel map as described in Sec. 8.2.2. Image taken from Deimel and Brock [22] ©2016 Sage Publications

8.3 Conclusion

In the first section of this chapter we evaluated the grasping capability of the RBO Hand 1 in the context of two grasping strategies. We were able to reliably pick up a number of irregularly shaped objects, including two deformable ones. The final orientation of the grasped object and location in the hand varied considerably depending on the precise placement. Nevertheless, the hand shows a contiguous region of success for each object. This indicates that the hand is both capable of adapting to the object's shape and its orientation, but also that this adaptation leads to a tolerance against position errors that may be caused by perception or arm control. These findings demonstrate, that pneumatic soft hands are capable of shape adaptation, but at the same time also are able to provide enough grasp strength to lift

objects. The RBO Hand 1's relatively low payload is the result of overly compliant fingers though.

In the second section we presented experiments that support the claim that pneumatic soft hands are not only capable of shape adaptation, but that they are also capable of providing a rich, diverse set of grasp postures using only very limited amount of control. In terms of grasp posture diversity, the hand is almost as capable as a human hand. The anthropomorphic RBO Hand 2 also demonstrates the potential of complex soft hand morphologies based on non-straight actuators and non-constant stiffness profiles along finger actuators. While the capability to maintain a grasp posture is a necessary skill, it does not imply that a robot is also capable of attaining a grasp posture with that hand. This topic will be investigated in the following chapter.

Chapter 9

Exploiting Environmental Constraints with Soft Hands

This chapter presents experiments that demonstrate how robot systems can execute robust grasping strategies based on exploiting environmental constraints to motion, and that the implementation of such strategies becomes simple with soft hands.

9.1 Environmental Constraints to Motion

In Chapter 6 we identified several principles for Soft Manipulation that have in common an active, intentional use of the environment to make a grasping strategy more robust and reliable. Based on these, we formulated the concept of *Environmental Constraints Exploitation*, where we primarily use environmental constraints to motion, to guide hand and object motion during a grasping strategy. These environmental constraints can be as simple as a horizontal surface (table), but also include edges on horizontal surfaces, corners, and even a second hand. We already used several grasping strategies that exploit environmental constraints for the experiments in the previous chapters. In Chapter 8 we showed two grasp strategies implemented with the RBO Hand 1, the surface-constrained grasp (or top-grasp), and the push grasp. Both grasp strategies are also possible with the RBO Hand 2. The field of grasping also provides a number accounts of grasping and pre-grasp manipulation strategies that use contact with the environment to become more robust and reliable [27, 62, 66, 10]. In this Chapter, we will present two more grasping strategies that rely on environmental constraints, and which are robustly implementable with the help of soft hands.

9.1.1 The Edge Grasp with the RBO Hand 1

The edge grasp is a simple grasping strategy that can be used when an object already is close to the edge of a surface. Figure 9.1 illustrates the individual phases of the edge grasp. In the illustration, the parts colored red denote environmental features whose presence is necessary during execution. The execution of the strategy relies on compliant collisions and on the soft hand's ability to adjust posture for small wrist motion errors. As a result, we are able to use interpolation in joint space for end effector motion to implement grasping strategies.

We also demonstrate the robustness towards variations in the grasping scene. In an experiment, we place cylinders of varying size parallel to the table edge at a varying distance. We then perform the edge grasp strategy with the RBO Hand 1 and evaluate the grasp success. Figure 9.2 shows a scatter plot of the trial results. The strategy works for a large range of cylinder sizes, especially for small cylinders. Another important detail is the spatial contiguousness of region of the successful trials. This means that we only need to make sure that scene parameters (e.g. object position) are within this region. To expect a successful grasp attempt, there is no need for more accurate information.

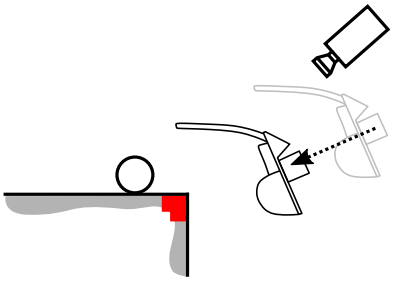	The edge is used as a visual environmental constraint to position the hand relative to it (alternatively, the object could also be used). A visual servoing controller terminates when hand and edge are vertically aligned.	
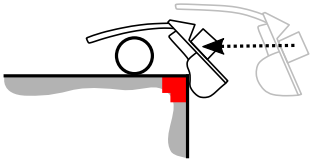	The edge is used as an environmental constraint to position the hand close to the object. A compliant position controller moves the hand towards the edge until contact.	
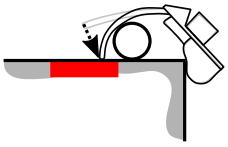	The surface is used as an environmental constraint to position the fingers. A controller flexes the fingers compliantly until they contact the surface. Upon termination, they are at the lowest possible position w.r.t. the object. Additionally, the object is caged.	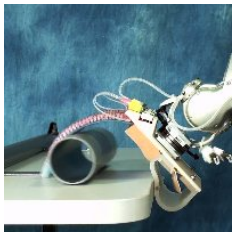
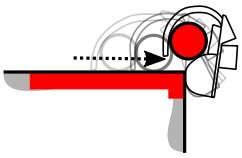	The edge in conjunction with the surface is used as an environmental constraint by the hand to enclose the object. A compliant position controller rotates the hand to unload the contact at the fingertips. While the fingertips move the object towards the palmar pad their motion is constrained by the surface. Upon termination, the hand encloses the object.	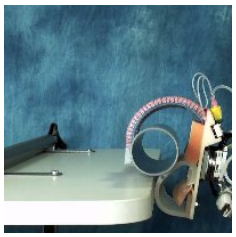

Fig. 9.1 Edge-grasp strategy with RBO Hand 1. Figure taken from Eppner et al. [32] ©2015 Sage Publications

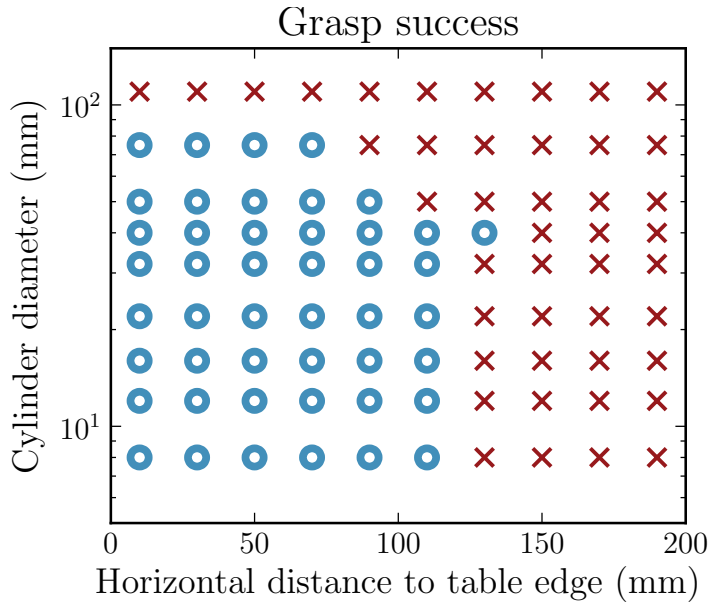

Fig. 9.2 Slide-to-edge grasp. Distance measured horizontally from lower edge of palm plate to closest object surface. Circles indicate successful grasps. Figure taken from Eppner et al. [32] ©2015 Sage Publications

9.1.2 The Slide-to-Wall Grasp with the RBO Hand 2

In the second grasp strategy example, we use the RBO Hand 2 to exploit environmental constraints. This time, we will use the edge between a horizontal and a vertical surface in a more elaborate grasping strategy. Its phases are illustrated in Figure 9.3. This slide-to-wall grasp strategy first sweeps an object towards a corner, then inflates the fingers slightly and rotates them to slip under the object. Then the wall is used to create a cage which is then shrunk by inflating the fingers. The grasp is then finally established by rotating the hand away from the wall, enabling the fingers to wrap around the object.

As with the previous grasp strategy, this one can be executed with simple joint space interpolation between a few key hand and wrist postures. Compliant arm motion together with the compliance of the hand makes it possible tolerate significant errors in positioning. Obviously, any cylinder placed between the start point of the sweep and the corner will be graspable. Object size too, can vary in a large range, as arm and finger compliance adapt accordingly. But as importantly, we can also adapt to deviations in the environmental constraints. To demonstrate this capability, we applied the slide-to-wall grasp strategy to walls of different inclination. Figure 9.4 shows the probability of success when picking a cylinder with 22 mm diameter. The experiment tested at $40°, 45°, 50°, 60°, 70°, 80°, 85°$, and $90°$ wall inclination. The grasp reliably works at $60°$, but the strategy still succeeds when deviating up to $15°$ from this value. Overall, the grasp strategy succeeds in the range of $45°$ to $90°$, which probably covers the inclinations of most walls. This result indicates a robustness of such grasping strategies not only against object variations, but also against variation in the environment.

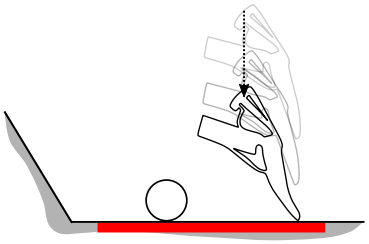	The surface is used as an environmental constraint to position the hand. A compliant position controller moves the hand downwards until it touches the surface. Upon termination, the fingertips are aligned vertically w.r.t. the object.	
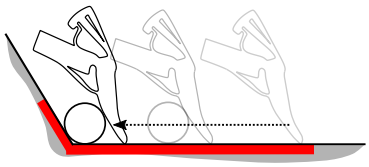	The surface in conjunction with the corner is used as an environmental constraint. A compliant position controller moves the hand horizontally to slide fingers across the surface, exploiting it as a constraint to fingertip position. The vertical surface constraints the horizontal motion. Upon termination, the object is caged by hand and environment.	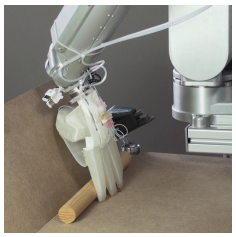
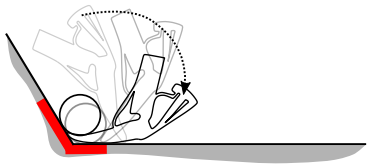	The corner surfaces are used as an environmental constraint to slide the fingers under the object.	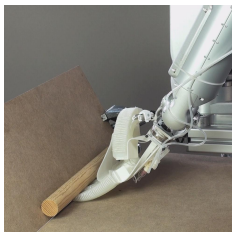
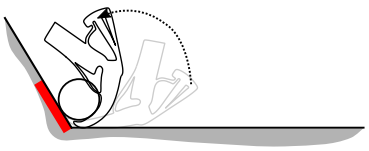	The wall is used as an environmental constraint to rotate the hand and prepare the grasp.	
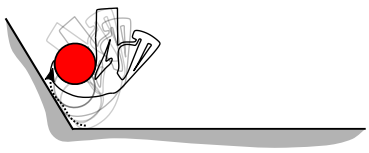	The hand is then lifted and its fingers are flexed to roll the object into the hand. Fingertip position is constrained by the wall, making them contact the object in the best possible location for attaining force closure.	

Fig. 9.3 Slide-to-wall grasp strategy with RBO Hand 2. Figure taken from Eppner et al. [32] ©2015 Sage Publication

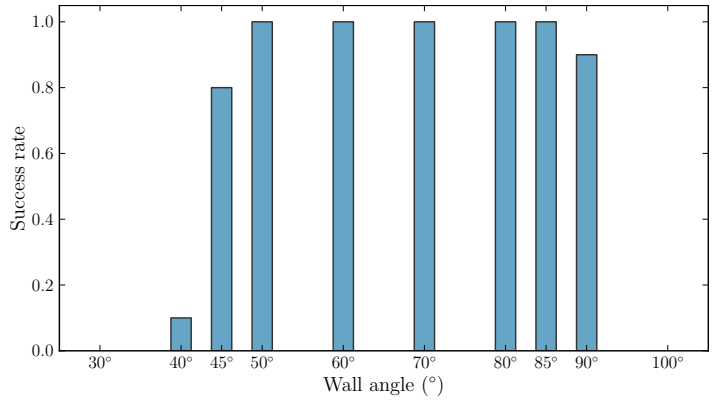

Fig. 9.4 Success of Slide-to-wall grasp under varying wall angles relative to horizontal table surface, 10 trials per angle. Image taken from Eppner et al. [32] ©2015 Sage Publications

9.2 Conclusion

This chapter presented two example grasping strategies that follow the principles of the *Soft Manipulation* paradigm and the *Environmental Constraint Exploitation* concept. We demonstrated the suitability of soft hands for implementing such strategies, as they make it easy to contact by collision, slide along surfaces without losing contact, and to adapt to limited deviations in the grasping scene. The resulting grasping strategies are successful for a contiguous range of scene parameters such as position and size which greatly simplifies the requirements to perception. In addition to the two strategies elaborated here, Chapter 8 demonstrates two more strategies using pneumatic soft hands: The push-grasp shown in Figure 8.1, and the surface-constrained grasp shown in Figure 8.3. Both grasps depend on the table surface to succeed. The push grasp uses it to constrain object motion into a two-dimensional plane, while the surface-constrained grasp uses it to position the hand and cage the object.

While this chapter only lists a small number of environmental-constraint-exploiting strategies, we believe that a large enough "bag of tricks" will make it possible to cover many or most situations encountered by a robot. Ideally, we will be able to synthesize grasping strategies based on a perceived grasping scene [31], and optimize motion primitives for soft hands with machine learning [48]. This also points towards the challenges of future work. Soft hands need to be designed to satisfy the requirements of a large number of those strategies. At the same time, designing motion primitives by a human expert is time consuming and biased towards strategies suitable for human hands. In this light, the advances in simulating soft hands that were presented in Chapter 5 are especially exciting, as they offer the chance to do machine learning of constraint-exploiting grasping strategies and at the same time to optimize the hand morphology for those strategies.

Chapter 10

Conclusions

10.1 Summary and Main Findings

In this thesis we tackled the problem of how to enable robots to grasp robustly and reliably. It investigated the application of a new way of understanding grasping. This required us to not just incrementally improve individual components in an existing system, but to rethink and re-frame all aspects of the robot system. Therefore, this thesis included topics at many abstraction levels, from building physical artifacts to control and modeling and finally to concepts for generating grasping behavior for soft hands. The thesis was structured into two parts. Part I covered the practical engineering question of how to build, assemble and model components for building pneumatic soft hands, and how to simulate grasping attempts with pneumatic soft hands. Part II covered the concepts that motivate building soft hands, and investigated the properties and ultimately usefulness of specific soft hand artifacts.

In Chapter 2 we gave an overview into current approaches to building pneumatic soft continuum actuators, which provide the basic building block of pneumatic soft hand designs.

In Chapter 3 we presented a toolkit for building soft hands, which at its core is a coherent collection of methods to design, simulate and build pneumatic soft continuum actuators for rapidly prototyping soft hands.

In Chapter 4 we complemented the soft pneumatic actuators with the *equilibrium point control* scheme which in contrast to position and force control respects and preserves the main feature of compliant actuators. We provided an air mass controller as an example implementation of equilibrium-point control for PneuFlex actuators, and demonstrated stable, fast and repeatable execution of continuous trajectories.

In Chapter 5 we revisited the analytic model for PneuFlex actuators, extended it, and implemented it in a simulator. We demonstrated qualitative and quantitative congruence of model behavior with real actuators in several validation experiments. We also demonstrated that soft hands can be simulated at about $0.1\times$ real time, opening up new opportunities of automated soft hand design.

Part II starts with Chapter 6, where we constructed the Soft Manipulation paradigm from specific observations. We then proposed a list of principles for Soft Manipulation, and developed the concept of exploiting environmental constraints to motion, which was used in the subsequent chapters.

In Chapter 7 we analyzed existing grippers and robotic hands with respect to their usefulness for Soft Manipulation and found that many recent designs partially incorporate compliance and softness already, and that these design ideas can be leveraged for developing soft hands. Further, the chapter also described the RBO Hand 1 and RBO Hand 2, and the design decisions made to provide a maximum of compliance and softness.

Chapter 8 finally investigated the properties of the two soft hands, and found that they both provide *shape adaptability* during grasping. In addition, we showed in a series of experiments, that the anthropomorphic RBO Hand 2 exhibits a diversity of grasps that is comparable to that observed with humans. We further show that this is not due to sophisticated control, but because of compliant interactions which are facilitated by the hand's morphology.

We completed the big picture of soft hands in Chapter 9, where we demonstrate how soft hands can be used to implement robust and reliable grasping strategies based on the concept of *exploiting environmental constraints*, which we believe plays a central role in the Soft Manipulation paradigm.

10.1.1 Research Questions

In the introduction we formulated four research questions:

> *"How can we rapidly prototype soft hands in order to catch up with conventional hands in terms of versatility and integration, and quickly advance research in Soft Manipulation?"*

The research question was answered by Part I. We developed an extensive set of methods and tools to provide all components necessary to rapidly prototype soft hands. The central contribution is the PneuFlex toolkit in Chapter 3 which provides methods to design, and manufacture pneumatic soft continuum actuators and is complemented by methods to assemble sets of actuators into soft hands. Chapter 4 presented a control scheme that provides stable and fast continuous control of pneumatic soft hands. This considerably simplifies integration with existing approaches to learning motion primitives. Finally, the thesis also lays the foundations for automated design of soft hands. In Chapter 5 we developed a simulation model capable of dynamically simulating grasping strategies with soft hands at about $0.1\times$real time speed. It enables us to improve soft hand morphologies and investigate new design ideas at a much faster pace than is currently possible. This will allow future soft hands to catch up with the sophistication of conventional hands.

> *"Does softness as* the *guiding design principle lead to practical robot manipulators at all, or does softness make grasping more difficult as one would assume in the mechanistic view (because posture becomes less uncontrollable)?"*

This research question was covered in Part II. We found that softness is already used in existing gripper designs for specific purposes. Two pneumatic soft hands, the RBO Hand 1 and RBO Hand 2 were designed for maximum compliance. In Chapter 8 we demonstrated their capability to grasp diverse objects, and also their capability to provide many different grasps. In Chapter 9 we further show that the compliance of the hands makes implementing grasping strategies that exploit environmental constraints very simple. We therefore conclude

that softness indeed provides a useful design principle, if it is used in systems that follow the Soft Manipulation elaborated in Chapter 6.

"What are the limits to the intrinsic shape adaptability of soft hands? How much additional control is necessary to complement it?"

In Chapter 8 we investigated the control necessary for implementing the list of grasp types by Feix et al. [37]. We found that the observed control complexity is significantly below the complexity of observed behavior.

"If hand posture and contact forces are not under the robot's direct control, how else can grasping be orchestrated?"

We proposed an answer to this question in Chapter 6 and demonstrated examples in Chapters 8 and 9. Interactions with the object to grasp and the environment provide action patterns for grasping that are robustly and reliably executable. These actions can be understood and designed with the Soft Manipulation paradigm which offers an alternative to the prevailing "mechanistic" paradigm for reasoning about grasping. The change from planning contact point configurations to planning sequences of interaction patterns also changes the design goals of robot hands — from rigid-linked and fully controlled and precise hands to adaptive, compliant and underactuated soft hands.

10.2 Open Questions and Future Work

The thesis provides a solid foundation for future investigations into the design space of pneumatic soft hands. But because soft hands use such a radically different technology compared to almost all other existing robot hands, it is difficult and often impossible to use existing proprioceptive or haptic sensor technologies. Sensors that are compatible with fluidic soft continuum actuators currently require either considerable investment in production facilities, or do not provide high quality sensor signals. Fortunately, research in this area is very active [35, 44, 108, 56, 116, 53], and we believe it will soon be feasible to integrate a considerable amount of sensors into soft hands. Addition of haptic and proprioceptive perception will also enable researchers to apply machine learning methods, which promises to boost the competence of soft handed robots.

A second promising future research topic is the automated design of soft hand morphologies. Due to their mechanical structure, we can adjust many mechanical parameters of fluidic soft continuum actuators and still guarantee their manufacturability. At the same time, effects of changes on the outcome of the mechanically opaque grasping strategies used in the Soft Manipulation paradigm are hard to predict even by expert users. Automated design based on an efficient simulation could emerge as a powerful tool here to improve hand morphology

for specific grasping application. Soft hands and grasping strategies could even be designed concurrently to leverage the strengths of each domain. Such tools would accelerate the path from basic research into productive applications for soft hands.

Part III

Back Matter

References

[1] Jérémie Allard et al. “SOFA - an Open Source Framework for Medical Simulation”. In: *Medicine Meets Virtual Reality, MMVR 15, February, 2007*. Long Beach, California, Etats-Unis, 2007, pp. 1–6.

[2] J.R. Amend et al. “A Positive Pressure Universal Gripper Based on the Jamming of Granular Material”. In: *IEEE Transactions on Robotics* 28.2 (2012), pp. 341 –350.

[3] J Bae et al. “Development of a low cost anthropomorphic robot hand with high capability”. In: *IEEE/RSJ International Conference on Intelligent Robots and Systems (IROS)*. IEEE/RSJ International Conference on Intelligent Robots and Systems (IROS). 2012, pp. 4776–4782.

[4] C. M. Best et al. “A New Soft Robot Control Method: Using Model Predictive Control for a Pneumatically Actuated Humanoid”. In: *IEEE Robotics Automation Magazine* 23.3 (2016), pp. 75–84.

[5] Antonio Bicchi, Marco Gabiccini, and Marco Santello. “Modelling Natural and Artificial Hands with Synergies”. In: *Philosophical Transactions of the Royal Society B: Biological Sciences* 366.1581 (2011), pp. 3153–3161.

[6] J. Bishop-Moser and S. Kota. “Design and Modeling of Generalized Fiber-Reinforced Pneumatic Soft Actuators”. In: *IEEE Transactions on Robotics* 31.3 (2015), pp. 536–545.

[7] J. Bishop-Moser et al. “Design of Soft Robotic Actuators using Fluid-filled Fiber-Reinforced Elastomeric Enclosures in Parallel Combinations”. In: *Proceedings of IEEE/RSJ International Conference on Intelligent Robots and Systems (IROS)*. IEEE/RSJ International Conference on Intelligent Robots and Systems (IROS). 2012, pp. 4264–4269.

[8] M. Bonilla et al. “Grasping with Soft Hands”. In: *2014 IEEE-RAS International Conference on Humanoid Robots*. 2014 IEEE-RAS International Conference on Humanoid Robots. 2014, pp. 581–587.

[9] M. G. Catalano et al. “Adaptive synergies for the design and control of the Pisa/IIT SoftHand”. In: *The International Journal of Robotics Research* 33.5 (2014), pp. 768–782.

[10] N. Chavan Dafle et al. “Extrinsic dexterity: In-hand manipulation with external forces”. In: *2014 IEEE International Conference on Robotics and Automation (ICRA)*. 2014 IEEE International Conference on Robotics and Automation (ICRA). 2014, pp. 1578–1585.

[11] M. Cianchetti et al. “STIFF-FLOP surgical manipulator: Mechanical design and experimental characterization of the single module”. In: *2013 IEEE/RSJ International Conference on Intelligent Robots and Systems*. 2013, pp. 3576–3581.

[12] M. Ciocarlie, F. Mier Hicks, and S. Stanford. “Kinetic and Dimensional Optimization for a Tendon-Driven Gripper”. In: *IEEE International Conference on Robotics and Automation (ICRA)*. IEEE International Conference on Robotics and Automation (ICRA). Karlsruhe, Germany, 2013, pp. 2751–2758.

[13] M. Ciocarlie et al. “Towards reliable grasping and manipulation in household environments”. In: *Proceedings of RSS 2010 Workshop on Strategies and Evaluation for Mobile Manipulation in Household Environments*. 2010.

[14] M. T. Ciocarlie and P. K. Allen. “Hand Posture Subspaces for Dexterous Robotic Grasping”. In: *The International Journal of Robotics Research* 28.7 (2009), pp. 851 –867.

[15] Fionnuala Connolly, Conor J. Walsh, and Katia Bertoldi. “Automatic design of fiber-reinforced soft actuators for trajectory matching”. In: *Proceedings of the National Academy of Sciences* 114.1 (2017), pp. 51–56.

[16] Fionnuala Connolly et al. “Mechanical Programming of Soft Actuators by Varying Fiber Angle”. In: *Soft Robotics* 2.1 (2015), pp. 26–32.

[17] M. Controzzi, C. Cipriani, and M. C. Carozza. “Design of Artificial Hands: A review”. In: *The Human Hand as an Inspiration for Robot Hand Development*. Vol. 95. Springer Tracts in Advanced Robotics. Springer, 2014, pp. 219–247.

[18] M. R Cutkosky. “On grasp choice, grasp models, and the design of hands for manufacturing tasks”. In: *IEEE Transactions on Robotics and Automation* 5.3 (1989), pp. 269–279.

[19] R Deimel. *RBO Hand 2 CAD Files*. http://dx.doi.org/10.14279/depositonce-5831. 2017.

[20] R. Deimel et al. “Exploitation of Environmental Constraints in Human and Robotic Grasping”. In: *Proceedings of the International Symposium on Robotics Research (ISRR)*. International Symposium on Robotics Research (ISRR). 2013.

[21] Raphael Deimel and Oliver Brock. “A Compliant Hand Based on a Novel Pneumatic Actuator”. In: *IEEE International Conference on Robotics and Automation (ICRA)*. IEEE International Conference on Robotics and Automation (ICRA). 2013, pp. 2047–2053.

[22] Raphael Deimel and Oliver Brock. “A novel type of compliant and underactuated robotic hand for dexterous grasping”. In: *The International Journal of Robotics Research* 35.1 (2016), pp. 161–185.

[23] Raphael Deimel and Oliver Brock. “A novel type of compliant, underactuated robotic hand for dexterous grasping”. In: *Proceedings of Robotics: Science and Systems (RSS)*. Robotics: Science and Systems. 2014, pp. 1687–1692.

[24] Raphael Deimel and Oliver Brock. “Soft Hands for Reliable Grasping Strategies”. In: *Soft Robotics, Soft Hands, Grasping*. Berlin Heidelberg: Springer-Verlag, 2015, pp. 211–221.

[25] Raphael Deimel, Marcel Radke, and Oliver Brock. “Mass control of pneumatic soft continuum actuators with commodity components”. In: *Proceedings of the Intelligent Robots and Systems (IROS), 2016 IEEE/RSJ International Conference on*. IEEE, 2016, pp. 774–779.

[26] M. Dogar and Siddhartha Srinivasa. “A framework for push-grasping in clutter”. In: *Robotics: Science and Systems VII* (2011).

[27] M.R. Dogar and S.S. Srinivasa. “Push-grasping with dexterous hands: Mechanics and a method”. In: *2010 IEEE/RSJ International Conference on Intelligent Robots and Systems (IROS)*. 2010, pp. 2123–2130.

[28] T. Doi et al. “Proposal of flexible robotic arm with thin McKibben actuators mimicking octopus arm structure”. In: *2016 IEEE/RSJ International Conference on Intelligent Robots and Systems (IROS)*. 2016 IEEE/RSJ International Conference on Intelligent Robots and Systems (IROS). 2016, pp. 5503–5508.

[29] A. M Dollar and R. D Howe. “Simple, reliable robotic grasping for human environments”. In: *IEEE International Conference on Technologies for Practical Robot Applications (TePRA)*. 2008, pp. 156–161.

[30] Aaron M. Dollar and Robert D. Howe. “The Highly Adaptive SDM Hand: Design and Performance Evaluation”. In: *The International Journal of Robotics Research* 29.5 (2010), pp. 585–597.

[31] Clemens Eppner and Oliver Brock. “Planning Grasp Strategies That Exploit Environmental Constraints”. In: *2015 IEEE International Conference on Robotics and Automation (ICRA)*. IEEE International Conference on Robotics and Automation (ICRA). 2015, pp. 4947–4952.

[32] Clemens Eppner et al. “Exploitation of environmental constraints in human and robotic grasping”. In: *The International Journal of Robotics Research* 34.7 (2015), pp. 1021–1038.

[33] Clemens Eppner et al. “Lessons from the Amazon Picking Challenge: Four Aspects of Building Robotic Systems”. In: *Proceedings of Robotics: Science and Systems*. Proceedings of Robotics: Science and Systems. Ann Arbor, MI, USA, 2016.

[34] M. A. Erdmann and M. T. Mason. “An exploration of sensorless manipulation”. In: *IEEE Journal on Robotics and Automation* 4.4 (1988), pp. 369–379.

[35] Nicholas Farrow and Nikolaus Correll. “A soft pneumatic actuator that can sense grasp and touch”. In: *2015 IEEE/RSJ International Conference on Intelligent Robots and Systems (IROS)*. 2015 IEEE/RSJ International Conference on Intelligent Robots and Systems (IROS). 2015, pp. 2317–2323.

[36] T. Feix, I.M. Bullock, and A.M. Dollar. “Analysis of Human Grasping Behavior: Object Characteristics and Grasp Type”. In: *IEEE Transactions on Haptics* 7.3 (2014), pp. 311–323.

[37] T. Feix et al. “A comprehensive grasp taxonomy”. In: *Robotics, Science and Systems: Workshop on Understanding the Human Hand for Advancing Robotic Manipulation*. 2009.

[38] J. Fraś et al. “New STIFF-FLOP module construction idea for improved actuation and sensing”. In: *2015 IEEE International Conference on Robotics and Automation (ICRA)*. 2015, pp. 2901–2906.

[39] Y. Fujihira et al. “Experimental investigation of effect of fingertip stiffness on resistible force in grasping”. In: *2015 IEEE International Conference on Robotics and Automation (ICRA)*. 2015 IEEE International Conference on Robotics and Automation (ICRA). 2015, pp. 4334–4340.

[40] I. Gaiser et al. “A new anthropomorphic robotic hand”. In: *8th IEEE-RAS International Conference on Humanoid Robots (Humanoids)*. 8th IEEE-RAS International Conference on Humanoid Robots (Humanoids). 2008, pp. 418–422.

[41] Kevin C. Galloway et al. “Mechanically Programmable Bend Radius for Fiber-Reinforced Soft Actuators”. In: *International Conference on Advanced Robotics*. International Conference on Advanced Robotics. 2013, pp. 1–6.

[42] Kevin C. Galloway et al. “Soft Robotic Grippers for Biological Sampling on Deep Reefs”. In: *Soft Robotics* 3.1 (2016), pp. 23–33.

[43] Alan N Gent. *Engineering with rubber: how to design rubber components*. Carl Hanser Verlag GmbH Co KG, 2012.

[44] Aaron P. Gerratt, Hadrien O. Michaud, and Stéphanie P. Lacour. “Elastomeric Electronic Skin for Prosthetic Tactile Sensation”. In: *Advanced Functional Materials* (2015), pp. 2287–2295.

[45] M. Grebenstein. “Approaching Human Performance - The Functionality Driven Awiwi Robot Hand”. Dissertation. Zürich: ETH Zürich, 2012.

[46] G. Grioli et al. “Adaptive Synergies: an approach to the design of under-actuated robotic hands”. In: *IEEE/RSJ International Conference on Intelligent Robots and Systems (IROS)*. 2012, pp. 1251–1256.

[47] Andrzej Grzesiak, Ralf Becker, and Alexander Verl. “The Bionic Handling Assistant: a success story of additive manufacturing”. In: *Assembly Automation* 31.4 (2011), pp. 329–333.

[48] Abhishek Gupta et al. “Learning Dexterous Manipulation for a Soft Robotic Hand from Human Demonstrations”. In: *IEEE/RSJ International Conference on Intelligent Robots and Systems*. 2016, pp. 3786–3793.

[49] F. Heinemann et al. “A taxonomy of human grasping behavior suitable for transfer to robotic hands”. In: *2015 IEEE International Conference on Robotics and Automation (ICRA)*. 2015 IEEE International Conference on Robotics and Automation (ICRA). 2015, pp. 4286–4291.

[50] Shigeo Hirose and Yoji Umetani. “The development of soft gripper for the versatile robot hand”. In: *Mechanism and Machine Theory* 13.3 (1978), pp. 351–359.

[51] D. P. Holland et al. “The Soft Robotics Toolkit: Strategies for Overcoming Obstacles to the Wide Dissemination of Soft-Robotic Hardware”. In: *IEEE Robotics Automation Magazine* 24.1 (2017), pp. 57–64.

[52] Bianca S. Homberg et al. “Haptic Identification of Objects Using a Modular Soft Robotic Gripper”. In: *International Conference on Intelligent Robots and Systems (IROS)*. International Conference on Intelligent Robots and Systems (IROS). 2015.

[53] Josie Hughes et al. “Soft Manipulators and Grippers: A Review”. In: *Frontiers in Robotics and AI* 3 (2016), p. 69.

[54] F. Ilievski et al. “Soft Robotics for Chemists”. In: *Angewandte Chemie International Edition* 50.8 (2011), pp. 1890–1895.

[55] Alec Jacobson et al. “Skinning: Real-time Shape Deformation”. In: *ACM SIGGRAPH 2014 Courses*. 2014.

[56] Ishan D. Joshipura et al. “Methods to pattern liquid metals”. In: *Journal of Materials Chemistry C* 3.16 (2015), pp. 3834–3841.

[57] Makoto Kaneko et al. “Analysis on Detaching Assist Motion (DAM)”. In: *Proceedings 2001 IEEE International Conference on Robotics and Automation (ICRA)*. IEEE International Conference on Robotics and Automation (ICRA). Vol. 3. 2001, pp. 3028–3033.

[58] I. A. Kapandji. “Cotation clinique de l’opposition et de la contre-opposition du pouce”. In: *Annales de Chirurgie de la Main* 5.1 (1986), pp. 68–73.

[59] Dov Katz et al. “Interactive segmentation, tracking, and kinematic modeling of unknown 3D articulated objects”. In: *Proceedings of the IEEE International Conference on Robotics and Automation (ICRA)*. IEEE International Conference on Robotics and Automation (ICRA). 2013, pp. 5003–5010.

[60] M. Kazemi et al. *Robust Object Grasping using Force Compliant Motion Primitives*. CMU-RI-TR-12-04. 2012.

[61] Moslem Kazemi et al. “Human-Inspired Force Compliant Grasping Primitives”. In: *Autonomous Robots* 37.2 (2014), pp. 209–225.

[62] Moslem Kazemi et al. “Robust Object Grasping using Force Compliant Motion Primitives”. In: *Proceedings of Robotics: Science and Systems*. Sydney, Australia, 2012.

[63] E. Knoop et al. “Handshakiness: Benchmarking for Human-Robot Hand Interactions”. In: *IEEE/RSJ International Conference on Intelligent Robots and Systems (IROS) (in press)*. 2017.

[64] J. P. Lewis, Matt Cordner, and Nickson Fong. “Pose Space Deformation: A Unified Approach to Shape Interpolation and Skeleton-driven Deformation”. In: *Proceedings of the 27th Annual Conference on Computer Graphics and Interactive Techniques*. SIGGRAPH '00. New York, NY, USA: ACM Press/Addison-Wesley Publishing Co., 2000, pp. 165–172.

[65] Tomás Lozano-Pérez, Matthew T. Mason, and Russell H. Taylor. “Automatic Synthesis of Fine-Motion Strategies for Robots”. In: *The International Journal of Robotics Research* 3.1 (1984), pp. 3 –24.

[66] R. R. Ma and A. M. Dollar. “On dexterity and dexterous manipulation”. In: *2011 15th International Conference on Advanced Robotics (ICAR)*. 2011 15th International Conference on Advanced Robotics (ICAR). 2011, pp. 1–7.

[67] R.R. Ma, L.U. Odhner, and A.M. Dollar. “A modular, open-source 3D printed underactuated hand”. In: *2013 IEEE International Conference on Robotics and Automation (ICRA)*. 2013 IEEE International Conference on Robotics and Automation (ICRA). 2013, pp. 2737–2743.

[68] R.R. Ma, L.U. Odhner, and A.M. Dollar. “Dexterous manipulation with underactuated fingers: Flip-and-pinch task”. In: *2012 IEEE International Conference on Robotics and Automation (ICRA)*. 2012 IEEE International Conference on Robotics and Automation (ICRA). 2012, pp. 3551 –3552.

[69] M. Malvezzi et al. “SynGrasp: A MATLAB Toolbox for Underactuated and Compliant Hands”. In: *Robotics Automation Magazine, IEEE* 22.4 (2015), pp. 52–68.

[70] A.D. Marchese et al. “Design and control of a soft and continuously deformable 2D robotic manipulation system”. In: *2014 IEEE International Conference on Robotics and Automation (ICRA)*. 2014 IEEE International Conference on Robotics and Automation (ICRA). 2014, pp. 2189–2196.

[71] Ramses V. Martinez et al. “Elastomeric Origami: Programmable Paper-Elastomer Composites as Pneumatic Actuators”. In: *Advanced Functional Materials* 22.7 (2012), pp. 1376–1384.

[72] Ramses V. Martinez et al. “Robotic Tentacles with Three-Dimensional Mobility Based on Flexible Elastomers”. In: *Advanced Materials* 25.2 (2013), pp. 205–212.

[73] M. T. Mason. “Mechanics and Planning of Manipulator Pushing Operations”. In: *The International Journal of Robotics Research* 5.3 (1986), pp. 53–71.

[74] Matthew T. Mason. “Compliance and Force Control for Computer-Controlled Manipulators”. In: *IEEE Trans on Systems, Man, and Cybernetics*. Vol. 11. 6. IEEE, 1981, pp. 418–432.

[75] Matthew T. Mason. “The mechanics of manipulation”. In: *1985 IEEE International Conference on Robotics and Automation. Proceedings*. 1985 IEEE International Conference on Robotics and Automation. Proceedings. Vol. 2. 1985, pp. 544–548.

[76] P. Meier, M. Lang, and S. Oberthür. “Reiterated tension testing of silicone elastomer”. In: *Plastics, Rubber and Composites* 34.8 (2005), pp. 372–377.

[77] A.T. Miller and P.K. Allen. “Graspit! a versatile simulator for robotic grasping”. In: *IEEE Robotics & Automation Magazine* 11.4 (2004), pp. 110–122.

[78] John Morrow et al. “Improving Soft Pneumatic Actuator Fingers through Integration of Soft Sensors, Position and Force Control, and Rigid Fingernails”. In: Robotics and Automation (ICRA), 2016 IEEE International Conference on. 2016, pp. 5024–5031.

[79] Bobak Mosadegh et al. “Pneumatic Networks for Soft Robotics that Actuate Rapidly”. In: *Advanced Functional Materials* 24.15 (2014), pp. 2163–2170.

[80] Philip Moseley et al. “Modeling, Design, and Development of Soft Pneumatic Actuators with Finite Element Method”. In: *Advanced Engineering Materials* 18.6 (2016), pp. 978–988.

[81] Nicolaus Correll et al. “Soft Autonomous Materials - Using Active Elasticity and Embedded Distributed Computation”. In: *Proceedings of the 12th International Symposium on Experimental Robotics (ISER)*. 12th International Symposium on Experimental Robotics (ISER). 2010.

[82] Lael U. Odhner and Aaron M. Dollar. “Stable, open-loop precision manipulation with underactuated hands”. In: *The International Journal of Robotics Research* 34.11 (2015), pp. 1347–1360.

[83] Lael U. Odhner et al. “A compliant, underactuated hand for robust manipulation”. In: *The International Journal of Robotics Research* 33.5 (2014), pp. 736–752.

[84] L.U. Odhner, R.R. Ma, and A.M. Dollar. “Open-Loop Precision Grasping With Underactuated Hands Inspired by a Human Manipulation Strategy”. In: *IEEE Transactions on Automation Science and Engineering* 10.3 (2013), pp. 625–633.

[85] M. F. Peschl. “Triple-loop learning as foundation for profound change, individual cultivation, and radical innovation. Construction processes beyond scientific and rational knowledge”. In: *Constructivist Foundations* 2.2 (2007), pp. 136–145.

[86] Eckart Pilz and Ernst Becker. *Technische Strömungslehre: Eine Einführung in die Grundlagen und technischen Anwendungen der Strömungsmechanik*. Teubner Studienbücher Mechanik, 1993.

[87] P. Polygerinos et al. “Modeling of Soft Fiber-Reinforced Bending Actuators”. In: *IEEE Transactions on Robotics* 31.3 (2015), pp. 778–789.

[88] P. Polygerinos et al. “Towards a soft pneumatic glove for hand rehabilitation”. In: *2013 IEEE/RSJ International Conference on Intelligent Robots and Systems*. 2013 IEEE/RSJ International Conference on Intelligent Robots and Systems. 2013, pp. 1512–1517.

[89] Domenico Prattichizzo and Jeffrey C. Trinkle. “Grasping”. In: *Springer Handbook of Robotics*. Ed. by Bruno Siciliano Prof and Oussama Khatib Prof. Springer Berlin Heidelberg, 2008, pp. 671–700.

[90] Steffen Puhlmann et al. “A Compact Representation of Human Single-Object Grasping”. In: *Proceedings of 2016 IEEE International Conference on Intelligent Robots and Systems (IROS)*. 2016 IEEE International Conference on Intelligent Robots and Systems (IROS). 2016, pp. 1954–1959.

[91] F. Renda et al. “A 3D steady-state model of a tendon-driven continuum soft manipulator inspired by the octopus arm”. In: *Bioinspiration & Biomimetics* 7.2 (2012), p. 025006.

[92] F. Renda et al. “Discrete Cosserat approach for soft robot dynamics: A new piecewise constant strain model with torsion and shears”. In: *2016 IEEE/RSJ International Conference on Intelligent Robots and Systems (IROS)*. 2016 IEEE/RSJ International Conference on Intelligent Robots and Systems (IROS). 2016, pp. 5495–5502.

[93] F. Renda et al. “Dynamic Model of a Multibending Soft Robot Arm Driven by Cables”. In: *IEEE Transactions on Robotics* 30.5 (2014), pp. 1109–1122.

[94] G. Robinson, J. B. C. Davies, and J. P. P. Jones. “Development of the Amadeus dextrous robot end-effectors”. In: *OCEANS '98 Conference Proceedings*. OCEANS '98 Conference Proceedings. Vol. 2. 1998, 703–707 vol.2.

[95] A. Rocchi et al. “Stable simulation of underactuated compliant hands”. In: *2016 IEEE International Conference on Robotics and Automation (ICRA)*. 2016, pp. 4938–4944.

[96] N. Rojas, R. R. Ma, and A. M. Dollar. “The GR2 Gripper: An Underactuated Hand for Open-Loop In-Hand Planar Manipulation”. In: *IEEE Transactions on Robotics* 32.3 (2016), pp. 763–770.

[97] J. Romero et al. “Spatio-temporal modeling of grasping actions”. In: *2010 IEEE/RSJ International Conference on Intelligent Robots and Systems (IROS)*. 2010 IEEE/RSJ International Conference on Intelligent Robots and Systems (IROS). 2010, pp. 2103–2108.

[98] F. Rothling et al. “Platform portable anthropomorphic grasping with the bielefeld 20-dof shadow and 9-dof tum hand”. In: *Intelligent Robots and Systems, 2007. IROS 2007. IEEE/RSJ International Conference on*. 2007, pp. 2951–2956.

[99] M. Santello, M. Flanders, and J. F. Soechting. “Postural Hand Synergies for Tool Use”. In: *The Journal of Neuroscience* 18.23 (1998), pp. 10105–10115.

[100] Marco Santello, Martha Flanders, and John F Soechting. “Patterns of Hand Motion During Grasping and the Influence of Sensory Guidance”. In: *The Journal of Neuroscience* 22.4 (2002), pp. 1426–1435.

[101] C. Della Santina et al. “Dexterity augmentation on a synergistic hand: The Pisa/IIT SoftHand+”. In: *2015 IEEE-RAS 15th International Conference on Humanoid Robots (Humanoids)*. 2015 IEEE-RAS 15th International Conference on Humanoid Robots (Humanoids). 2015, pp. 497–503.

[102] Otto Scharmer. *Theory U: Leading from the Future as It Emerges*. San Francisco, CA, USA: Berrett-Koehler Publishers, 2008.

[103] S. Schulz, C. Pylatiuk, and G. Bretthauer. "A new ultralight anthropomorphic hand". In: *IEEE International Conference on Robotics and Automation, 2001. Proceedings 2001 ICRA*. IEEE International Conference on Robotics and Automation, 2001. Proceedings 2001 ICRA. Vol. 3. IEEE, 2001, 2437–2441 vol.3.

[104] Y. Shapiro, A. Wolf, and G. Kósa. "Compliant Bi-bellows actuator with PVDF force-shape sensing". In: *2012 4th IEEE RAS EMBS International Conference on Biomedical Robotics and Biomechatronics (BioRob)*. 2012 4th IEEE RAS EMBS International Conference on Biomedical Robotics and Biomechatronics (BioRob). 2012, pp. 1602–1606.

[105] Yoel Shapiro, Alon Wolf, and Kosa Gabor. "Bi-bellows: Pneumatic bending actuator". In: *Sensors and Actuators A: Physical* 167.2 (2011), pp. 484–494.

[106] Jun Shintake. "Functional Soft Robotic Actuators Based on Dielectric Elastomers". PhD thesis. Lausanne: Lausanne : Ecole Polytechnique Fédérale de Lausanne, 2016.

[107] A. Shiva et al. "Tendon-Based Stiffening for a Pneumatically Actuated Soft Manipulator". In: *IEEE Robotics and Automation Letters* 1.2 (2016), pp. 632–637.

[108] Harshal Arun Sonar and Jamie Paik. "Soft Pneumatic Actuator Skin with Piezoelectric Sensors for Vibrotactile Feedback". In: 2 (2016), p. 38.

[109] Y. Sun, Y. S. Song, and J. Paik. "Characterization of silicone rubber based soft pneumatic actuators". In: *2013 IEEE/RSJ International Conference on Intelligent Robots and Systems*. 2013 IEEE/RSJ International Conference on Intelligent Robots and Systems. 2013, pp. 4446–4453.

[110] M. Tavakoli and A. T. de Almeida. "Adaptive under-actuated anthropomorphic hand: ISR-SoftHand". In: *2014 IEEE/RSJ International Conference on Intelligent Robots and Systems*. 2014, pp. 1629–1634.

[111] M. Tavakoli et al. "Actuation strategies for underactuated anthropomorphic hands". In: *2014 IEEE/RSJ International Conference on Intelligent Robots and Systems*. 2014, pp. 274–280.

[112] Mahmoud Tavakoli, Rafael Batista, and Lucio Sgrigna. "The UC Softhand: Light Weight Adaptive Bionic Hand with a Compact Twisted String Actuation System". In: *Actuators* 5.1 (2015), p. 1.

[113] Michael T. Tolley et al. "A Resilient, Untethered Soft Robot". In: *Soft Robotics* 1.3 (2014), pp. 213–223.

[114] Maxime Tournier et al. "Stable Constrained Dynamics". In: *ACM Trans. Graph.* 34.4 (2015), 132:1–132:10.

[115] Vincent Wall, Raphael Deimel, and Oliver Brock. "Selective Stiffening of Soft Actuators Based on Jamming". In: *Proceedings of the IEEE International Conference on Robotics and Automation (ICRA)*. IEEE International Conference on Robotics and Automation (ICRA). IEEE, 2015, pp. 252–257.

[116] Martin Weigel et al. “iSkin: Flexible, Stretchable and Visually Customizable On-Body Touch Sensors for Mobile Computing”. In: *Proceedings of the 33rd Annual ACM Conference on Human Factors in Computing Systems*. CHI '15. New York, NY, USA: ACM, 2015, pp. 2991–3000.

[117] Yong-Jae Kim et al. “Design of a Tubular Snake-like Manipulator with Stiffening Capability by Layer Jamming”. In: International Conference on Intelligent Robots and Systems (IROS). 2012, pp. 4251–4256.

[118] J. Z Zheng, S. De La Rosa, and A. M Dollar. “An investigation of grasp type and frequency in daily household and machine shop tasks”. In: *2011 IEEE International Conference on Robotics and Automation (ICRA)*. 2011 IEEE International Conference on Robotics and Automation (ICRA). IEEE, 2011, pp. 4169–4175.

Index